

AD-A119 386

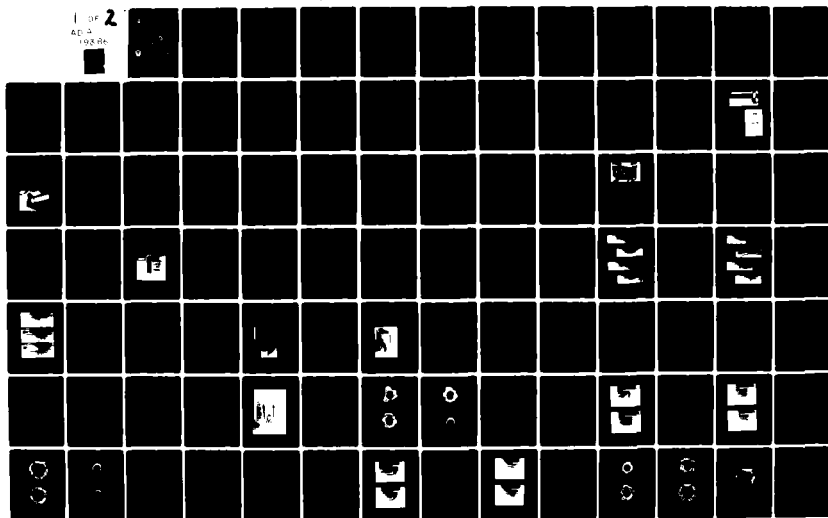
TEXAS UNIV AT AUSTIN FLUID DYNAMICS INST
IMPINGEMENT FLOW-FIELDS FOR TUBE-LAUNCHED ROCKETS.(U)

F/G 21/2

AUG 82 S A BOUSLOG, J J BERTIN, W B WINGERT DAAH01-81-C-B078
82-101 DRSMI/RL-CR-82-5 NL

UNCLASSIFIED

1 OF 2
AD-A
103-86



AD A119386

2

IMPINGEMENT FLOW-FIELDS
FOR TUBE-LAUNCHED ROCKETS

DTIC
ELECTE
SEP 20 1982
S H D

Stanley A. Bouslog,
John J. Bertin,
and
William B. Wingert, II



U.S. ARMY MISSILE COMMAND
Redstone Arsenal, Alabama 38809

DTIC FILE COPY

Fluid Dynamics Inst. 82-101
TR-RL-CR-82-5

August 1982

This work was supported
by the U.S. Army through
DAAH01-81-C-0078

Approved for public release; distribution unlimited.

SECURITY CLASSIFICATION OF THIS PAGE (When Data Entered)

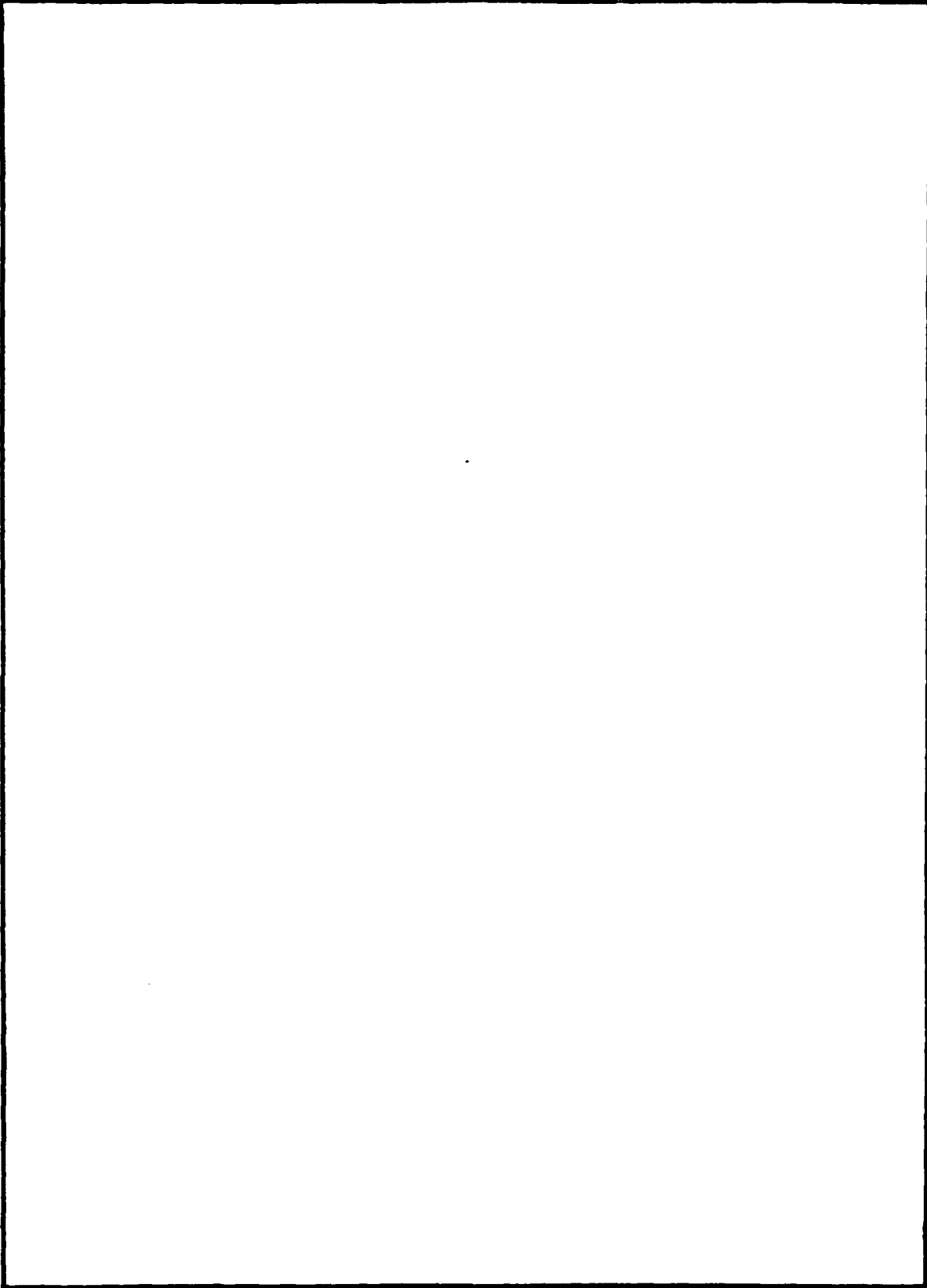
REPORT DOCUMENTATION PAGE		READ INSTRUCTIONS BEFORE COMPLETING FORM
1. REPORT NUMBER TR-RL-CR-82-5	2. GOVT ACCESSION NO. AD-A119386	3. RECIPIENT'S CATALOG NUMBER
4. TITLE (and Subtitle) Impingement Flow-Fields for Tube-Launched Rockets		5. TYPE OF REPORT & PERIOD COVERED Contractor Report
7. AUTHOR(s) Stanley A. Bouslog, John J. Bertin, and William B. Wingert, II		6. PERFORMING ORG. REPORT NUMBER Fluid Dynamics Inst. 82-101
9. PERFORMING ORGANIZATION NAME AND ADDRESS Department of Aerospace Engineering and Engineering Mechanics UT-Austin, Austin, TX 78712		8. CONTRACT OR GRANT NUMBER(s) DAAH01-81-C-B078
11. CONTROLLING OFFICE NAME AND ADDRESS		10. PROGRAM ELEMENT, PROJECT, TASK AREA & WORK UNIT NUMBERS
14. MONITORING AGENCY NAME & ADDRESS (if different from Controlling Office)		12. REPORT DATE Aug. 1982
		13. NUMBER OF PAGES
		15. SECURITY CLASS. (of this report) UNCLASSIFIED
		15a. DECLASSIFICATION/DOWNGRADING SCHEDULE
16. DISTRIBUTION STATEMENT (of this Report) Approved for public release; distribution unlimited.		
17. DISTRIBUTION STATEMENT (of the abstract entered in Block 20, if different from Report)		
18. SUPPLEMENTARY NOTES		
19. KEY WORDS (Continue on reverse side if necessary and identify by block number) Launch-tube flow fields, viscous/inviscid interactions, rocket-exhaust flows.		
20. ABSTRACT (Continue on reverse side if necessary and identify by block number) An experimental program has been conducted to measure the pressures acting on the face of a launcher assembly due to the impingement of an underexpanded rocket exhaust flow.		

DD FORM 1 JAN 73 1473

EDITION OF 1 NOV 65 IS OBSOLETE
S/N 0102-LF-014-6601

SECURITY CLASSIFICATION OF THIS PAGE (When Data Entered)

SECURITY CLASSIFICATION OF THIS PAGE (When Data Entered)



SECURITY CLASSIFICATION OF THIS PAGE (When Data Entered)



CONTENTS

Accession For		
NTIS GRA&I	<input checked="" type="checkbox"/>	
DTIC TAB	<input type="checkbox"/>	
Unannounced	<input type="checkbox"/>	
Justification		
By		
Distribution/		
Availability Codes		
Dist	Avail and/or	
A	Special	

	Page
1. INTRODUCTION.	13
2. EXPERIMENTAL PROGRAM.	21
2.1 Test Facility.	21
2.2 Coordinate Systems	21
2.3 Simulated Rocket	21
2.4 Simulated Launcher	29
2.5 Test Program	33
3. DATA ACQUISITION AND REDUCTION.	39
3.1 Pressure Measurements.	39
3.2 Contour Mapping.	39
3.3 Shadowgraphs	44
4. DISCUSSION OF RESULTS	47
4.1 Characterization of the Impingement Flow Field	47
4.2 Pressure Distributions on the Face of the Launcher Assembly.	69
4.3 Effect of an Open Adjacent Tube.	117
4.4 Pressure Differentials Acting on the Rocket.	128
5. CONCLUDING REMARKS.	132
LITERATURE CITED.	133
NOMENCLATURE.	135

FIGURES

- 1 Static pressure distribution on flat plate at $M_{ne} = 2.0$,
 $\theta_{ne} = 10^\circ$, and $\frac{p_{ne}}{p_{atm}} = 5.1$.
(reference 9). 16

FIGURES (Cont'd)

	<u>Page</u>
2 Shock wave structure in an underexpanded jet impinging on a flat plate (reference 9).	18
3 Schematic diagram of the flow in the center of the flat plate, $M_{ne} = 2.0$, $\theta_{ne} = 10^\circ$, $\frac{p_{ne}}{p_{atm}} = 5.1$ and $h/r_{ne} = 10.0$ (reference 9).	19
4 Schematic of the University of Texas Rocket Exhaust Effects Facility	22
5 Photographs of the simulated rocket and the multi-tube launcher assembly.	23
a Simulated rocket with yoke assembly.	23
b Model of the multi-tube launcher assembly.	25
6 Rocket/multi-tube launcher assembly	25
a Isometric sketch	25
b Photograph	25
7 Coordinate systems used in data presentations	27
a Coordinate system for launcher pressure measurements	27
b Coordinate system for pressure measurements from the model rocket.	27
8 10° Conical Nozzle, the C1 Nozzle	28
9 Sketch of the C1 rocket nozzle illustrating pressure orifice locations. Scale: actual size. $r_{ne} = 1.453\text{cm}$ (0.572 in.).	30
10 Simulated Multi-tube Rocket Launcher.	31
a Front view of launcher (Full scale).	31
b Side view of launcher (0.31 scale)	32
11 Face of launch-tube assembly.	35
a Photograph	35
b Sketch illustrating pressure-orifice locations	35

FIGURES (Cont'd)

	<u>Page</u>
12 Internal instrumentation for launch tube 2.	37
13 Photograph of Data Acquisition System	41
14 Sample Output of Data Acquisition System.	43
15 Sample Contour Map.	45
16 Photographs of the C1 nozzle exhausting into quiescent air. . . .	49
a $p_{t1} = 6.89 \times 10^5 \text{ N/m}^2$ (100 psi).	49
b $p_{t1} = 1.38 \times 10^6 \text{ N/m}^2$ (200 psi).	49
c $p_{t1} = 2.76 \times 10^6 \text{ N/m}^2$ (400 psi).	49
d $p_{t1} = 3.45 \times 10^6 \text{ N/m}^2$ (500 psi).	49
e $p_{t1} = 4.14 \times 10^6 \text{ N/m}^2$ (600 psi).	51
f $p_{t1} = 4.83 \times 10^6 \text{ N/m}^2$ (700 psi).	51
g $p_{t1} = 5.52 \times 10^6 \text{ N/m}^2$ (800 psi).	51
h $p_{t1} = 7.69 \times 10^6$ (1115 psi).	51
17 Characteristics of the Free-Jet	53
a $p_{t1} = 2.76 \times 10^6 \text{ N/m}^2$ (400 psi).	53
b $p_{t1} = 4.83 \times 10^6 \text{ N/m}^2$ (700 psi).	53
c $p_{t1} = 7.69 \times 10^6 \text{ N/m}^2$ (1115 psi)	53
18 Illustration of the Characteristic Features of Subcritical and Supercritical Flow Fields.	57
a Subcritical flow, $h = 10 r_{ne}$, $p_{t1} = 4.86 \times 10^6 \text{ N/m}^2$ (705 psi).	57
b Supercritical flow, $h = 10 r_{ne}$, $p_{t1} = 7.52 \times 10^6 \text{ N/m}^2$ (1090 psi)	59

FIGURES (Cont'd)

		<u>Page</u>
19	Threshold values for the stagnation pressure required for the supercritical flow.	62
20	Location of the Mach disc for the free jet and for impinging flows	64
	a Rocket "launched" from tube #1.	64
	b Rocket "launched" from tube #2.	65
21	Diameter of the Mach disc for the free jet and for impinging flows	66
22	Standoff Distance (from nozzle-exit plane to the Mach disk) as a function of separation distance (h).	67
23	Shadowgraph of the unstable Mach disc at $h = 6.0 r_{ne}$ and $p_{t1} = 4.206 \times 10^6 \text{ N/m}^2$	71
24	Static pressure distributions (tube 2), $h = 8.0 r_{ne}$	73
	a $p_{t1} = 7.34 \times 10^6 \text{ N/m}^2$	73
	b $p_{t1} = 4.79 \times 10^6 \text{ N/m}^2$	73
	c $p_{t1} = 4.72 \times 10^6 \text{ N/m}^2$	74
	d $p_{t1} = 4.12 \times 10^6 \text{ N/m}^2$	74
	e $p_{t1} = 2.71 \times 10^6 \text{ N/m}^2$	75
25	Shadowgraphs of plume impingement (tube 2), $h = 8.0 r_{ne}$	77
	a $p_{t1} = 7.52 \times 10^6 \text{ N/m}^2$	77
	b $p_{t1} = 4.83 \times 10^6 \text{ N/m}^2$	77
	c $p_{t1} = 4.14 \times 10^6 \text{ N/m}^2$	79
	d $p_{t1} = 2.76 \times 10^6 \text{ N/m}^2$	79

FIGURES (Cont'd)

		<u>Page</u>
26	Static pressure distributions (tube 2), $h = 12.0 r_{ne}$	81
a	$p_{t1} = 7.58 \times 10^6 \text{ N/m}^2$	81
b	$p_{t1} = 6.00 \times 10^6 \text{ N/m}^2$	81
c	$p_{t1} = 5.33 \times 10^6 \text{ N/m}^2$	82
d	$p_{t1} = 4.72 \times 10^6 \text{ N/m}^2$	82
e	$p_{t1} = 2.71 \times 10^6 \text{ N/m}^2$	83
27	Shadowgraphs of plume impingement (tube 2), $h = 12.0 r_{ne}$	87
a	$p_{t1} = 7.62 \times 10^6 \text{ N/m}^2$	87
b	$p_{t1} = 6.21 \times 10^6 \text{ N/m}^2$	87
c	$p_{t1} = 5.24 \times 10^6 \text{ N/m}^2$	89
d	$p_{t1} = 2.76 \times 10^6 \text{ N/m}^2$	89
28	Static pressure distributions (tube 2), $p_{t1} \approx 7.58 \times 10^6 \text{ N/m}^2$. .	91
a	$h = 2.0 r_{ne} = 0.21 \tilde{x}_m$	91
b	$h = 4.0 r_{ne} = 0.42 \tilde{x}_m$	91
c	$h = 6.0 r_{ne} = 0.63 \tilde{x}_M$	92
d	$h = 10.0 r_{ne} = 1.05 \tilde{x}_M$	92
e	$h = 15.0 r_{ne} = 1.56 \tilde{x}_M$	93

Note: Flow is supercritical

FIGURES (Cont'd)

		<u>Page</u>
29	Shadowgraphs of the plume impingement (tube 2), $p_{t1} \approx 7.58 \times 10^6 \text{ N/m}^2$	95
a	$h = 4.0 r_{ne}$	95
b	$h = 6.0 r_{ne}$	95
c	$h = 10.0 r_{ne}$	97
d	$h = 15.0 r_{ne}$	97
30	Static pressure distributions (tube 2), $p_{t1} \approx 4.83 \times 10^6 \text{ N/m}^2$	99
a	$h = 2.0 r_{ne} = 0.27 \tilde{x}_M$	99
b	$h = 4.0 r_{ne} = 0.53 \tilde{x}_M$	99
c	$h = 6.0 r_{ne} = 0.80 \tilde{x}_M$	100
d	$h = 10.0 r_{ne} = 1.33 \tilde{x}_M$	100
e	$h = 15.0 r_{ne} = 2.0 \tilde{x}_M$	101
31	Shadowgraphs of the plume impingement (tube 2), $p_{t1} \approx 4.83 \times 10^6 \text{ N/m}^2$	103
a	$h = 4.0 r_{ne}$	103
b	$h = 6.0 r_{ne}$	103
c	$h = 10.0 r_{ne}$	105
d	$h = 15 r_{ne}$	105

FIGURES (Cont'd)

		<u>Page</u>
32	Static pressure distributions (tube 2), $p_{t1} \approx 2.76 \times 10^6 \text{ N/m}^2$	108
a	$h = 2.0 r_{ne}$	108
b	$h = 4.0 r_{ne}$	108
c	$h = 6.0 r_{ne}$	109
d	$h = 10.0 r_{ne}$	109
e	$h = 15.0 r_{ne}$	110
33	Shadowgraphs of the plume impingement (tube 2), $p_{t1} \approx 2.76 \times 10^6 \text{ N/m}^2$	112
a	$h = 4.0 r_{ne}$	112
b	$h = 6.0 r_{ne}$	112
c	$h = 10.0 r_{ne}$	114
d	$h = 15.0 r_{ne}$	114
34	Characteristics of the flow field defined by maximum static pressures on the launcher face, $p_{t1} = 7.58 \times 10^6 \text{ N/m}^2$	116
a	pressure data, tube #6.	116
b	$h \approx 4r_{ne} < h_1^*$	116
c	$h \approx 10r_{ne} > h_1^*$	116
35	Maximum static pressures on the face of the launcher assembly. .	118
a	tube #6	118
b	tube #2	119

FIGURES (Cont'd)

		Page
36	Static-pressure distributions with adjacent tube closed and open, $p_{t1} \approx 7.58 \times 10^6 \text{ N/m}^2$	120
a	$h = 4.0 r_{ne}$, adjacent tube closed.	120
b	$h = 4.0 r_{ne}$, adjacent tube open.	120
c	$h = 6.0 r_{ne}$, adjacent tube closed.	121
d	$h = 6.0 r_{ne}$, adjacent tube open.	121
e	$h = 10.0 r_{ne}$, adjacent tube closed	122
f	$h = 10.0 r_{ne}$, adjacent tube open	122
g	$h = 15.0 r_{ne}$, adjacent tube closed	123
h	$h = 15.0 r_{ne}$, adjacent tube open	123
37	Static-pressure distributions with adjacent tube open and closed, $p_{t1} \approx 4.83 \times 10^6 \text{ N/m}^2$	124
a	$h = 4.0 r_{ne}$, adjacent tube closed.	124
b	$h = 4.0 r_{ne}$, adjacent tube open.	124
c	$h = 6.0 r_{ne}$, adjacent tube closed.	125
d	$h = 6.0 r_{ne}$, adjacent tube open.	125
e	$h = 10.0 r_{ne}$, adjacent tube closed	126
f	$h = 10.0 r_{ne}$, adjacent tube open	126
g	$h = 15.0 r_{ne}$, adjacent tube closed	127
h	$h = 15.0 r_{ne}$, adjacent tube open	127

FIGURES (Cont'd)

		<u>Page</u>
38	Maximum pressure differentials acting on the simulated rocket.	130
a	$p_{t1} \approx 7.58 \times 10^6 \text{ N/m}^2$	130
b	$p_{t1} \approx 4.83 \times 10^6 \text{ N/m}^2$	131

DELIBERATELY BLANK

1. (U) INTRODUCTION

The complex viscid/inviscid interaction flow field created by the impingement of a supersonic jet on a nearby surface occurs in a variety of applications. For some applications, the axis of the jet is parallel to the surface^{1,2,3}, such as might occur when a missile is launched from an airplane or during stage separation. The axis of the impinging jet is normal (or nearly normal) to the surface for the highly underexpanded exhaust from a rocket leaving the lunar surface⁴. However, the characteristics of these impingement flow fields are substantially different than those that occur in connection with the design of launcher facilities for supersonic missiles.

In the study of the jet-impingement flow field for launchers, most investigators have simulated the impingement of a supersonic jet onto a flat, solid surface that is perpendicular to the jet axis. Gummer and Hunt⁵ found that the impingement of a properly-expanded, uniform jet that was located approximately one r_{ne} above a plate produced a static pressure distribution that was a maximum at the centerline and decreased slowly in the radial direction. The main features of the flow for these conditions included a symmetric shock wave spanning the jet that was convex upwards causing an outward deflection of the streamlines and the reduction of the flow velocities downstream of the shock wave to subsonic speeds.

¹ Vick, A. R., and Andrews, E. H., Jr., "An Experimental Investigation of Highly Underexpanded Free Jets Impinging Upon a Parallel Flat Surface", TND - 2326, June 1964, NASA.

² Ivanov, M. Y., and Nazarov, V. P., "'Lateral' Interaction of a Supersonic Underexpanded Ideal-Gas Jet With Surfaces of Different Shape", Izvestiya Akademii Nauk SSSR, Mekhanika Zhidkosti i Gaza, No. 6, November - December 1974, pp. 3 - 8.

³ Smith, S. D., Penny, M. M., Greenwood, T. F., and Roberts, B. B., "Exhaust Plume Impingement of Chemically Reacting Gas-Particle Flows", AIAA Paper No. 75-688, AIAA 10th Thermophysics Conference, Denver, Colorado, May 1975.

⁴ Stitt, L. E., "Interaction of Highly Underexpanded Jets With Simulated Lunar Surfaces", TND - 1095, December 1961, NASA.

⁵ Gummer, J. H., and Hunt, B. L., "The Impingement of a Uniform Axisymmetric, Supersonic Jet on a Perpendicular Flat Plate", The Aeronautical Quarterly, Vol. 22, November 1971, pp. 403 - 420.

In an experimental investigation of a supersonic jet impinging onto a circular disk, whose diameter was four times that of the jet, Henderson⁶ observed a sudden and intense increase in the noise level generated by the interaction. The increase occurred when the exit-plane Mach number was approximately 2 and the plate was 4 r_{ne} to 7 r_{ne} from the exit plane. Morch⁷ found that, although the Mach shock wave for the free jet is stable, a shock instability may occur if a resonator is inserted into the jet at such a position that a blunt-body shock-wave, generated by the presence of the resonator, is produced upstream of the position where the Mach shock would normally occur in the free jet. The shock oscillations do not occur if the resonator is located very near the nozzle.

As the distance (h) from the nozzle-exit plane to the barrier is increased, it is apparent that the shock structure changes. Based on the investigations of Semiletenko and Uskov⁸, Ginzburg et al.⁹, and Golubkov, et al.¹⁰, the variation of the wave structure in the interaction flow field of the impinging jet with distance is as follows.

⁶ Henderson, L. F., "Experiments on the Impingement of a Supersonic Jet on a Flat Plate", Journal of Applied Mathematics and Physics, Vol. 17, 1966, pp. 553 - 569.

⁷ Morch, K. A., "A Theory for the Mode of Operation of the Hartmann Air Jet Generator", Journal of Fluid Mechanics, Vol. 20, 1964, pp. 141 - 159.

⁸ Semiletenko, B. G., and Uskov, V. N., "Empirical Formulas for Locating Shock Waves in a Jet Impinging on a Barrier at Right Angles", Inzhenerno - Fizicheskii Zhurnal, Vol. 23, No. 3, September 1972, pp. 453 - 458.

⁹ Ginzburg, I. P., Semiletenko, B. G., and Uskov, V. N., "Experimental Study of Underexpanded Jets Impinging Normally on a Plane Baffle", Fluid Mechanics - Soviet Research, Vol. 4, No. 3, May - June 1975, pp. 93 - 105.

¹⁰ Golubkov, A. G., Koz'menko, B. K., Ostapenko, V. A., and Solotchin, A. V., "On the Interaction of an Underexpanded Supersonic Jet with a Finite Flat Baffle", Fluid Mechanics - Soviet Research, Vol. 3, No. 1, January - February 1974, pp. 96 - 102.

(1) When h is relatively small, the central compression shock wave (CSW) is convex towards the nozzle. This is consistent with the structure observed by Gummer and Hunt⁵.

(2) As h is increased, the central compression shock wave may pass through inflections becoming concave towards the nozzle.

For cases (1) and (2), Ginzburg et al.⁹ note that the static pressure distribution has a maximum at the center of the barrier.

(3) When the distance between the nozzle-exit plane and the plate is increased further, the pressure at the centerline decreases more rapidly than that near the edge. Semiletenko and Uskov⁸ note that the wave structure at a critical value of h (which will be designated h_1^* for this report) fluctuates at a high frequency. This unstable interaction is accompanied by the generation of strong acoustic waves. Ginzburg et al.⁹ note that the strong instability and the sonic vibration develop when the pressure at the center of the obstruction becomes equal to that in the peripheral region.

(4) Ginzburg et al.⁹ noted further that, when h was increased above h_1^* , there was a further reduction of the pressure in the central region, while the pressure at the periphery remained about the same. Thus, for $h > h_1^*$, the character of the static pressure distribution on the obstacle changed, exhibiting a peak near the periphery of the impinging jet. Pressure distributions for $h < h_1^*$ and for $h > h_1^*$, as taken from ref. 9, are reproduced in Fig. 1. Although the mechanism is not discussed, Piesek and Roberts¹¹ present a pressure distribution

⁵ Gummer, J. H., and Hunt, B. L., "The Impingement of a Uniform Axisymmetric, Supersonic Jet on a Perpendicular Flat Plate", The Aeronautical Quarterly, Vol. 22, November 1971, pp. 403 - 420.

⁸ Semiletenko, B. G., and Uskov, V. N., "Empirical Formulas for Locating Shock Waves in a Jet Impinging on a Barrier at Right Angles", Inzhenerno - Fizicheskii Zhurnal, Vol. 23, No. 3, September 1972, pp. 453 - 458.

⁹ Ginzburg, I. P., Semiletenko, B. G., and Uskov, V. N., "Experimental Study of Underexpanded Jets Impinging Normally on a Plane Baffle", Fluid Mechanics - Soviet Research, Vol. 4, No. 3, May - June 1975, pp. 93 - 105.

¹¹ Piesek, E. T., and Roberts, D. J., "A Method to Define Low-Altitude Rocket Exhaust Characteristics and Impingement Effects", Journal of Spacecraft and Rockets, Vol. 7, No. 4, April 1970, pp. 446 - 451.

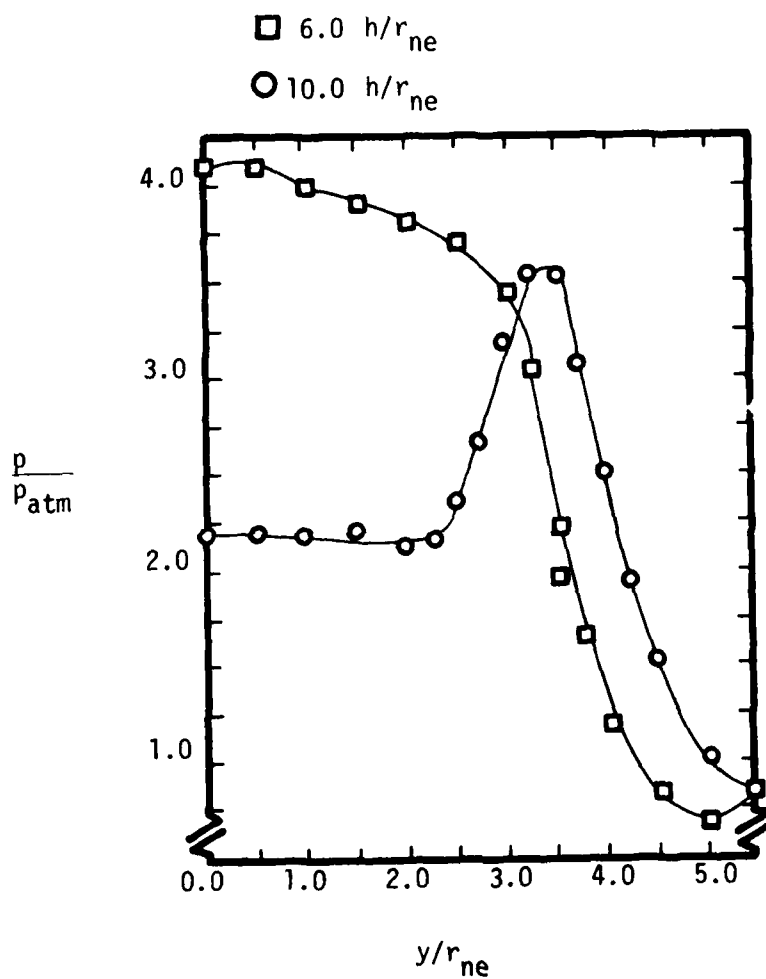


Figure 1. - Static pressure distribution on flat plate at $M_{ne} = 2.0$, $\theta_{ne} = 10^\circ$, and $\frac{p_{ne}}{p_{atm}} = 5.1$.
(reference 9).

similar to that for $h > h_1^*$.

For values of $h > h_1^*$, the shock structure exhibits the elements shown in Fig. 2. There is a central compression shock wave (CSW) that is concave towards the nozzle. An oblique, reflected shock wave (RSW) occurs outboard of the intersection of the CSW and the lip shock wave (LSW). Because the reflected shock wave is more oblique and relatively weaker than the central compression shock wave, the total pressure is greater downstream of the RSW than downstream of the CSW. Thus, as the flow decelerates toward the plate, a peak occurs in the local pressure near the periphery of the impinging jet.

Using schlieren photographs, oil-flow patterns, and hot-wire probes, Ginzburg et al.⁹ recorded the existence of a central region of flow reversal. A sketch of the flow near the center of the plate (as taken from ref. 9) is presented in Fig. 3. The dividing streamline on the plate occurred in the region of the peripheral pressure peak. Belov et al.¹² have used integral equations and an approximate flow model similar to that of Fig. 2 in order to estimate the heating to the surface of the plate.

(5) As h is increased still further, a second, weak, instability is observed^{8,9}. The acoustic field and the fluctuations in the wave structure at this value of h (which will be designated h_2^*) are much weaker than those observed during the first instability mode.

(6) The weak instability is followed by a stepwise transition to a stable mode. In this case, the shock wave structure corresponds to the wave structure of a free-jet exhausting into the ambient atmosphere, but there is a second, centered shock wave that is produced as the flow encounters the plate. This second CSW is initially convex to the nozzle and then, as h is increased, becomes concave to the nozzle.

⁸ Semiletenko, B. G., and Uskov, V. N., "Empirical Formulas for Locating Shock Waves in a Jet Impinging on a Barrier at Right Angles", *Inzhenerno - Fizicheskii Zhurnal*, Vol. 23, No. 3, September 1972, pp. 453 - 458.

⁹ Ginzburg, I. P., Semiletenko, B. G., and Uskov, V. N., "Experimental Study of Underexpanded Jets Impinging Normally on a Plane Baffle", *Fluid Mechanics - Soviet Research*, Vol. 4, No. 3, May - June 1975, pp. 93 - 105.

¹² Belov, I. A., Ginzburg, I. P., and Shub, L. I., "Supersonic Under-expanded Jet Impingement upon Flat Plate", *International Journal of Heat-Mass Transfer*, Vol. 16, 1973, pp. 2067 - 2076.

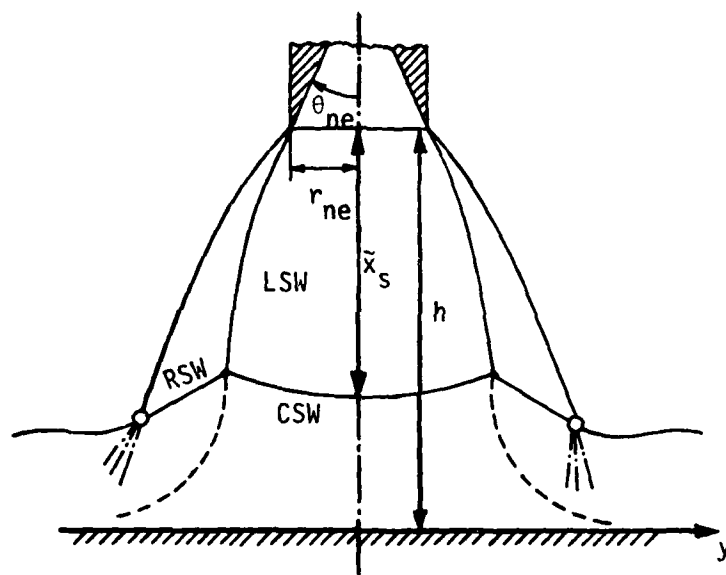


Figure 2. - Shock wave structure in an underexpanded jet impinging on a flat plate (reference 9).

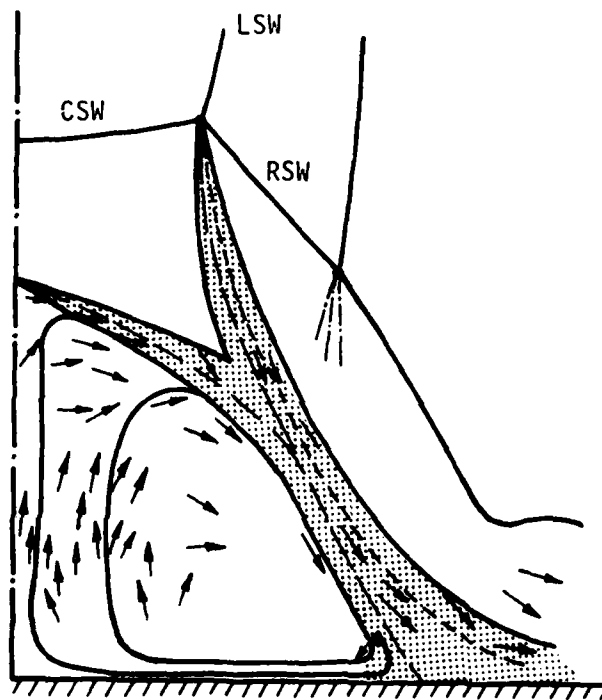


Figure 3. - Schematic diagram of the flow in the center of the flat

plate, $M_{ne} = 2.0$, $\theta_{ne} = 10^\circ$, $\frac{p_{ne}}{p_{atm}} = 5.1$ and $h/r_{ne} = 10.0$
(reference 9).

(7) As the nozzle exit-plane moves far from the obstruction, viscous effects would spread across the entire jet. The pressure distribution on the plate would be relatively constant across the impingement (see ref. 11).

The values of h_1^* and of h_2^* at which the interaction flow-field changes character depend on the conditions in the nozzle-exit plane, on the ratio of specific heats of the exhaust gas (γ), on the jet-expansion ratio ($n = p_{ne}/p_{atm}$), and on the relative dimensions of the jet and of the obstruction.

In all of the investigations discussed thus far, the jet exhaust impinged on a solid obstruction. However, for a rocket exiting from a launcher, the obstruction contains one, or more, openings through which the exhaust gases can pass. The present report discusses data that were obtained at the Rocket Exhaust Effects Facility at the University of Texas at Austin in which a simulated underexpanded rocket-exhaust-plume impinged on the face of a multi-tube launcher. The plume was produced when unheated air was accelerated through a convergent/divergent nozzle for various stagnation pressures, such that the static pressure in the nozzle-exit plane was up to 5 atmospheres, i.e., the jet-expansion ratio was up to 5. The launch-tube assembly represented a configuration containing six launch tubes and an overhead crane. The launch-tube assembly could be moved relative to the simulated rocket in order to provide data illustrating the effect of the distance and the orientation between the nozzle-exit plane and the face of the launcher assembly for launches from different tubes. Data were obtained with a single tube open and with two tubes open. This latter configuration represents the second launch in a ripple-fire sequence.

The viscid/inviscid shock-interaction flow-field was defined using pressure measurements and flow visualization photographs. Static pressures were measured on the face of the launcher assembly, in the launch tube, and on the rocket itself. These data are discussed in the present report.

(7) As the nozzle exit-plane moves far from the obstruction, viscous effects would spread across the entire jet. The pressure distribution on the plate would be relatively constant across the impingement (see ref. 11).

The values of h_1^* and of h_2^* at which the interaction flow-field changes character depend on the conditions in the nozzle-exit plane, on the ratio of specific heats of the exhaust gas (γ), on the jet-expansion ratio ($n = p_{ne}/p_{atm}$), and on the relative dimensions of the jet and of the obstruction.

In all of the investigations discussed thus far, the jet exhaust impinged on a solid obstruction. However, for a rocket exiting from a launcher, the obstruction contains one, or more, openings through which the exhaust gases can pass. The present report discusses data that were obtained at the Rocket Exhaust Effects Facility at the University of Texas at Austin in which a simulated underexpanded rocket-exhaust-plume impinged on the face of a multi-tube launcher. The plume was produced when unheated air was accelerated through a convergent/divergent nozzle for various stagnation pressures, such that the static pressure in the nozzle-exit plane was up to 5 atmospheres, i.e., the jet-expansion ratio was up to 5. The launch-tube assembly represented a configuration containing six launch tubes and an overhead crane. The launch-tube assembly could be moved relative to the simulated rocket in order to provide data illustrating the effect of the distance and the orientation between the nozzle-exit plane and the face of the launcher assembly for launches from different tubes. Data were obtained with a single tube open and with two tubes open. This latter configuration represents the second launch in a ripple-fire sequence.

The viscid/inviscid shock-interaction flow-field was defined using pressure measurements and flow visualization photographs. Static pressures were measured on the face of the launcher assembly, in the launch tube, and on the rocket itself. These data are discussed in the present report.

2. EXPERIMENTAL PROGRAM

2.1 Test Facility

The tests were conducted at the Rocket Exhaust Effects Facility located at the Experimental Aerodynamics Laboratory (EAL) of the University of Texas at Austin. A schematic diagram of this blow-down type facility is presented in Figure 4. Simulated rocket exhaust plumes were obtained by accelerating unheated, compressed air (the test gas) through a pipe with a convergent-divergent nozzle (the simulated rocket). The simulated rocket (i.e., the pipe/nozzle configuration) was threaded to a high pressure supply line and held firmly in place by a yoke assembly. A photograph of the pipe/nozzle/yoke configuration is presented in Figure 5(a). The model of the multi-tube launcher was mounted on a carriage assembly that allowed translation in the x- (or streamwise), y-, and z-directions, and rotation in the pitch and yaw planes. A photograph of the multi-tube launcher and carriage assembly mounted on the rails that permit movement in the axial direction is presented in Figure 5(b). An isometric sketch and a photograph of the basic rocket/launcher configuration are presented in Figure 6.

2.2 Coordinate Systems

The data obtained during this experimental program are presented in one of two coordinate systems. The coordinate system for the pressure measurements from the launcher are illustrated in Figure 7(a). The origin of the coordinate system is located at the front face of the launcher with the positive x-axis directed along the centerline of the launch tube. The z-axis is located in the vertical plane of the facility and the y-axis completes a right-handed coordinate system. The second coordinate system for the pressure measurements on the rocket consists only of an axial coordinate, \bar{x}/r_{ne} . The origin is located at the nozzle-exit plane (see Figure 7(b)). This coordinate system was used only to locate pressure orifices on the external rocket surface. Note that all dimensions were non-dimensionalized by the internal radius of the nozzle exit, r_{ne} .

2.3 Simulated Rocket

A sketch illustrating the geometry of the 10° conical convergent/divergent nozzle used to produce the simulated rocket exhaust is presented in Figure 8. The nozzle-exit radius, r_{ne} , which is used as the characteristic dimension to non-dimensionalize the length parameters, is 1.453 cm (0.572 in). The area ratio of the nozzle, A_{ne}/A^* , is 2.242. If one assumes isentropic gas flow

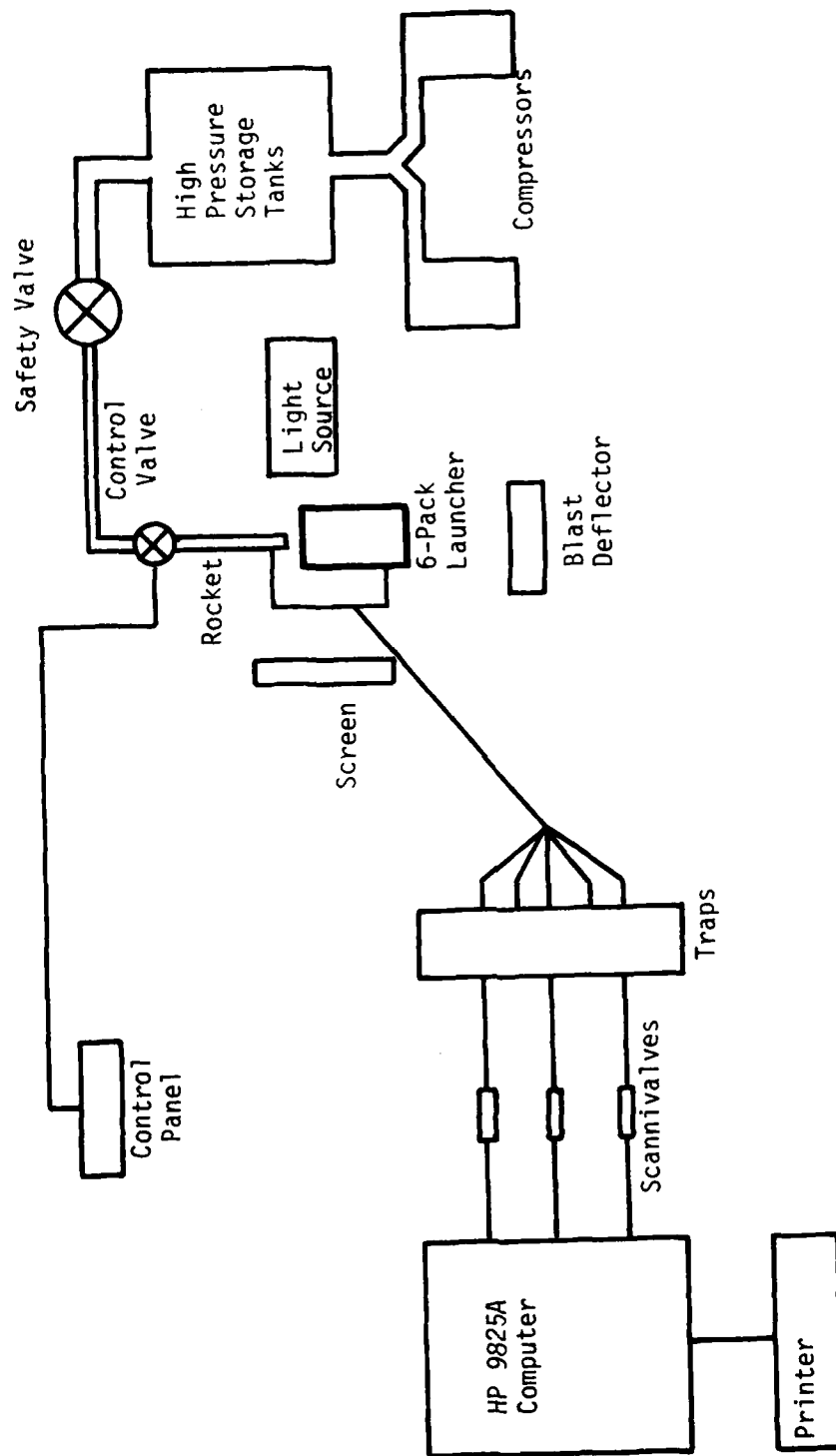
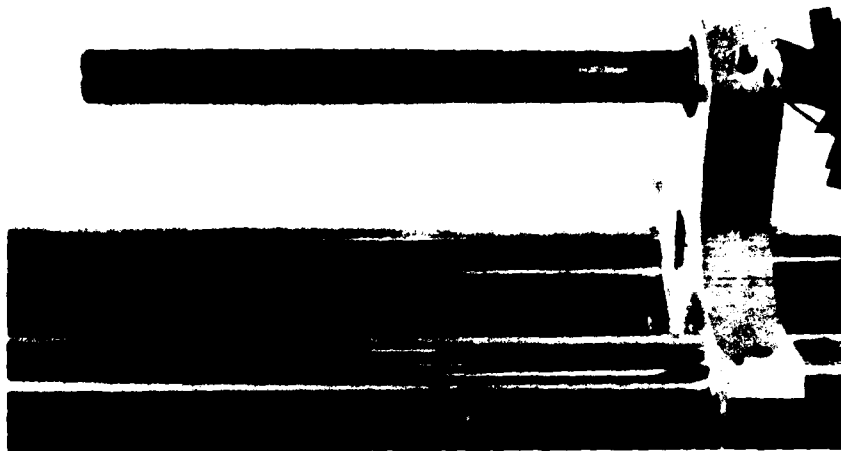


Figure 4. - Schematic of the University of Texas Rocket Exhaust Effects Facility.



(a) Simulated rocket with yoke assembly.

(b) Model of the multi-tube launcher assembly.

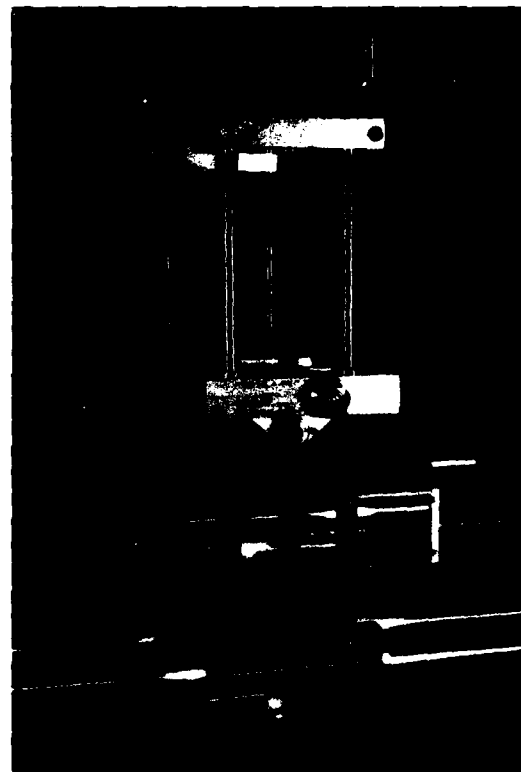
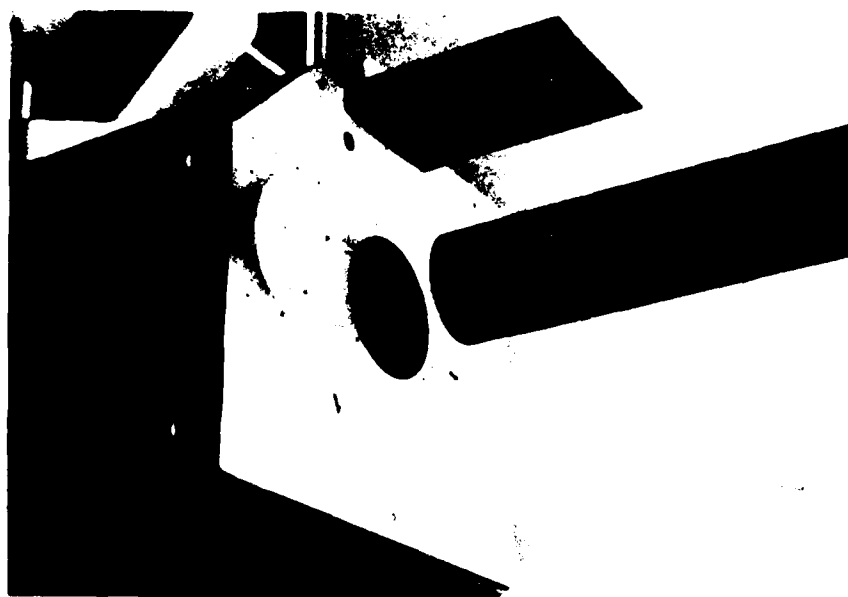
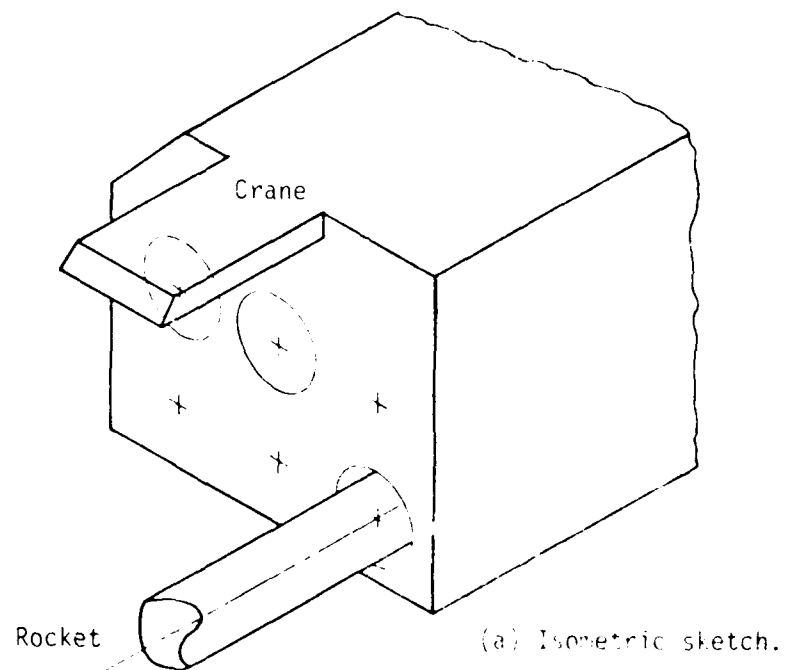


Figure 5. - Photographs of the simulated rocket and the multi-tube launcher assembly.

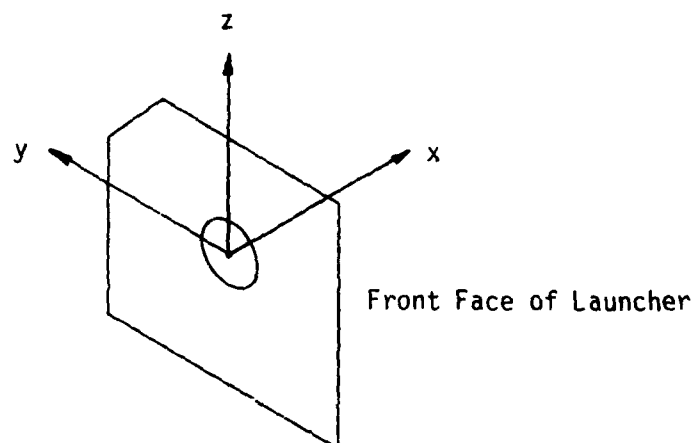
DELIBERATELY BLANK



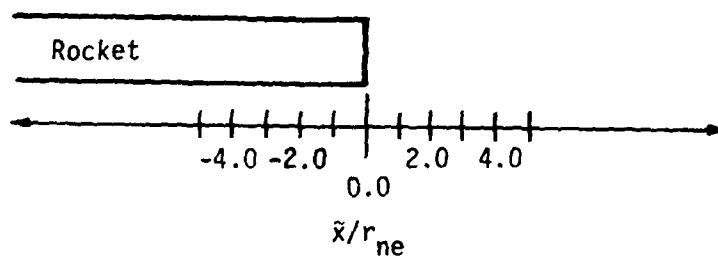
(b) Photograph

Figure 6. - Rocket/multi-tube launcher assembly.

DELIBERATELY BLANK



(a) Coordinate system for launcher pressure measurements.



(b) Coordinate system for pressure measurements from the model rocket.

Figure 7. - Coordinate systems used in data presentations.

Note: dimensions in centimeters (inches)

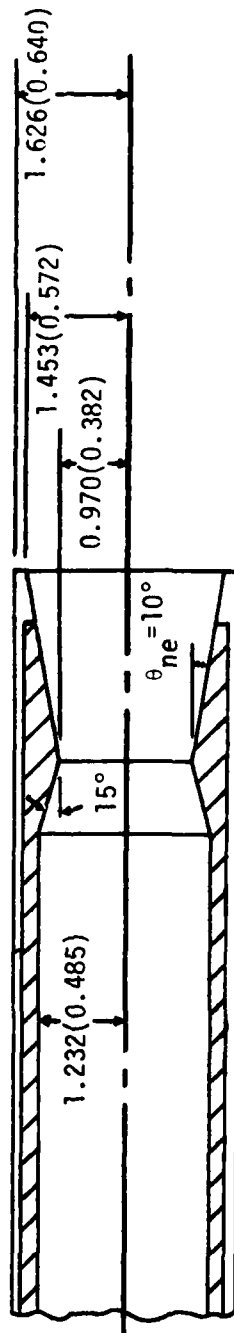


Figure 8. - 10° Conical Nozzle, the C1 Nozzle.

relations, the nozzle-exit-plane Mach number is 2.32.

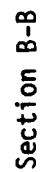
Instrumentation on the surface of the sleeved rocket. - The nozzle was sleeved so that small grooves could be milled in the outer surface to accept the stainless steel tubing used in measuring surface pressures. These inlaid tubes can be clearly seen in the photograph of Figure 5. A total of thirty-two diametrically-opposed static-pressure orifices were located in the surface of the simulated rocket which permitted the direct measurement of pressures acting on its outer surface. These orifices were located at selected axial and circumferential locations. Cross-sectional views of the particular axial locations at which the pressure taps were located are presented in Figure 9. The cross-sections, or "stations", which contain pressure taps are located at distances equal to integer multiples of the nozzle-exit radius from the nozzle-exit plane. This non-dimensional distance is also the station number. As shown in the figure, pressure taps were located at stations 1, 2, 3, 5 and 10.

At each station, pressure orifices were distributed circumferentially around the nozzle. The eight orifices located at each of stations, 1, 2, and 5 are 45° apart, while the four orifices located at each of stations 3 and 10 are 90° apart. However, rather than designate the circumferential location of each tap in degrees, the taps have been numbered 1 through 8 consecutively. The pressure tap on the top (positive z-direction) of the rocket has been designated as 1 ($\phi = 0^\circ$); while the remaining taps are numbered in increasing order in the clockwise direction as viewed from the nozzle exit. At stations 3 and 10 the orifices are numbered as if a total of eight orifices existed.

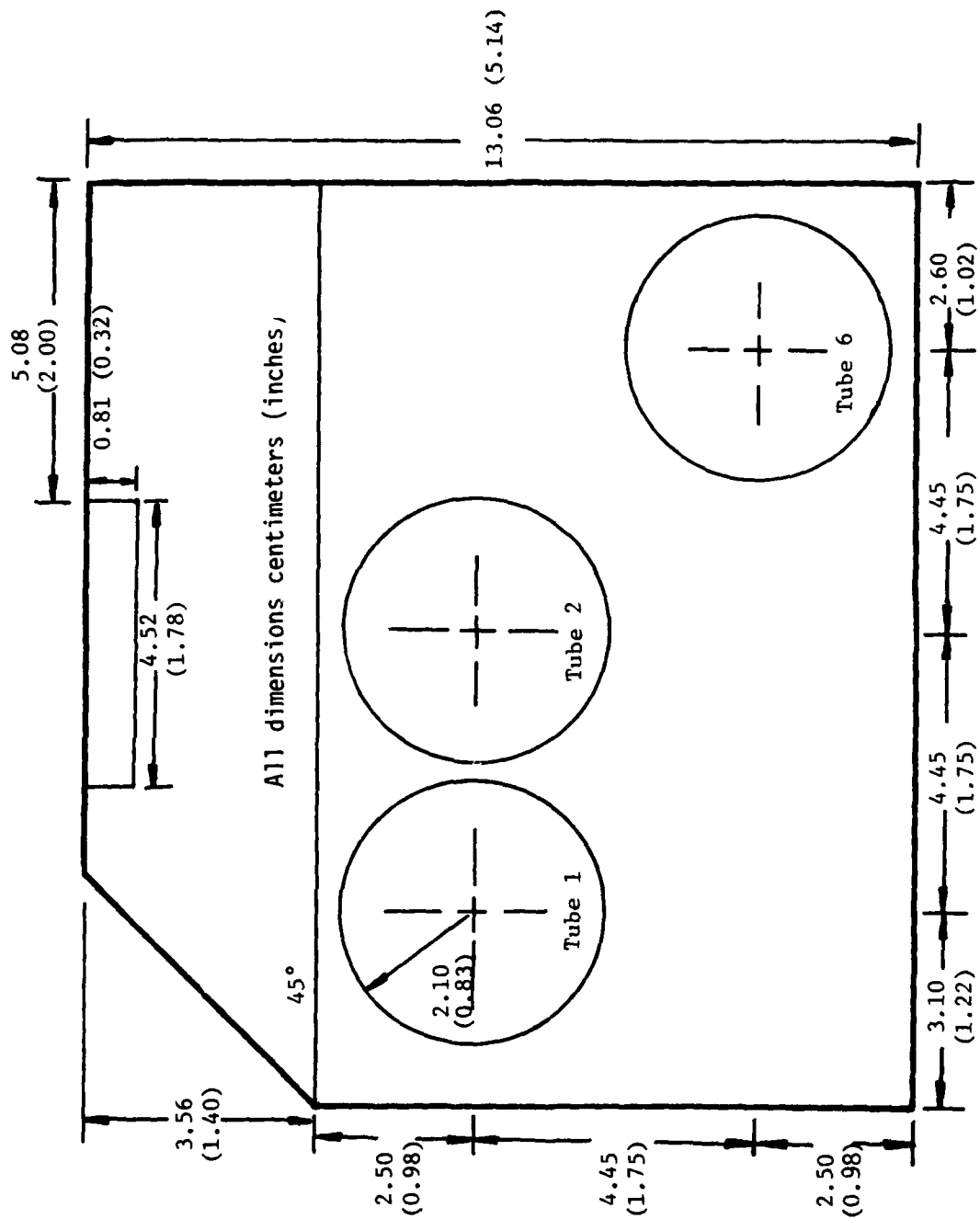
2.4 Simulated Launcher

A model of one half of a multi-tube launcher assembly containing twelve tubes has been constructed. The launcher assembly will be identified as the "6-pack." As shown in Figure 10 only three tubes were simulated in the model. The other three tubes remained "covered" for these tests. A quasi-steady-state rocket launch could be simulated either from tube number 1, 2, or 6. While "launching" the simulated rocket out of one tube, the remaining tubes could be open, as if a rocket had already been launched from that tube, or covered. Figure 10 illustrates the relative position of tubes 1, 2, and 6 and the overhang which simulates a telescoping crane used to reload the launcher. The internal radius of the constant cross-sectional area launch tubes was $1.44 r_{ne}$.

Mounting Assembly. - The launcher assembly was mounted on a carriage that rode on two steel rails, allowing streamwise movement relative



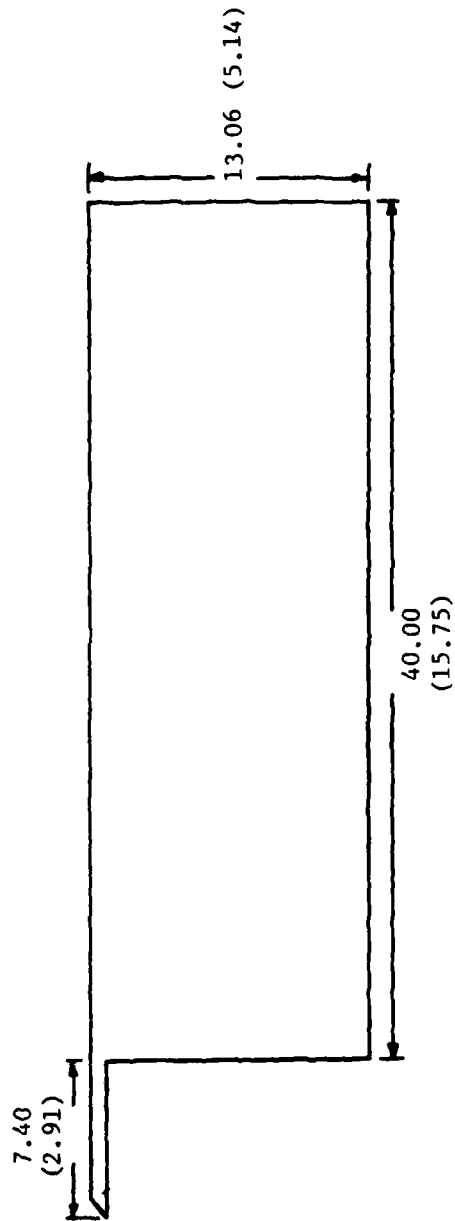
Section A-A



(a) Front view of launcher (Full scale)

Figure 10. - Simulated Multi-tube Rocket Launcher.

Note: All dimensions in centimeters (inches)



(b) Side view of launcher (0.31 scale).

Figure 10. - Concluded.

to the fixed nozzle-exit position. The carriage and rails are visible in Figure 5(b). Screw drives in the carriage provided for vertical and lateral movement of the 6-pack. The attachment point permitted the rotation of the 6-pack in the pitch and yaw planes. The translational movements could be measured within ± 0.003 cm (0.001 in). Initial alignment of the rocket with the launch tube, so that both center lines would be colinear, was made with an estimated error of ± 0.05 degrees. However, any rotation beyond the initial position could be measured to within only ± 0.5 degrees.

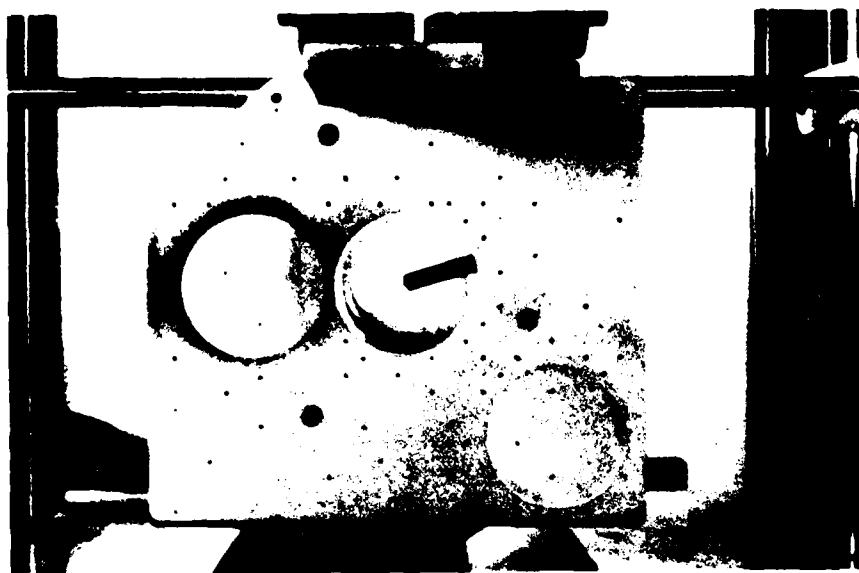
Launcher instrumentation. - The front face of the simulated launcher was fitted with eighty-one pressure orifices, each 0.064 cm (0.025 in) in diameter. The locations of these orifices, which are concentrated near the tube openings and become sparser further from the launch tubes, is shown in Figure 11. In the photograph, the cover of tube 2, which contains five pressure orifices, has been removed, revealing the pitot-probe assembly. The numbering scheme for the pressure orifices on the front plate is illustrated in Figure 11(b). Of the three launch tubes in the 6-pack only tube 2 was instrumented internally. As mentioned earlier, a pitot-probe mounted on a wedge airfoil was constructed and could be inserted into tube 2 to measure the total pressure of the flow entering the tube. Ten pressure orifices were located in the wall of launch tube 2 so that static-wall-pressures could be measured in the tube. A sketch of the instrumentation in tube 2 is presented in Figure 12. Due to the pitot-probe interference static-wall-pressures and pitot-pressures were not measured simultaneously.

2.5 Test Program

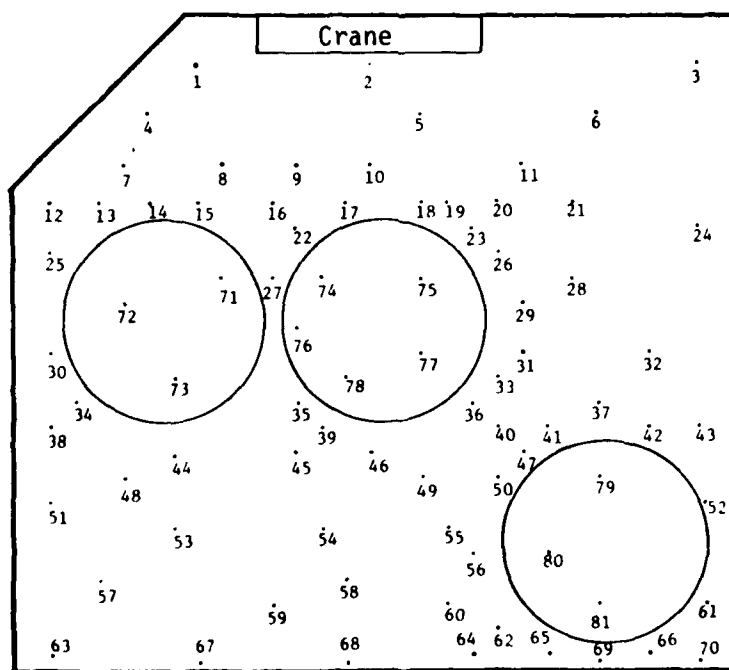
Three rocket/launcher configurations were simulated in this experimental program (1) rocket launching out of tube 1, (2) tube 2, or (3) tube 6. Before each run, the rocket was aligned so that its axis was colinear with that of the launch tube of interest. It should be noted that despite the painstaking alignment procedure, exhaust pressure loading on the launcher introduced a small misalignment between the rocket and the launcher during the run. Even though the carriage assembly allowed the simulation of mal-launch conditions, i.e., lateral, yawing, and/or pitching motion of the rocket relative to the launcher, these conditions were not simulated in this experimental program.

After the alignment procedure had been completed, the launcher assembly was locked into position. During the test, the stagnation pressure in the nozzle reservoir and, therefore, the mass-flow rate of the unheated air were controlled by the test operator. Once steady-state conditions were obtained at the desired chamber

DELIBERATELY BLANK



(a) Photograph



(b) Sketch illustrating pressure-orifice locations.

Figure 11. - Face of launch-tube assembly.

DELIBERATELY BLANK

Note: All dimensions in x/r_{ne} ($r_{ne} = 1.45 \text{ cm (0.572 in)}$)

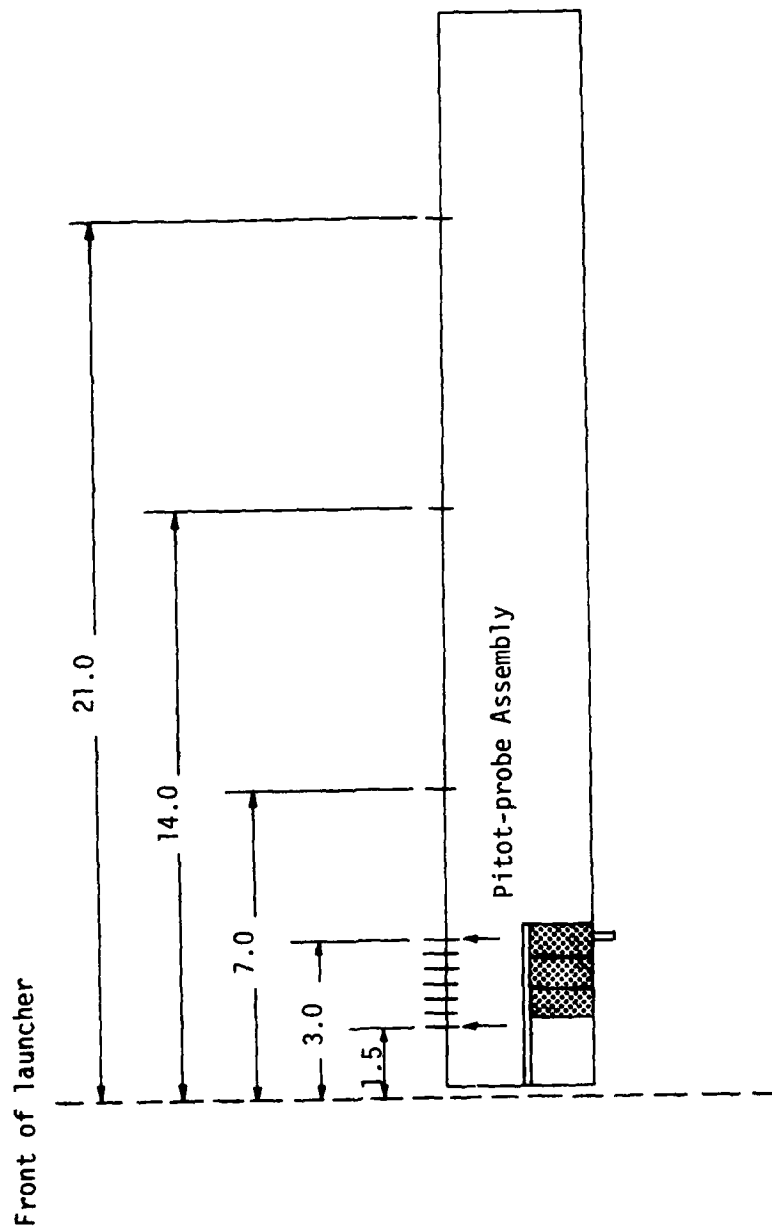


Figure 12. - Internal instrumentation for launch tube 2.

pressure, data were then recorded. Data were taken for nozzle-exit plane positions of 2.0, 4.0, 6.0, 8.0, 10.0, 12.0, and 15.0 r_{ne} from the front of the launcher, and for chamber pressures of 7.58×10^6 N/m² (1100 psi), 4.83×10^6 (700 psi), and 2.76×10^6 N/m² (400 psi). Additional data were obtained at nozzle-exit positions of 5.0 r_{ne} and 13.5 r_{ne} for runs out of tube 2. These tests were conducted with all tubes covered, except the tube from which the rocket was "launched". Additional tests were conducted with both the launch tube and the adjacent tube open. For example, data were obtained for tests out of tube 1 with tubes 2 and 6 covered and for tests out of tube 1 with tube 2 open and tube 6 covered.

Early in the experimental program, it was determined that for some conditions a transition between a subcritical and a supercritical flow field existed. This transition, which was accompanied by a pronounced sound change, occurred when a threshold stagnation pressure was reached. Furthermore, it occurred only for nozzle-exit positions exceeding 4.0 r_{ne} . Therefore, data were obtained for nozzle-exit positions exceeding 4.0 r_{ne} and for stagnation pressures slightly above and slightly below (approximately $\pm 3.45 \times 10^5$ N/m² (± 50 psi)) the threshold stagnation pressure for a given nozzle position. It should be emphasized that the threshold stagnation pressure was determined by the sound change and as the stagnation pressure was increasing.

In addition to pressure data, photographic data were also obtained during this test program. Besides providing an illustration of the general features of the flow field, the shadowgraphs of the exhaust impingement allowed the measurement of shock positions. Shadowgraphs were obtained for two rocket/launcher configurations. With the rocket "firing" out of tube 1 with tubes 2 and 6 covered, photographs were taken at nozzle-exit plane positions of 2.0, 4.0, 6.0, 8.0, 10.0, 12.0, and 15.0 r_{ne} , and for stagnation pressures ranging from 7.58×10^6 N/m² (1100 psi) to 6.89×10^5 N/m² (100 psi). Photographs of the exhaust impingement were also obtained for the rocket "firing" out of tube 2 with tubes 1 and 6 covered, and at nozzle-exit plane positions of 4.0, 6.0, 8.0, 10.0, 12.0, 13.5, and 15.0 r_{ne} , and for the same stagnation pressure range.

3. DATA ACQUISITION AND REDUCTION

For the present experimental program, both pressure and photographic data were obtained. Pressures on the front face of the launcher and on the surface of the simulated rocket were measured for a variety of launch conditions. Tube number 2 was instrumented so that static-wall pressure distributions or the pitot-pressure could be measured for selected runs. Shadowgraphs were also obtained for a variety of launch conditions.

3.1 Pressure Measurements

Nylon and vinyl pressure tubing connected the pressure orifices on the 6-pack and on the simulated rocket to pressure traps. After the stagnation pressure of interest in the nozzle chamber was obtained, a switch was thrown to isolate pressures in these traps. A scannivalve system was then used to measure the pressures in each trap. Pressures on the front face of the launcher were measured with a $3.45 \times 10^6 \text{ N/m}^2$ (500 psi) or a $6.89 \times 10^5 \text{ N/m}^2$ (100 psi) transducer. Pressures on the surface of the simulated rocket were measured using $1.03 \times 10^5 \text{ N/m}^2$ (15 psi) transducer. Each of these transducers had an error of $\pm 0.06\%$ of full scale. A HP9825A mini-computer controlled the scannivalve system. A photograph of the data acquisition system is presented in Figure 13.

The mini-computer also provided the tabulated values of the pressures measured on the face of the 6-pack and on the surface of the simulated rocket. All pressures were non-dimensionalized by the atmospheric pressure which was measured using a mercury barometer. A sample output is presented in Figure 14. The pressure measurements from the external surface of the rocket are differential pressures, i.e., the difference between pressures measured at diametrically opposed orifices. The reader should note that the error in the non-dimensional differential pressures should be approximately ± 0.0013 . However, this accuracy can be misleading. Recall that the simulated rocket was anchored by a yoke (see Figure 6). In runs where there was considerable entrainment of atmospheric air by the exhaust gas, the yoke interfered with the flow over the surface of the rocket. For these runs, the pressures on the surface of the rocket (especially those at large values of \tilde{x}/r_{ne}) are questionable. In order to define the interference problem, tufts were placed on the rocket and photographs were taken of the rocket during a run.

3.2 Contour Mapping

After generating the non-dimensionalized pressures on the front face of the 6-pack, these data were input into a contour mapping

DELIBERATELY BLANK

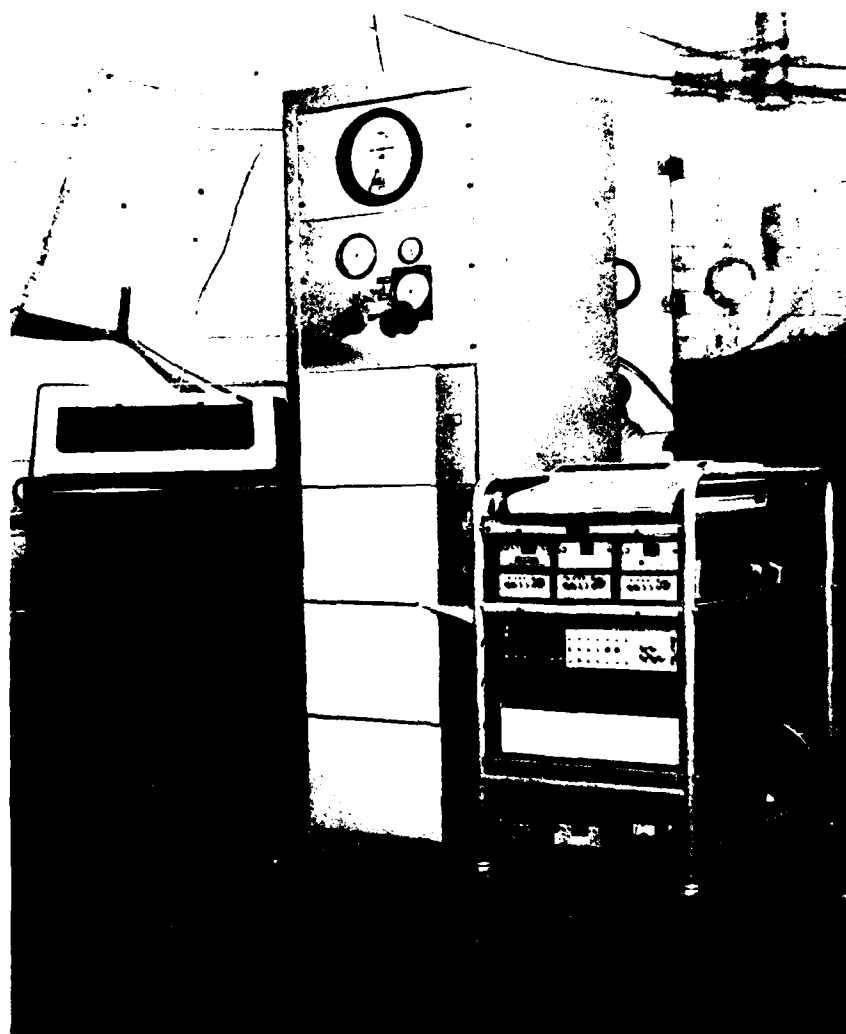


Figure 13. - Photograph of Data Acquisition System.

DELIBERATELY BLANK

U.T./BFC 6-PPE PROJECT									
Date: 27 OCT 1981									
Temperature(P): 528.00									
Ptl(PSt): 1084.8344									
Angle Alpha(deg): 0									
Launch Tube(s) Covered: 1,6									
Fired From Launch Tube: 2									
TAP NO.	P/Patr	TAP NO.	P/Patr	Xt/Pne	PMI (deg)	Delta F/Patr	PPFSSUPFS ON POCKET		
1	0.78094	39	5.23282	-1	0	-0.05602			
2	4.24715	40	8.36883	-1	45	0.00971			
3	1.21168	41	3.05927	-1	90	-0.03701			
4	0.60744	42	0.40477	-1	135	0.06226			
5	4.21991	43	0.66072	-2	0	-0.06161			
6	0.39016	44	0.43977	-2	45	-0.08219			
7	0.57300	45	10.68927	-2	90	-0.09810			
8	2.32799	46	5.35884	-2	135	0.08699			
9	6.41930	47	3.47893	-3	0	-0.07051			
10	5.80297	48	0.50394	-3	90	-0.04492			
11	4.15204	49	10.65372	-5	0	0.00263			
12	0.75167	50	2.66547	-5	45	-0.03281			
13	0.61150	51	1.04021	-5	90	-0.00788			
14	0.93467	52	1.22405	-5	135	0.01435			
15	2.28567	53	0.47039	-10	0	0.00241			
16	5.47288	54	0.84927	-10	90	0.00123			
17	6.25402	55	0.94160						
18	6.24156	56	0.34789						
19	5.91728	57	1.30687						
20	5.63169	58	0.36968						
21	2.78366	59	0.60024						
22	5.86099	60	0.53163						
23	6.04719	61	0.96989						
24	0.71085	62	0.60301						
25	0.73385	63	1.24012						
26	5.60630	64	0.82950						
27	5.74711	65	1.15886						
28	5.40594	66	1.00928						
29	5.45995	67	0.86361						
30	0.64511	68	1.21168						
31	5.46965	69	1.00199						
32	0.43838	70	0.98515						
33	5.44518	71	5.77204						
34	0.57688	72	0.53395						
35	5.36762	73	1.16643						
36	5.46364	79	0.28372						
37	0.92913	80	0.36082						
38	0.85988	81	0.94031						

PRESSURES IN TUBE NO. 2

Xt/Pne	P/Patr
1.50	1.66430
1.75	2.2928
2.00	2.86142
2.25	2.72153
2.50	2.63991
2.75	2.47038
3.00	2.30713
7.00	2.36327
14.00	1.90640
21.00	2.23825

Figure 14. - Sample Output of Data Acquisition System.

computer code, CONRAN. This code was obtained from the National Center for Atmospheric Research (NCAR) in Boulder, Colorado. The input to the code consisted of the non-dimensionalized pressures and the coordinates of the pressure orifices. CONRAN then triangulated the irregularly distributed data and performed the contouring by interpolating the triangulated data. The triangulation and interpolation schemes are based on Lawson's C1 surface interpolation algorithm¹³, which has been refined by Akima¹⁴. An outline of the front of the 6-pack was then overlaid on the contour map of isobars to present the pressure data on the face of the launcher. The reader should note that, because of the limited number of orifices and their irregular spacing and because of the interpolation procedure, the isobars will not exactly represent the actual pressure distribution. Since an axisymmetric jet was used, one would expect the isobars to be concentric "circles". However, due in part to the number, spacing and interpolation scheme for the static pressures and partially due to asymmetries in the flow, "islands" of high pressures have appeared. A sample contour map, which is shown in Figure 15, contain both a concentric isobar and "island" isobars. Clearly, if more pressure orifices were present, the "islands" would probably have been connected forming concentric isobars. Being aware of these problems, the contour maps can be used to rapidly recognize high and low pressure regions and to generally interpret the flow field existing on the face of the 6-pack.

3.3 Shadowgraphs

In order to obtain a better understanding of the flow field existing when an underexpanded jet impinges on the face of a multi-tube launcher, shadowgraphs of the exhaust impingement were made. A high voltage mercury-vapor lamp was used to provide an intense narrow beam of light that was reflected onto a 30.48 cm (12 in) diameter parabolic mirror. The mirror directed a parallel beam of light through the exhaust flow and projected an image on a transparent film. Photographs of the image could then be taken during runs. Shadowgraphs were obtained for a free jet and for two rocket-launcher configurations: (1) the rocket firing out of tube 1 with tubes 2 and 6 covered and (2) the

¹³Lawson, C. L., "Software for C1 Surface Interpolation", JPL Publication 77-30, August 15, 1977.

¹⁴Akima, H., "A Method of Bivariate Interpolation and Smooth Surface Fitting for Irregularly Distributed Data Points", ACM Transactions on Mathematical Software, Vol. 4, No. 2, June 1978, pp. 148 - 159.

rocket firing out of tube 2 with tubes 1 and 6 covered. These photographs were taken for several nozzle-exit positions, relative to the front of the launcher, ranging from 2.0 r_{ne} to 15 r_{ne} , and for stagnation pressures ranging from $6.89 \times 10^5 \text{ N/m}^2$ (100 psi) to $7.58 \times 10^6 \text{ N/m}^2$ (1100 psi).

4. DISCUSSION OF RESULTS

An experimental program has been conducted at the Rocket Exhaust Effects Facility during which a simulated rocket-exhaust plume impinged on the front surface of a multi-tube launcher. Static pressures were measured on the face of the launcher, along the wall of one of the tubes, and on the external surface of the simulated rocket. Shadowgraphs were taken of the impingement flow-field. These data were obtained over a range of stagnation pressure and for a range of separation distances between the simulated rocket and the launcher assembly.

4.1 Characterization of the Impingement Flow Field

As discussed in the Introduction, one can identify several distinctively different flow fields that result when an exhaust plume impinges on a plate. The type of impingement flow-field that exists depends on the diameter of the exhaust plume, on the size of the plate, and on the distance from the nozzle-exit plane to the plate. Many of the flow characteristics observed in the investigations of the impingement flow fields for plates and for disks were also observed in the present investigation where there was a large opening in the plate. However, the presence of a hole in the plate, i.e., the tube from which the rocket was launched, significantly modified the flow field. The most important characteristic dimension becomes the diameter of the plume relative to the diameter of the tube.

Shadowgraphs of the exhaust plume as a free jet are presented in Figure 16 for stagnation pressures from $6.89 \times 10^5 \text{ N/m}^2$ to $7.69 \times 10^6 \text{ N/m}^2$. At the lowest stagnation pressures, the flow in the nozzle-exit plane is overexpanded. Thus, the boundary of the free-jet plume does not go beyond the cylinder formed by extending the outer surface of the rocket. For stagnation pressures greater than $2.76 \times 10^6 \text{ N/m}^2$, the flow in the nozzle-exit plane is underexpanded and the flow continues to accelerate as it leaves the nozzle. As a result, the maximum plume diameter increases as p_{t1} increases. For p_{t1} greater than $3.45 \times 10^6 \text{ N/m}^2$, a normal shock wave, or Mach disk, forms due to the coalescence of the compression waves. The Mach disk increases in diameter and moves downstream as the stagnation pressure increases.

Enlargements of the shadowgraphs are presented in Figure 17 for three stagnation pressures: $2.76 \times 10^6 \text{ N/m}^2$, $4.83 \times 10^6 \text{ N/m}^2$, and $7.69 \times 10^6 \text{ N/m}^2$. Included in the photographs are scales depicting: (1) the nondimensional axial coordinate and (2) the internal diameter of the launch tube. In the subsequent discussion, the relation of these characteristic dimensions to the impingement flow-field will be

DELIBERATELY BLANK



(a) $p_{t1} = 6.89 \times 10^5 \text{ N/m}^2$ (100 psi)



(b) $p_{t1} = 1.38 \times 10^6 \text{ N/m}^2$ (200 psi)



(c) $p_{t1} = 2.76 \times 10^6 \text{ N/m}^2$ (400 psi)



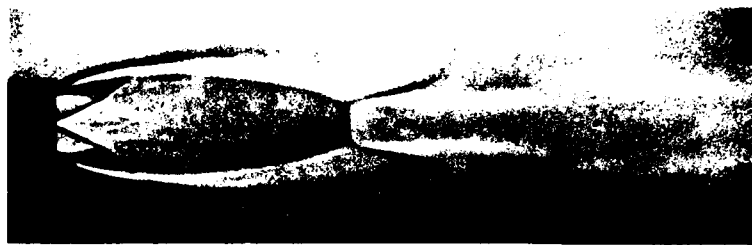
(d) $p_{t1} = 3.45 \times 10^6 \text{ N/m}^2$ (500 psi)

Figure 16. - Photographs of the C1 nozzle exhausting into quiescent air.

DELIBERATELY BLANK



(e) $p_{t1} = 4.14 \times 10^6 \text{ N/m}^2$ (600 psi)



(f) $p_{t1} = 4.83 \times 10^6 \text{ N/m}^2$ (700 psi)



(g) $p_{t1} = 5.52 \times 10^6 \text{ N/m}^2$ (800 psi)



(h) $p_{t1} = 7.69 \times 10^6$ (1115 psi)

Figure 16.- Concluded.

DELIBERATELY BLANK

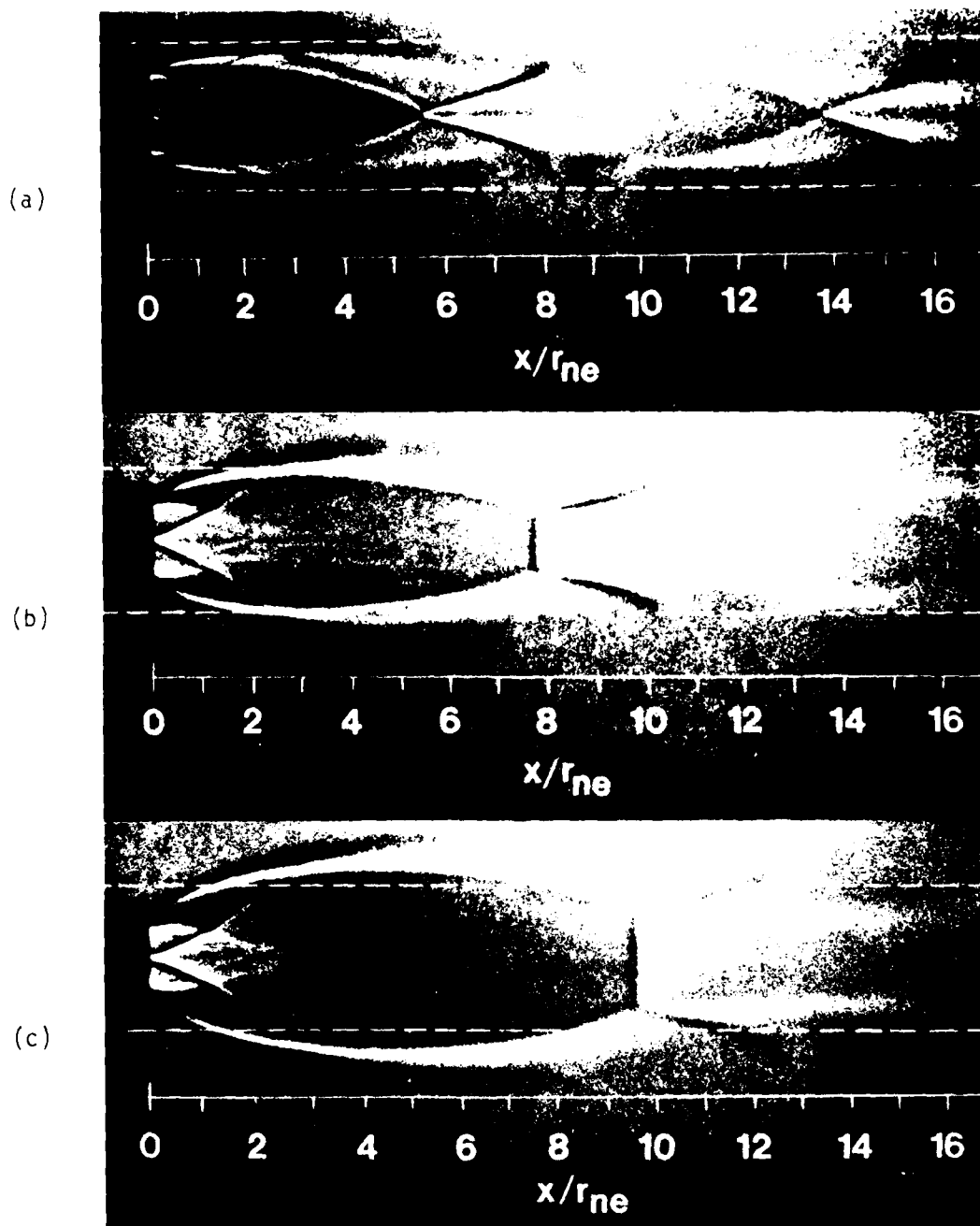


Figure 17. - Characteristics of the Free-Jet; (a) $p_{t1} = 2.76 \times 10^6 \text{ N/m}^2$ (400 psi); (b) $p_{t1} = 4.83 \times 10^6 \text{ N/m}^2$ (700 psi); (c) $p_{t1} = 7.69 \times 10^6 \text{ N/m}^2$ (1115 psi).

DELIBERATELY BLANK

discussed. Although the interaction between the impinging jet and the launcher will change the plume geometry, these photographs provide insights into the relation between the characteristic parameters and the impingement flow-field.

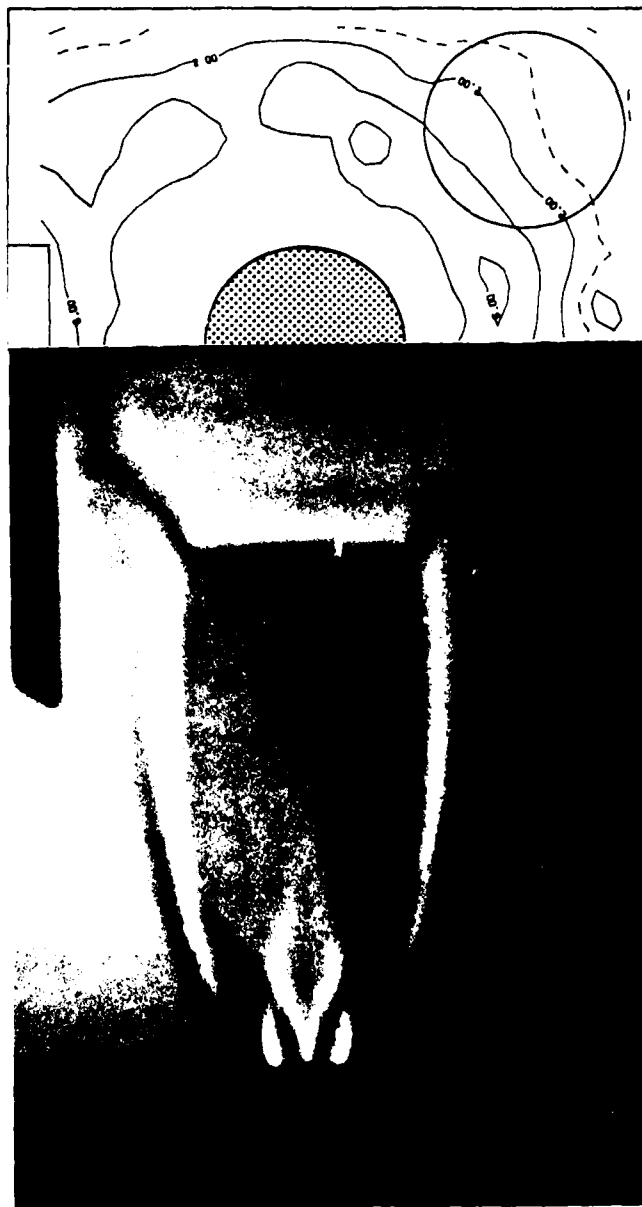
When the stagnation pressure is relatively low, the boundary of the free-jet plume does not intersect the launch-tube wall. Such is the case when $p_{t1} = 2.76 \times 10^6 \text{ N/m}^2$, as shown in Figure 17(a). At intermediate pressures, the free-jet plume is slightly larger than the internal diameter of the launch tube. This is illustrated in the shadowgraph for $p_{t1} = 4.83 \times 10^6 \text{ N/m}^2$, presented in Figure 17(b). At the highest stagnation pressures of the present program, a large portion of the free-jet plume lies outside the boundary of the launch tube. Refer to the shadowgraph of Figure 17(c) for $p_{t1} = 7.69 \times 10^6 \text{ N/m}^2$. The ratio of the diameter of the plume and the internal diameter of the launch tube is a dominant parameter in defining the impingement flow field. This ratio obviously depends on the stagnation pressure.

For purposes of this report, there were two characteristic impingement flow-fields: (1) subcritical, i.e., one in which almost all of the exhaust flow is swallowed by the open launch tube, and (2) supercritical, i.e., one in which a strong shock-wave system is formed and only a small fraction of the exhaust flow is swallowed by the open tube while a large fraction of the exhaust spreads over the face of the launcher. The supercritical flow occurs when the stagnation pressure and the distance from the nozzle-exit plane to the launcher surface are such that a strong shock wave is produced when the exhaust impinges on the rim of the tube. Because of the large decrease in stagnation pressure across the normal shock wave, the area of the launch tube is not large enough to pass all of the exhaust gases. The flow in the launch tube is "choked". As a result, a large fraction of the exhaust gases flow radially across the face of the launcher and only a small fraction continues down the tube. As will be discussed, the impingement flow-fields over the face of the launcher assembly for the supercritical flows and when $h > h_1^*$ of the present tests are similar to those described as type (4) for the solid plates, as discussed in the Introduction and as illustrated in Figures 2 and 3.

The characteristic features of a subcritical flow and of a supercritical flow are illustrated in the composite figures of Figure 18, in which a shadowgraph of the impinging exhaust has been superimposed on a graph of the experimentally-determined isobars from the face of the launcher assembly. The flow field depicted in Figure 18(a) is for a separation distance (h) of $10 r_{ne}$ with the reservoir pressure (p_{t1}) equal to $4.86 \times 10^6 \text{ N/m}^2$. That presented in Figure 18(b) was obtained

DELIBERATELY BLANK

DELIBERATELY BLANK



(b) Supercritical flow, $h = 10 r_{ne}$, $p_{t1} = 7.52 \times 10^6 \text{ N/m}^2$ (1090 psi).

Figure 18. - Concluded.

DELIBERATELY BLANK

at the same separation distances, i.e., h of $10 r_{ne}$, but with the reservoir pressure equal to $7.52 \times 10^6 \text{ N/m}^2$. Referring to Figures 17(b) and (17)c, it can be seen that the diameter of the free jet is significantly greater than that of the launch tube (d_t) for the higher stagnation pressure and approximately equal to d_t at the lower stagnation pressure. Thus, from the previous discussion, one would expect that the impingement flow field would be subcritical for the lower stagnation pressure and supercritical for the higher stagnation pressure. This was the case, as illustrated in Figures 18(a) and 18(b). This supports the assumption that the most important characteristic dimension is the ratio of the plume diameter to the launch-tube diameter.

Since the ratio of the plume diameter to the launch-tube diameter is a function of the stagnation pressure and of the separation distance between the nozzle-exit plane and the launcher, these two parameters can be used to characterize the impingement flow field. They are used in the following discussion to correlate the onset of transition from subcritical flow to supercritical flow. To those actually present when the tests were conducted, the most apparent indication of the transition from subcritical flow to supercritical flow was a dramatic change in the sound emitted by the impinging plume. Other, albeit less graphic, means (such as shock structure and pressure fields) could also be used to define the transition.

The transition values of the stagnation pressure are presented as a function of the nozzle-exit position (h/r_{ne}) in Figure 19. The open symbols represent the minimum stagnation pressure required to obtain supercritical flow. They were recorded as the chamber pressure was increased slowly. Once supercritical flow had been established, it could be maintained at lower stagnation pressures than those required to initiate it. This phenomenon is indicated by the filled symbols which represent the critical transition values of the stagnation pressure that were recorded as the chamber pressure was decreased. The filled symbols are consistently below the open symbols, indicating that once supercritical flow is established it can exist at lower stagnation pressures than those required to initiate it. The difference becomes more pronounced as the distance between the nozzle-exit plane and the face of the launcher increases.

It has been noted that a normal shock wave, or Mach disk, forms due to a coalescence of the compression waves for p_{t1} greater than $3.45 \times 10^6 \text{ N/m}^2$ (500 psi). For the free jet, the distance from the nozzle-exit plane to the Mach disk (\bar{x}_M) is $6.4 r_{ne}$, i.e., $\bar{x}_M = 6.4 r_{ne}$. As the stagnation pressure was increased, the Mach disk of the free jet moved downstream and increased in diameter. The down-

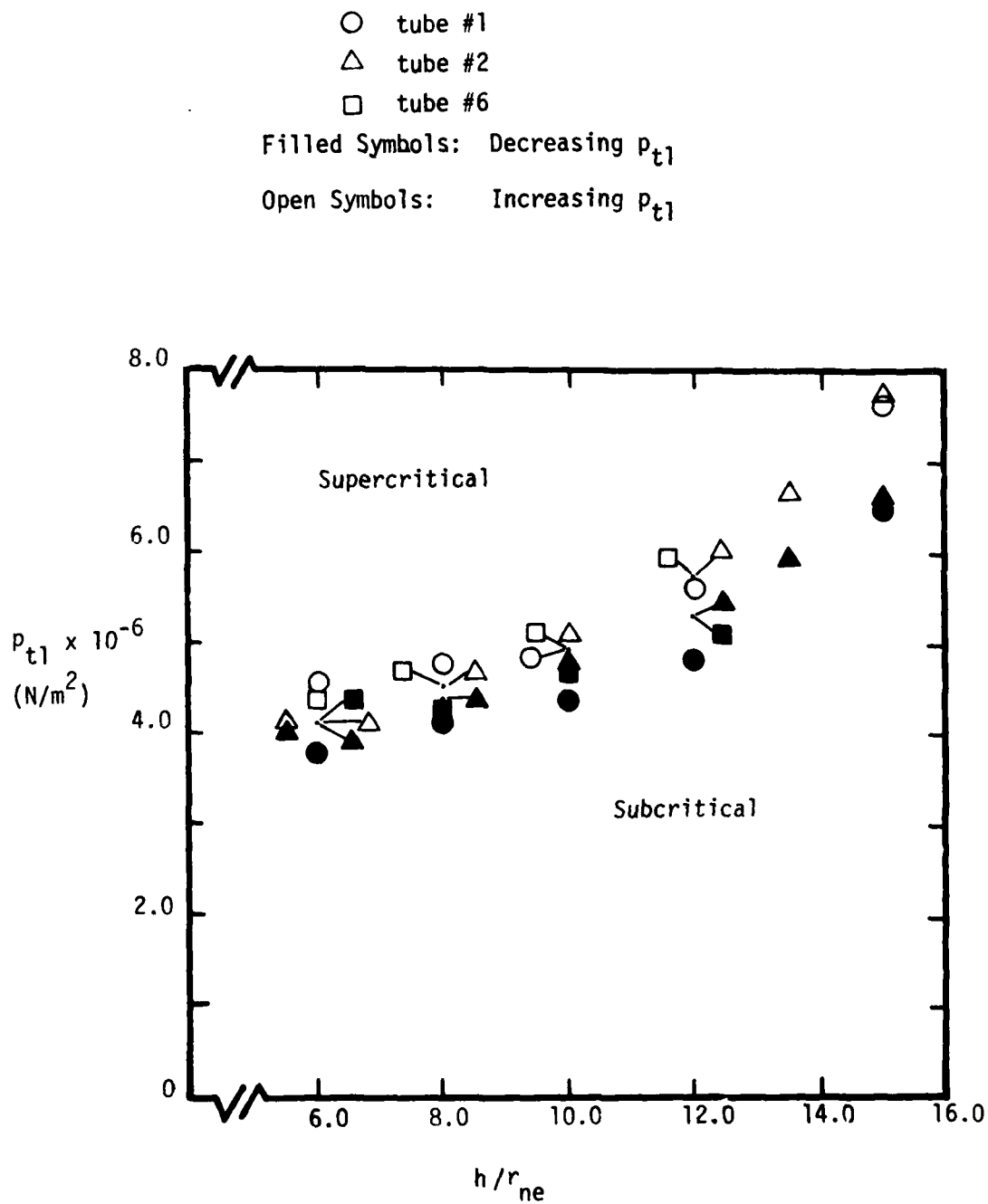


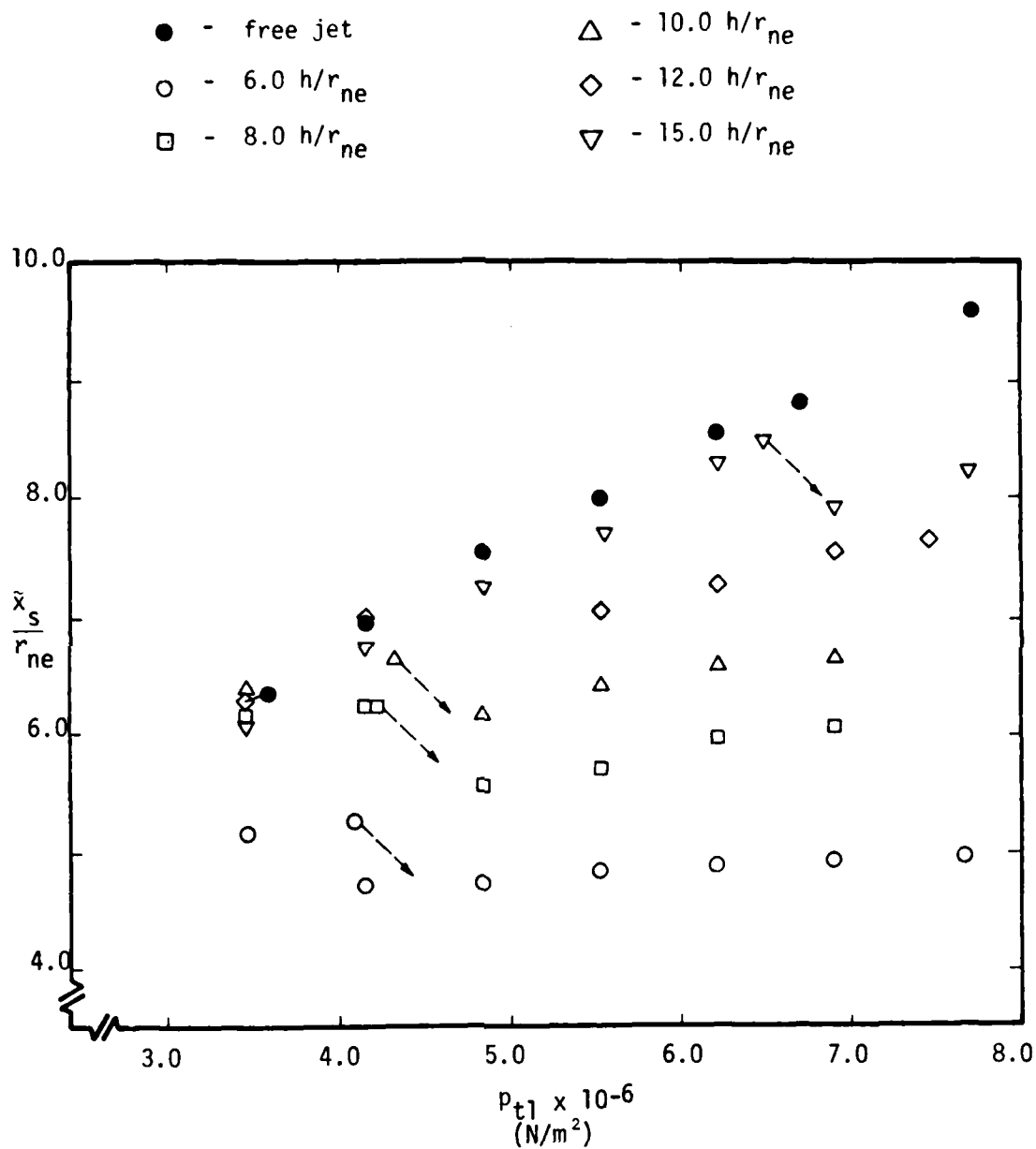
Figure 19. - Threshold values for the stagnation pressure required for the supercritical flow.

stream movement and growth of the free jet's Mach disk are illustrated by the filled symbols of Figure 20 and 21, respectively. The reader should note that the position and diameter of the Mach disk was measured from photographs of the flow field that were obtained as the chamber pressure was decreased. Thus, the critical pressures correspond to the filled symbols of Figure 19.

If the distance from the nozzle-exit plane to the face of the launcher (h) is much greater than the distance to the Mach disk of the free-jet (\tilde{x}_S for the filled symbols corresponds to \tilde{x}_M), one would not expect the presence of the launcher to have a significant effect on either the location or on the size of the Mach disk. This is verified by the data presented in Figures 20 and 21. Thus, for $p_{t1} = 3.45 \times 10^5 \text{ N/m}^2$ (500 psi), the Mach disk is between $6.0 r_{ne}$ and $6.5 r_{ne}$ from the nozzle-exit plane when the jet exhausts into the ambient atmosphere and when the launcher is $8.0 r_{ne}$, or more, away from the nozzle-exit plane, as shown in Figure 20. When the distance between the nozzle-exit plane and the launcher is $6.0 r_{ne}$, the shock is displaced by the presence of the launcher. This should not be surprising, since h is less than \tilde{x}_M for this case. Note that the presence of the launcher affects the location of the Mach disk for all but one of the configurations tested, i.e., $h = 15.0 r_{ne}$, when the stagnation pressure is $5.52 \times 10^6 \text{ N/m}^2$ (800 psi). Thus, the Mach disk is upstream of the free-jet location even when the distance from the nozzle-exit plane to the launcher is $12.0 r_{ne}$. The shock wave for the impinging jet is $7.07 r_{ne}$ from the nozzle-exit plane when $h = 12.0 r_{ne}$, where as it is $8.0 r_{ne}$ from the nozzle-exit plane for the free-jet.

These data indicate that, when the flow field is supercritical, the presence of the launcher can perturb the position of the Mach disk, even when h is relatively large. The perturbation in the location of the Mach disk (\tilde{x}_S/\tilde{x}_M) is presented in Figure 22 as a function of the ratio (h/\tilde{x}_M) which is the distance from the nozzle-exit plane divided by the distance to the Mach disk for the free jet. Included for comparison are the measurements for a jet impinging on a solid plate as reported by Ginzburg et al.⁹. Although the plate was solid for the Soviet tests but had large openings (the launch tubes) for the present tests, the correlation is essentially the same for both tests, when the flow is choked in the launch tube. Even when $h \approx 2\tilde{x}_M$, the Mach disk is moved approximately ten percent upstream

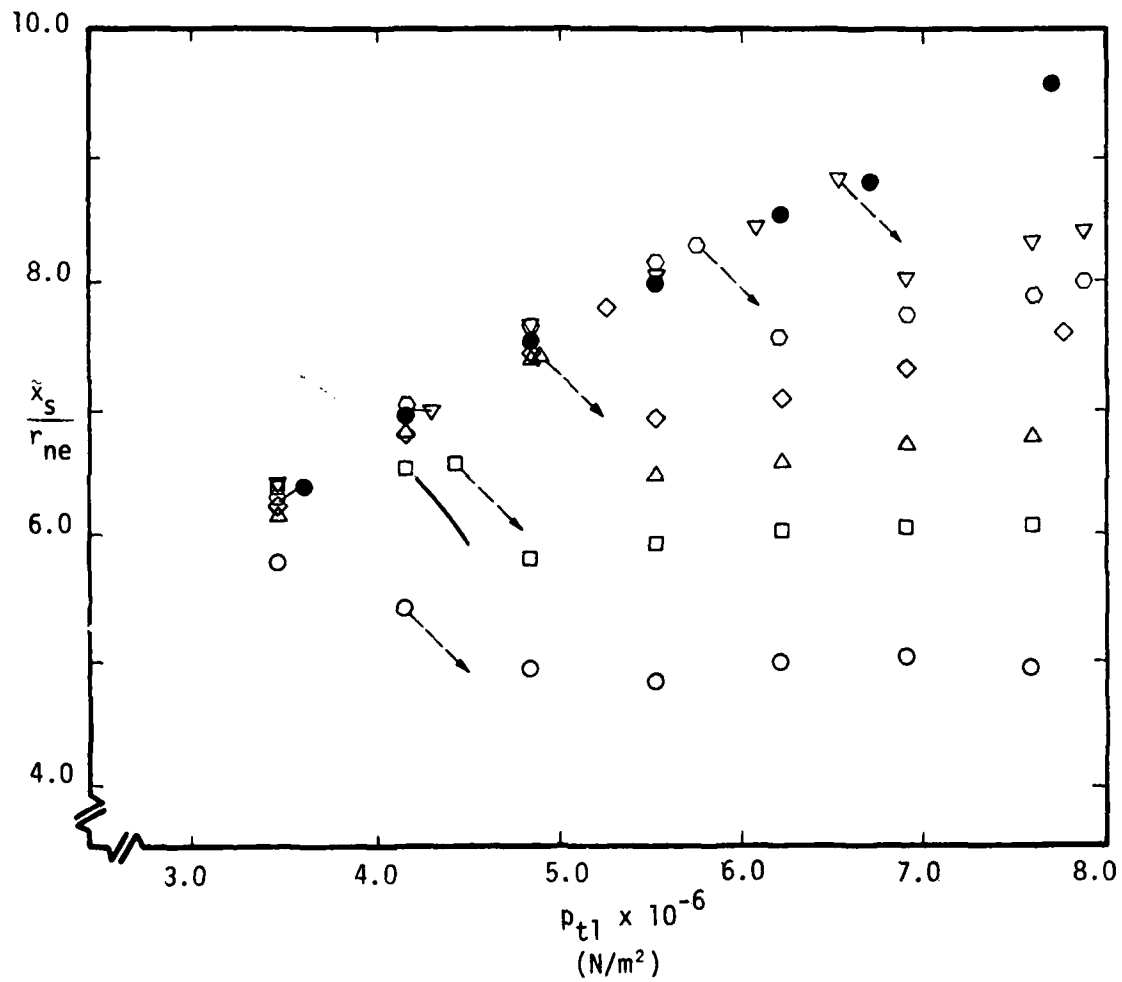
⁹ Ginzburg, I. P., Semiletchenko, B. G., and Uskov, V. N., "Experimental Study of Underexpanded Jets Impinging Normally on a Plane Baffle", Fluid Mechanics - Soviet Research, Vol. 4, No. 3, May - June 1975, pp. 93 - 105.



(a) Rocket "launched" from tube #1.

Figure 20. - Location of the Mach disc for the free jet and for impinging flows.

- - free jet
- - 6.0 h/r_{ne}
- - 8.0 h/r_{ne}
- △ - 10.0 h/r_{ne}
- ◇ - 12.0 h/r_{ne}
- ◯ - 13.5 h/r_{ne}
- ▽ - 15.0 h/r_{ne}



(b) Rocket "launched" from tube #2

Figure 20. - Concluded.

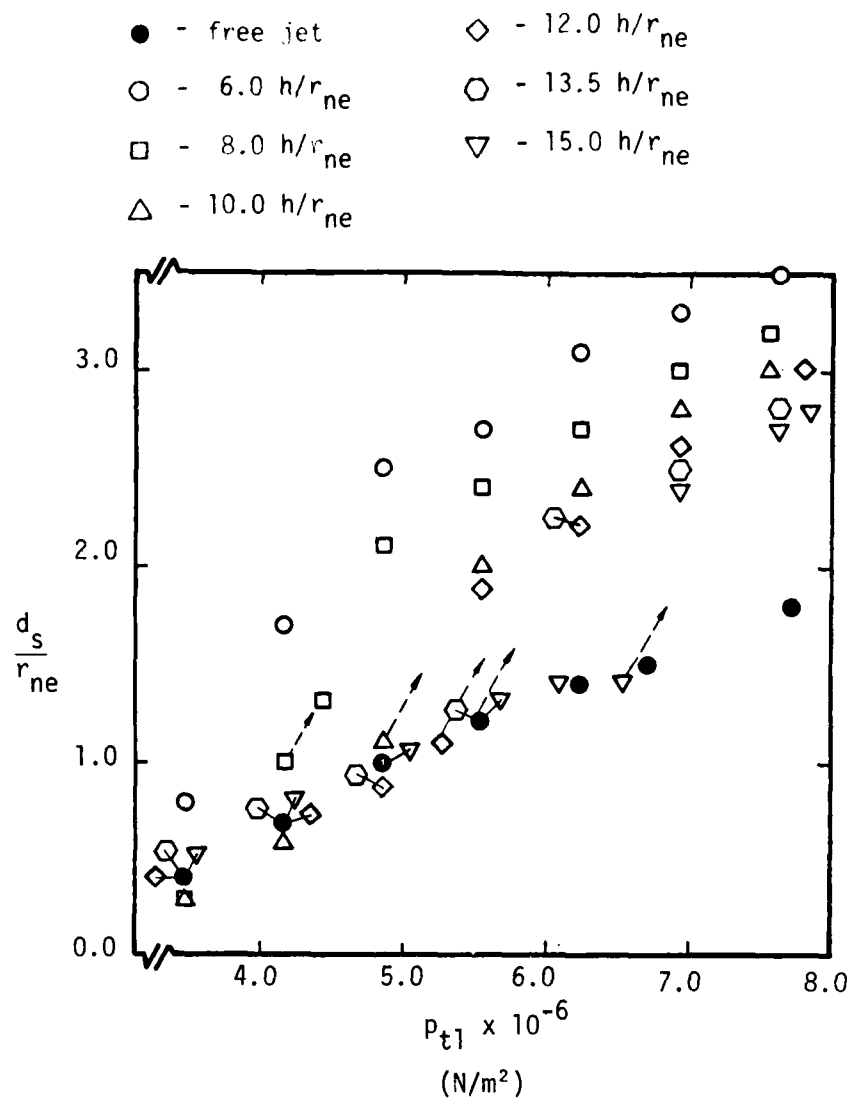


Figure 21. - Diameter of the Mach disc for the free jet and for impinging flows.

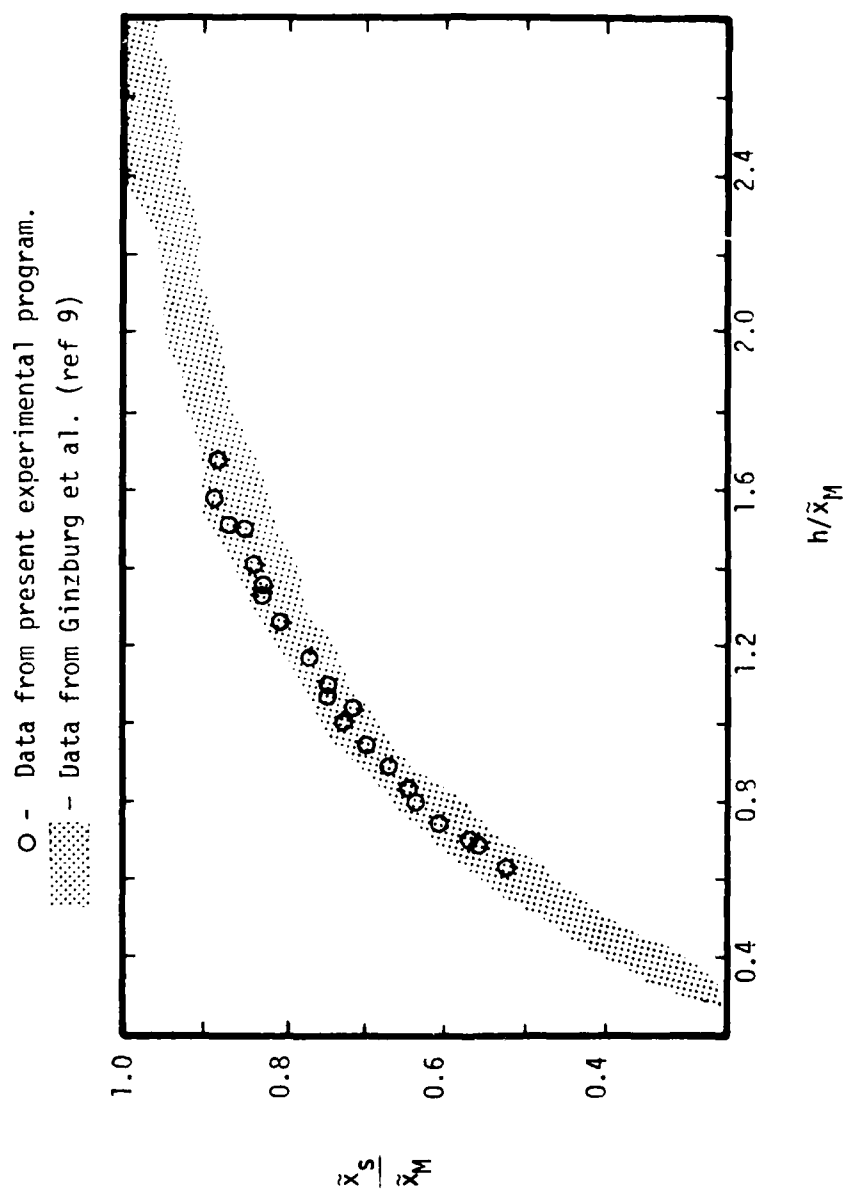


Figure 22. - Standoff Distance (from nozzle-exit plane to the Mach disk) as a function of separation distance (h).

from its unperturbed position.

When a critical stagnation pressure, i.e., the threshold pressure for a particular nozzle-exit position is exceeded, there is a sudden, discontinuous change in the geometry of the plume "barrel". The arrows of Figures 20 and 21 designate the sudden change. The change in plume geometry corresponds to the transition from a subcritical flow field to a supercritical one. Given a nozzle-exit position, the plume geometry, i.e., the distance between the nozzle-exit plane and the Mach disk and the diameter of the Mach disk, will be similar to that of the free jet if the chamber pressure is below the threshold stagnation pressure. In this case the flow is subcritical and very little of the exhaust flow interacts with the face of the launcher. Increasing the stagnation pressure to the threshold pressure results in a transition to supercritical flow. At this critical pressure, the Mach disk grows and stands further upstream of the launcher, thus decreasing \tilde{x}_S . At the same time the flow in the open launch-tube is choked.

When the flow field is supercritical, the measured pressure distributions from the present tests indicate that the separation distance corresponds to an h near h_1^* , or greater than h_1^* . As described in the Introduction, h_1^* denotes the separation distance between the nozzle-exit plane and the flat plate at which a zone of strong instability begins. For h less than h_1^* , the shock structure is stable with a static pressure distribution that has a maximum near the center of the impingement region. At the critical value of h , i.e., h_1^* , the static pressure at the centerline has decreased until the pressure distribution is constant across the plate. The Mach disk begins to fluctuate at a high frequency. A correlation developed by Ginzburg et al.⁹ for flow impinging on a flat plate indicates that this zone of instability begins when $h_1^*/\tilde{x}_M = (1.08 - 0.17 M_{ne})$.

The nozzle used in the present experimental program had an exit Mach number of 2.32. Based on the correlation of Ginzburg et al., the strong instability zone should begin at $h_1^*/\tilde{x}_M = 0.687$. However, the present data do not provide information as to what effect the tube opening might have on the instability zone. Also, the Soviet researchers do not clearly define the upper limit of the strong instability zone. Therefore, once a supercritical flow field is established on the launcher it is difficult to determine whether the nozzle is positioned

⁹ Ginzburg, I. P., Semiletenko, B. G., and Uskov, V. N., "Experimental Study of Underexpanded Jets Impinging Normally on a Plane Baffle", Fluid Mechanics - Soviet Research, Vol. 4, No. 3, May - June 1975, pp. 93 - 105.

upstream or downstream of this zone. During the present test program only one instance of shock instability was recorded. The shadowgraph of the impingement flow field for $h = 6.0 r_{ne}$ and for a stagnation pressure of $4.206 \times 10^6 \text{ N/m}^2$ is presented in Figure 23. Even though $h/\bar{x}_M = 0.86$, which is greater than the calculated value of h_1^* for this configuration, the shock is clearly unstable. A comparison of the pressure distributions for the impingement flow field on the launcher and those on a solid plate will assist in defining the zone of instability. The pressure distributions measured on the face of the launcher assembly will be discussed in the next section.

4.2 Pressure Distributions on the Face of the Launcher Assembly

The data acquired during this experimental program included measurements of the static pressure distributions on the launcher assembly when a simulated rocket exhaust impinged on its face. These pressures were measured while simulating a rocket launch from tube 1, tube 2, or tube 6. However, the general characteristics of the impingement flow field associated with each tube were very similar. Therefore, only the pressure data obtained for "launches" from tube 2 will be presented. The trends in the pressure distributions will be analyzed by comparing the data for two parametric variations: (1) for various stagnation pressures with the separation distance, i.e., h , held fixed; (2) for various separation distances at a given stagnation pressure.

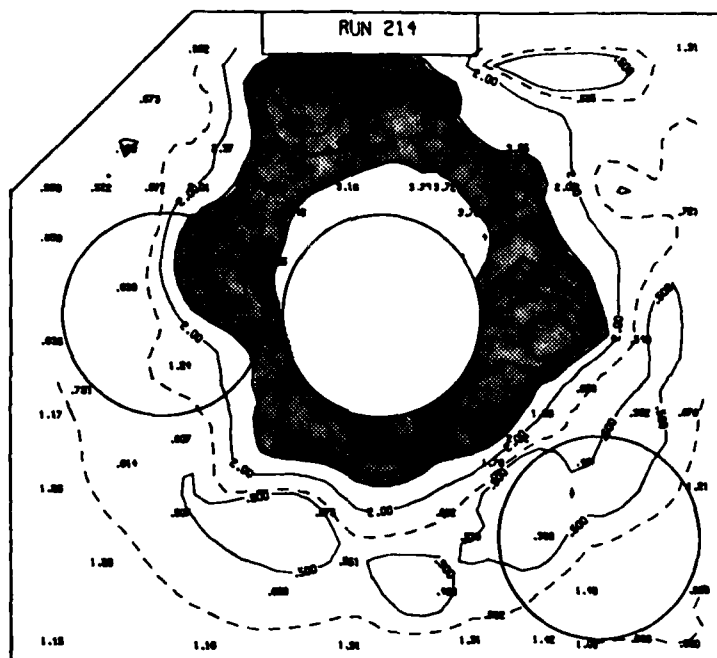
The static pressure distributions are presented as isobaric contours for $h = 8.0 r_{ne}$ and $h = 12.0 r_{ne}$ in Figures 24 and 26, respectively. Data are presented for stagnation pressures from $7.58 \times 10^6 \text{ N/m}^2$ to $2.71 \times 10^6 \text{ N/m}^2$. Both isobars and the individual pressure measurements are represented on these maps in atmospheres. When the separation distance is $8.0 r_{ne}$, the threshold stagnation pressure required for supercritical flow is $4.5 \times 10^6 \text{ N/m}^2$ (see Figure 19). Therefore, at stagnation pressures above $4.5 \times 10^6 \text{ N/m}^2$, a significant fraction of the plume should be impinging on the face of the launcher assembly. The pressure contours presented in Figures 24(a), (b), and (c) exhibit the high pressure regions, i.e., four atmospheres and above, which are shaded so that they can be more easily seen. A relatively large region of high pressure exists near the rim of the launch tube for $p_{t1} > 4.5 \times 10^6 \text{ N/m}^2$. Moving radially outwards, the pressure first increases reaching a ring of "local maxima". The pressure then decreases until a band of sub-atmospheric pressure is reached. This low pressure region is due to the local turning and subsequent acceleration of the flow as it spreads across the face of the launcher. The pressure distributions presented in Figures 24(b) and (c) are very similar. This similarity should be expected, since the chamber pressures are nearly equal. These two

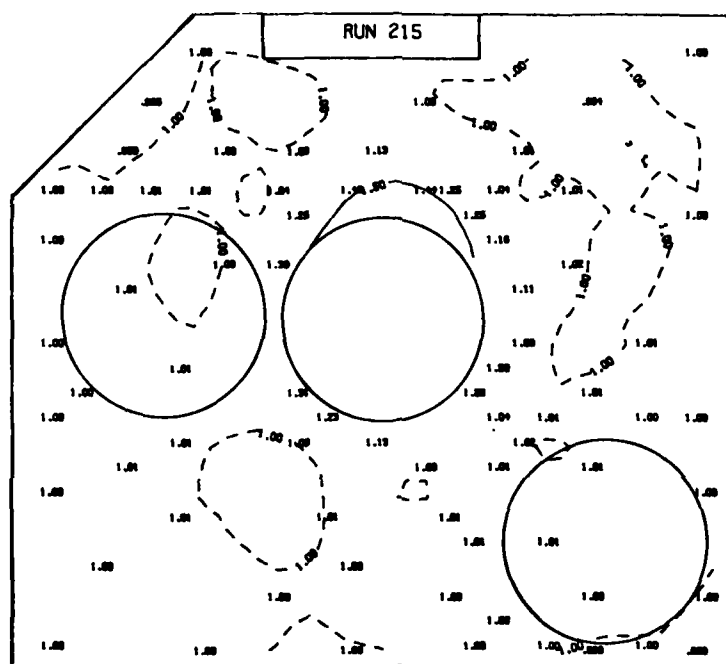
DELIBERATELY BLANK



Figure 23. - Shadowgraph of the unstable Mach disc at $h = 6.0 r_{ne}$ and $p_{t1} = 4.206 \times 10^6 \text{ N/m}^2$.

DELIBERATELY BLANK





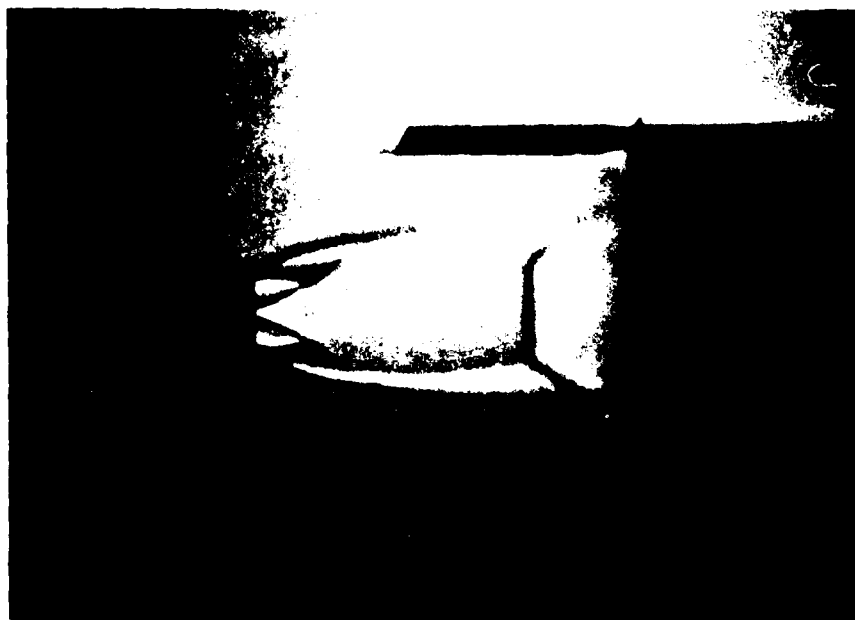
(e) $p_{t1} = 2.71 \times 10^6 \text{ N/m}^2$

Figure 24. - Concluded.

DELIBERATELY BLANK



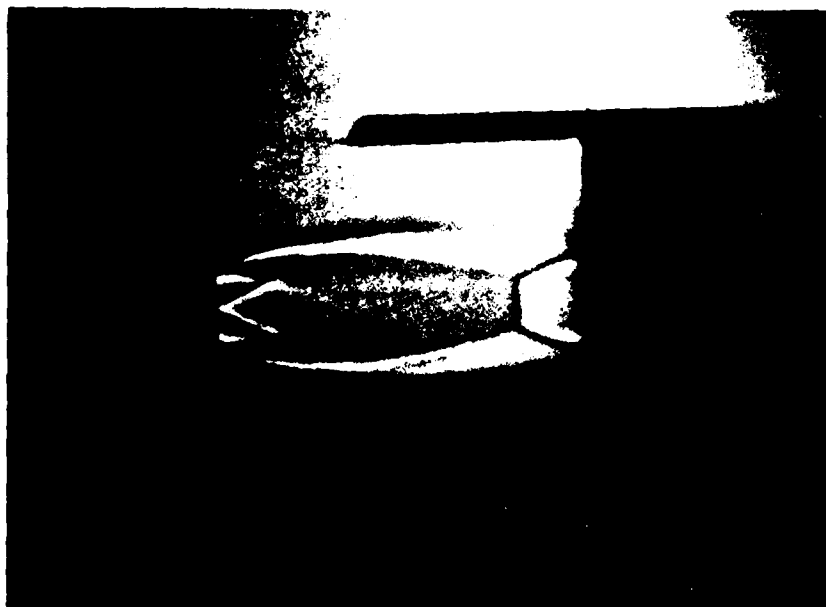
(a) $p_{t1} = 7.52 \times 10^6 \text{ N/m}^2$



(b) $p_{t1} = 4.83 \times 10^6 \text{ N/m}^2$

Figure 25. - Shadowgraphs of plume impingement (tube 2), $h = 8.0 r_{ne}$.

DELIBERATELY BLANK



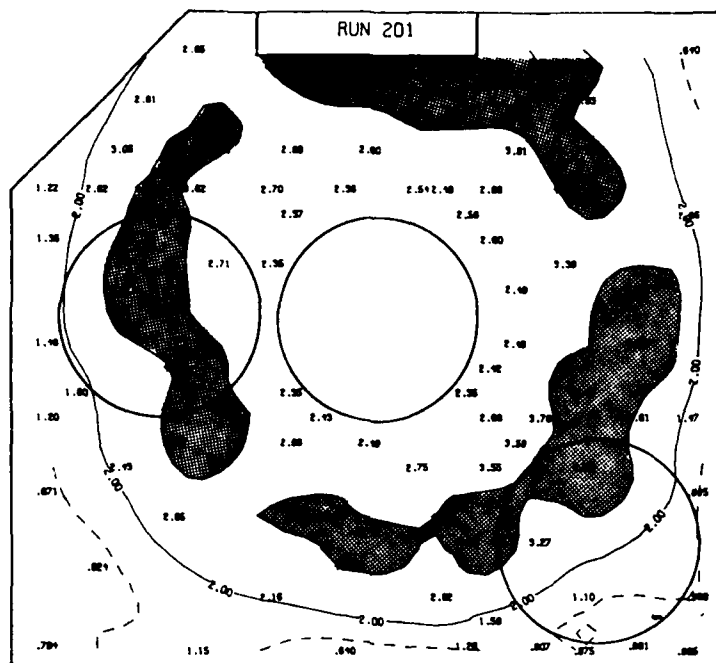
$$(c) p_{t1} = 4.14 \times 10^6 \text{ N/m}^2$$



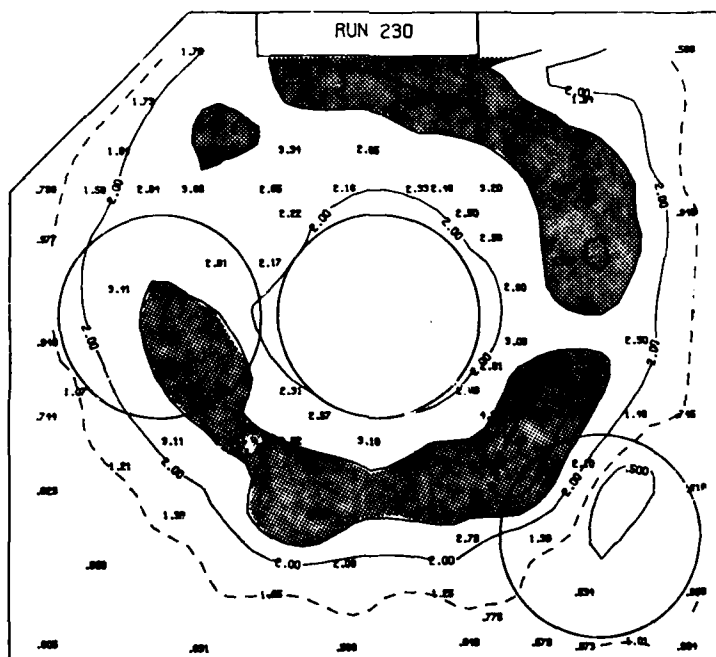
$$(d) p_{t1} = 2.76 \times 10^6 \text{ N/m}^2$$

Figure 25. - Concluded.

DELIBERATELY BLANK

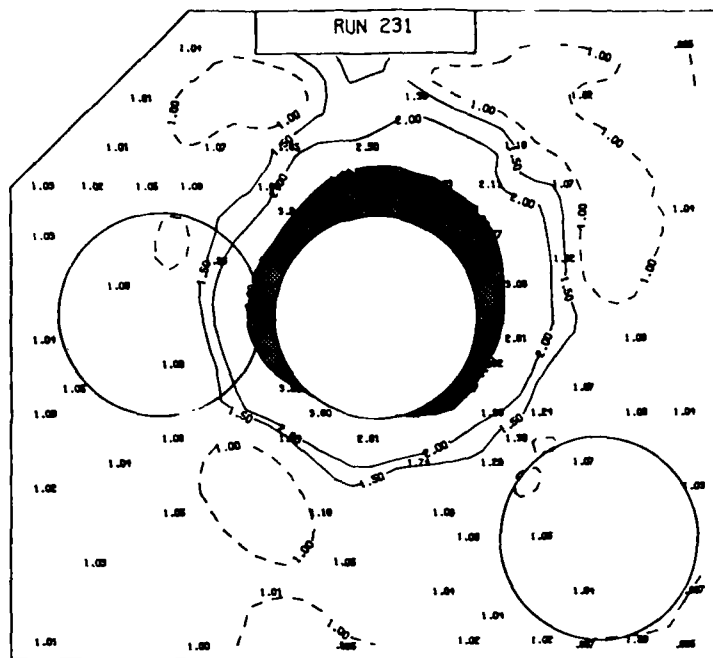


(a) $p_{t1} = 7.58 \times 10^6 \text{ N/m}^2$

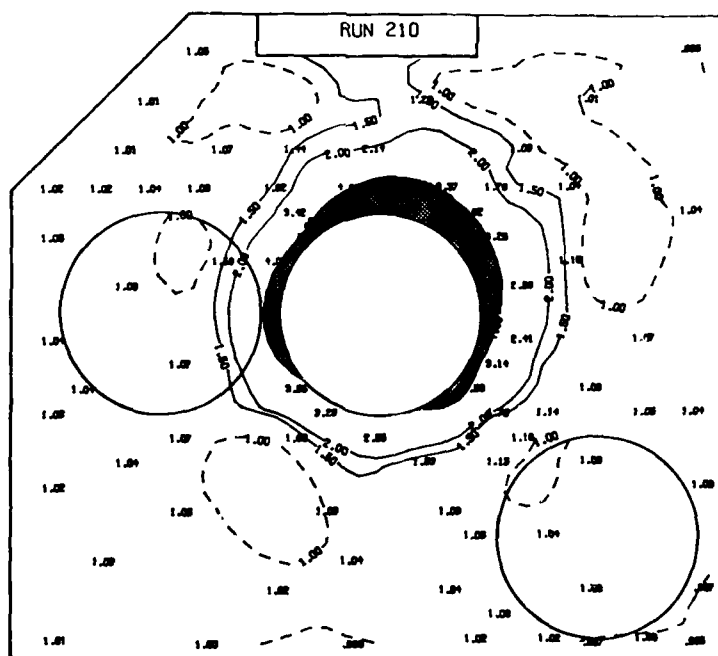


(b) $p_{t1} = 6.00 \times 10^6 \text{ N/m}^2$

Figure 26. - Static pressure distributions (tube 2), $h = 12.0 r_{ne}$

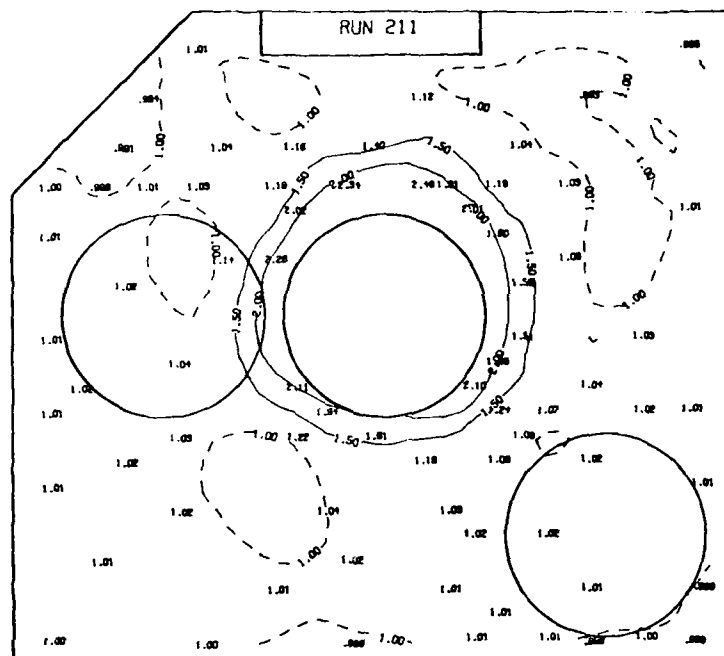


(c) $p_{t1} = 5.33 \times 10^6 \text{ N/m}^2$



(d) $p_{t1} = 4.72 \times 10^6 \text{ N/m}^2$

Figure 26. - Continued.



$$(e) p_{t1} = 2.71 \times 10^6 \text{ N/m}^2$$

Figure 26. - Concluded.

contour maps reflect the repeatability of the data. The reader should also note the "low" pressure region above and near the rim of tube 2, the tube from which the rocket is "launched". This region suggests that the impinging plume was asymmetric. One probable cause of the asymmetry was a slight rotation of the launcher assembly being acted upon by the pressure loads of the impinging plume. The fact that pressures lower than the peripheral pressures exist in this region suggest that the separation distance (h) is greater than h_1^* , i.e., is beyond the zone of instability. Recall from the discussion in the Introduction, that when $h = h_1^*$ the pressure distribution across the impingement region is constant. When h exceeds h_1^* , the pressures in the central region decrease and the maximum pressures occur at the periphery of the impingement region. Referring to Figure 20, the value of h/\tilde{x}_M is 0.84 and 1.06 for Figures 24(a) and (b), respectively. Since these values of h/\tilde{x}_M are greater than h_1^*/\tilde{x}_M calculated, the pressure distributions are consistent with those expected.

If the stagnation pressure is decreased below $4.5 \times 10^6 \text{ N/m}^2$, the flow field is subcritical, i.e., most of the exhaust gases are swallowed by the open tube. Isobar maps for subcritical flows at $h = 8.0 r_{ne}$ are presented in Figures 24(d) and (e). As should be expected, only a small area near the rim of the launch tube is affected by the plume. Shadowgraphs of subcritical and supercritical flow fields, corresponding to the pressure distributions illustrated in Figure 24, are presented in Figure 25. The shadowgraphs support the observations made using the pressure data. It can be seen that, when the stagnation pressure is less than $4.5 \times 10^6 \text{ N/m}^2$, most of the exhaust flow is swallowed by the open tube, i.e., the flow is subcritical.

The isobar maps presented in Figure 26 illustrate the dramatic change in pressure distribution from supercritical to subcritical flows, as the nozzle-exit plane moves further from the face of the launcher. If the value of h is greater than h_1^* and if the flow is supercritical, i.e., a large fraction of the exhaust flow impinges on the face of the launcher, high pressures act over a large area of the face. The peak pressures occur near the periphery of the impingement region. The rings of relatively high pressure at the periphery are clearly evident in Figures 26(a) and (b). For subcritical flows, "high" pressures occur only in a small area near the rim of the launch tube, where the viscous shear layer at the plume boundary impinges on the face of the launcher. Most of the exhaust gases continue down the open tube.

However, the chamber pressure also has a more subtle effect on the pressure distribution. First, recall that the shock structure for supercritical flows is similar to that illustrated in Figure 2. Also, recall that the diameter of the central shock wave (CSW) is a function of stagnation pressure as well as other parameters (see

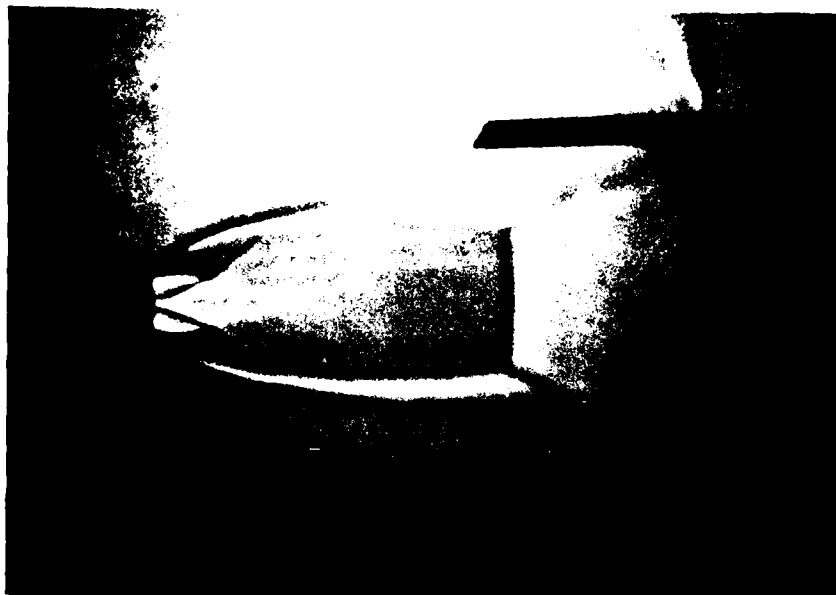
Figure 21). Since the pressure drop across a normal shock wave, or the Mach disk, is greater than that across an oblique shock, i.e., the reflected shock wave (RSW), then increasing the diameter of the Mach disk, by increasing the stagnation pressure, the flow will spread radially outward and the location of the high pressure peripheral region will also move outward. This phenomenon is illustrated in the isobar maps of Figure 26(a) and (b), and in the shadowgraphs of Figure 27(a) and (b). Shadowgraphs of some subcritical flows at $h = 12.0 r_{ne}$ are also presented in Figure 27.

In order to more clearly understand the effect that the separation distance (h) has on the pressure distributions, data are presented in Figures 28 to 33 for various separation distances with the stagnation pressure held fixed. Isobaric contour maps are presented in Figures 28, 30, and 32 for chamber pressures of $7.58 \times 10^6 \text{ N/m}^2$, $4.83 \times 10^6 \text{ N/m}^2$, and $2.76 \times 10^6 \text{ N/m}^2$, respectively. The intermediate figures, Figures 29, 31, and 33, present shadowgraphs of the impingement flow field at the corresponding stagnation pressures and separation distances.

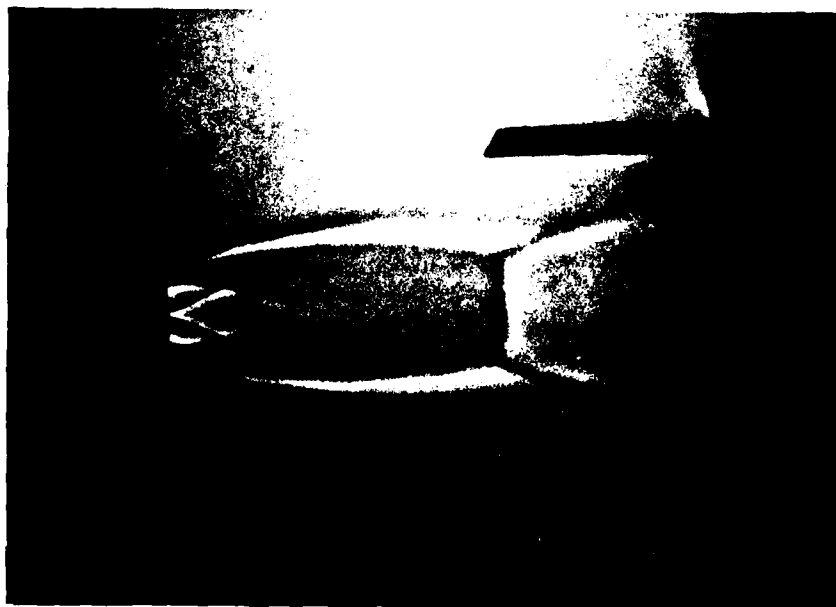
Data for a relatively large stagnation pressure, i.e., approximately $7.58 \times 10^6 \text{ N/m}^2$, are presented in Figures 28 and 29. As discussed earlier, the impingement flow field is supercritical for $4.0 \leq h \leq 15.0 r_{ne}$. Even when $h = 2.0 r_{ne}$, at this stagnation pressure, Figure 28(a), the impinging exhaust flow affects the pressures in a mid-sized region near the open tube. Although the rapidly expanding impingement plume creates a relatively strong shock, most of the exhaust gases are swallowed by the open launch tube. The static pressure distributions presented in Figures 28(b), (c), (d), and (e) indicate that a large fraction of the face of the launcher is affected by the exhaust flow. The isobar contours of Figures 28(b) and (c) correspond to separation distances less than h_j^* , i.e., $h < 0.687 \tilde{x}_M$, while those presented in Figures 28(d) and (e) correspond to $h > h_j^*$. As h approaches h_j^* , the high pressure region spreads radially across the plate with the peak pressures decreasing. For $h > h_j^*$, the static pressures near the tube opening decrease. However, locally high pressures occur near the periphery of the jet impingement region. Shadowgraphs of the simulated rocket exhaust impinging on the launcher assembly are presented for $p_{t1} \approx 7.58 \times 10^6 \text{ N/m}^2$ in Figure 29. Note, there is a definite oblique, reflected shock wave near the periphery of the impinging plume for $h = 10.0 r_{ne}$ and $15.0 r_{ne}$ which does not appear in the shadowgraphs for $h = 4.0 r_{ne}$ and begins to appear for $h = 6.0 r_{ne}$.

At an intermediate stagnation pressure, i.e., $p_{t1} \approx 4.83 \times 10^6 \text{ N/m}^2$, the separation distance determines whether the flow field is supercritical or subcritical. The relevant data are presented in Figure 30 and 31. When the nozzle-exit plane is near the launcher,

DELIBERATELY BLANK



(a) $p_{t1} = 7.62 \times 10^6 \text{ N/m}^2$



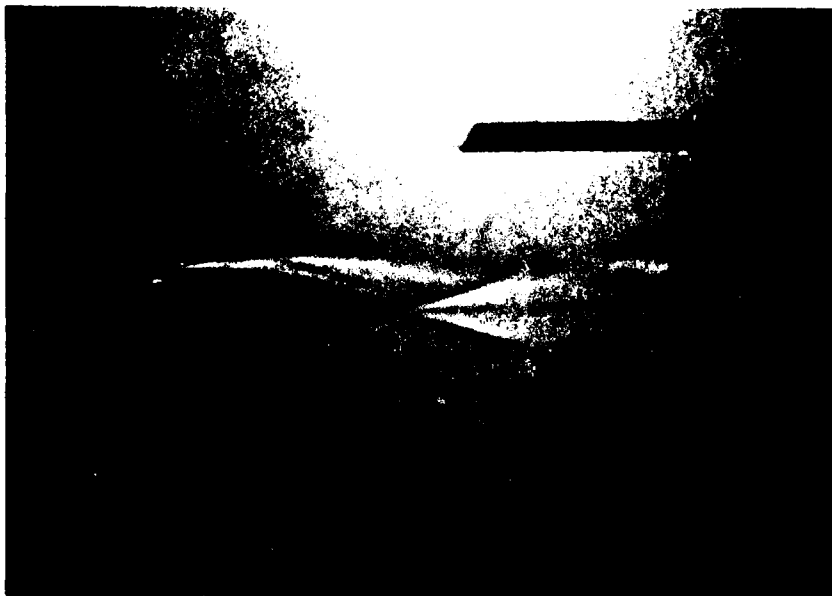
(b) $p_{t1} = 6.21 \times 10^6 \text{ N/m}^2$

Figure 27. - Shadowgraphs of plume impingement (tube 2), $h = 12.0 r_{ne}$.

DELIBERATELY BLANK



(c) $p_{t1} = 5.24 \times 10^6 \text{ N/m}^2$



(d) $p_{t1} = 2.76 \times 10^6 \text{ N/m}^2$

Figure 27. - Concluded.

DELIBERATELY BLANK

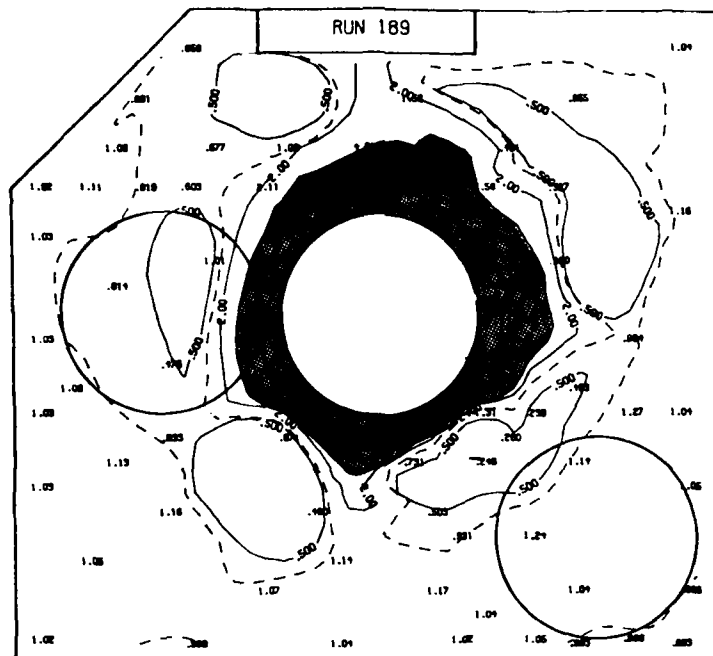
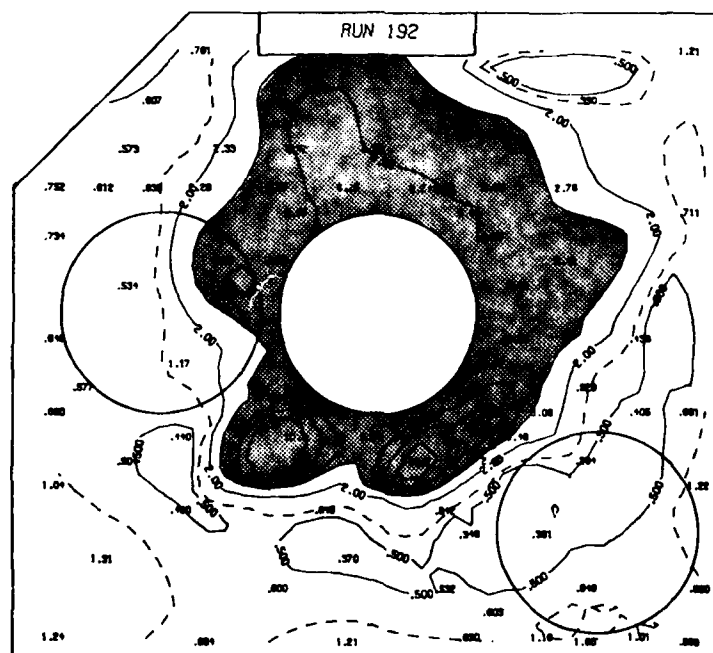
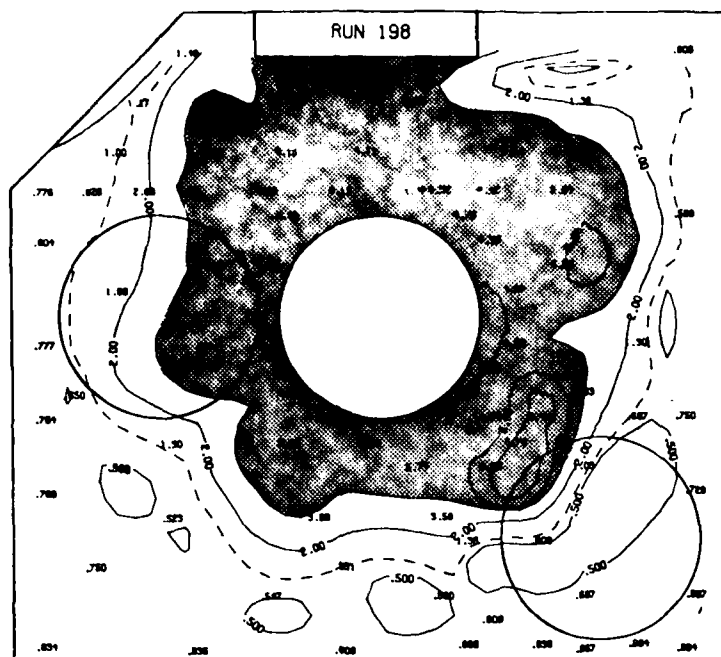
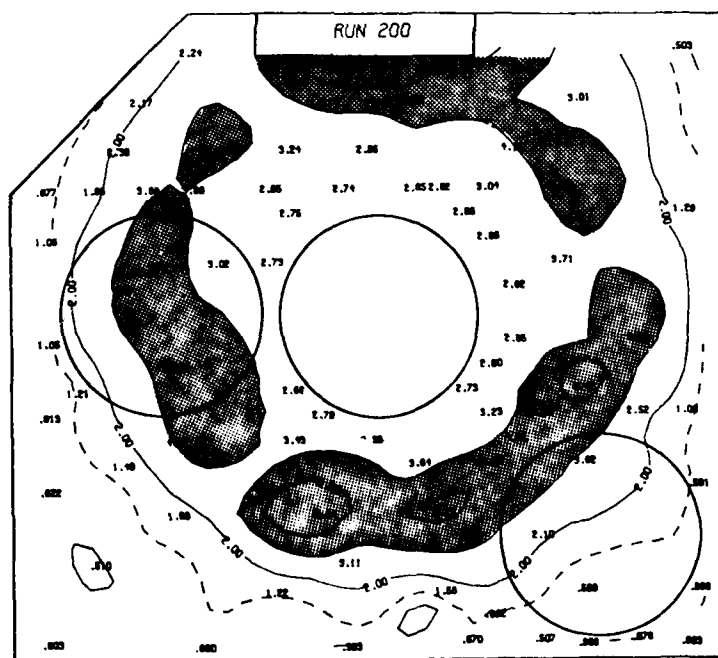

$$(a) \quad h = 2.0 \quad r_{ne} = 0.21 \quad \tilde{x}_m$$

$$(b) \quad h = 4.0 \, r_{ne} = 0.42 \, \tilde{x}_m$$

Figure 28. - Static pressure distributions (tube 2), $p_{t1} = 7.50 \times 10^6 \text{ N/m}^2$.

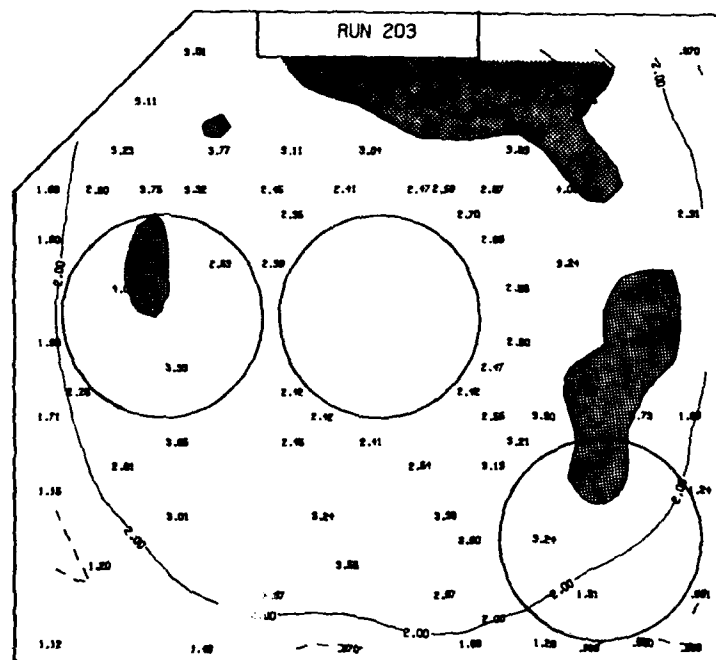


(c) $h = 6.0 \text{ } r_{ne} = 0.63 \tilde{x}_M$



(d) $h = 10.0$ $r_{ne} = 1.05 \tilde{x}_M$

Figure 28. - Continued.



(e) $h = 15.0$ $r_{ne} = 1.56 \bar{x}_M$

Note: Flow is supercritical

Figure 28. - Concluded.

DELIBERATELY BLANK

AD-A119 386

TEXAS UNIV AT AUSTIN FLUID DYNAMICS INST
IMPINGEMENT FLOW-FIELDS FOR TUBE-LAUNCHED ROCKETS.(U)

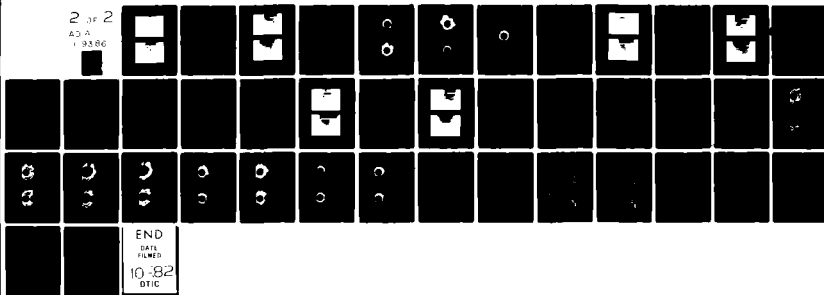
F/6 21/2

AUG 82 S A BOUSLOG, J J BERTIN, W B WINGERT DAAH01-81-C-8078
82-101 ORSMI/RL-CR-82-5 NL

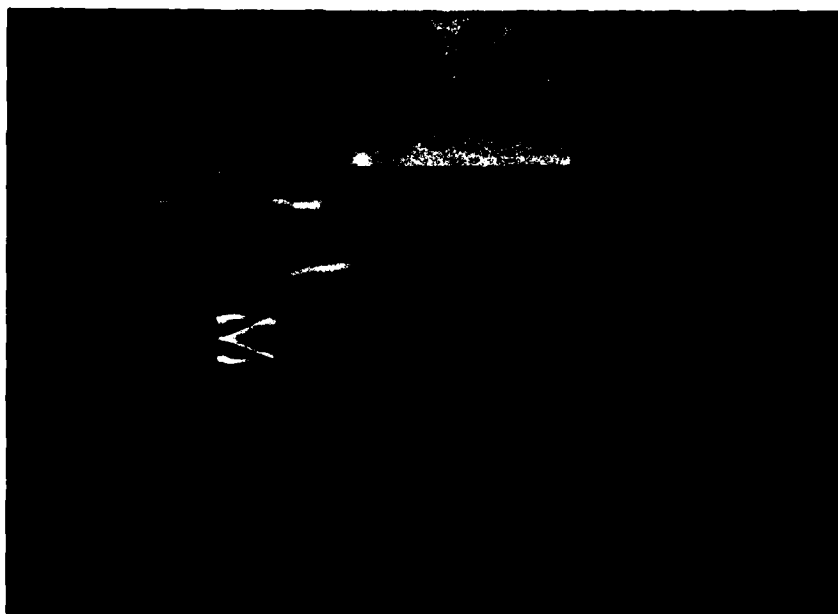
UNCLASSIFIED

2 of 2

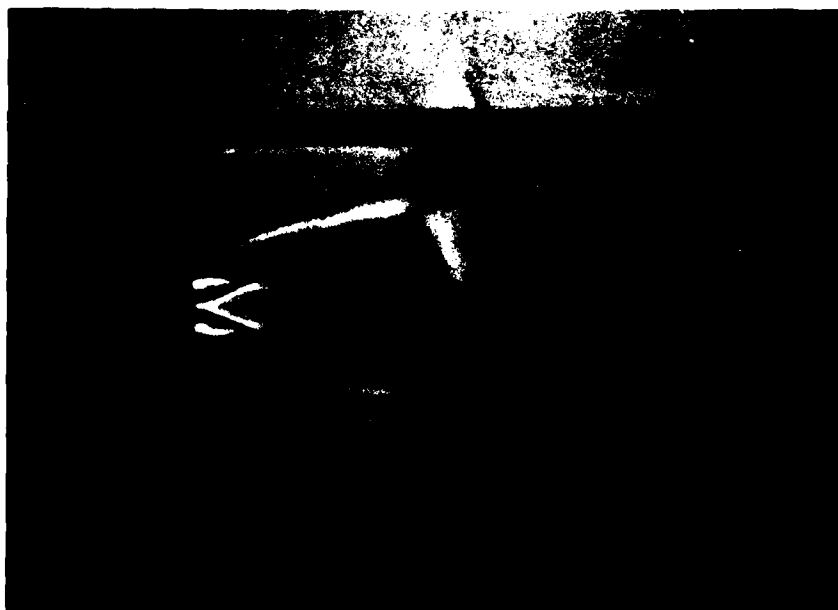
43 A
1 93 86



END
DATE
FILMED
10-82
DTIC



(a) $h = 4.0 r_{ne}$



(b) $h = 6.0 r_{ne}$

Figure 29. - Shadowgraphs of the plume impingement (tube 2), $p_{t1} \approx 7.58 \times 10^6 \text{ N/m}^2$.

DELIBERATELY BLANK



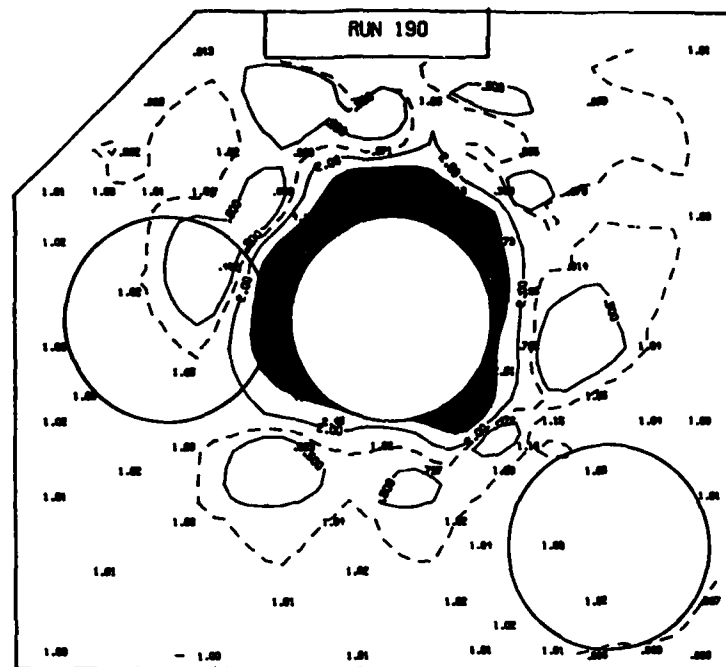
(c) $h \approx 10.0 r_{ne}$



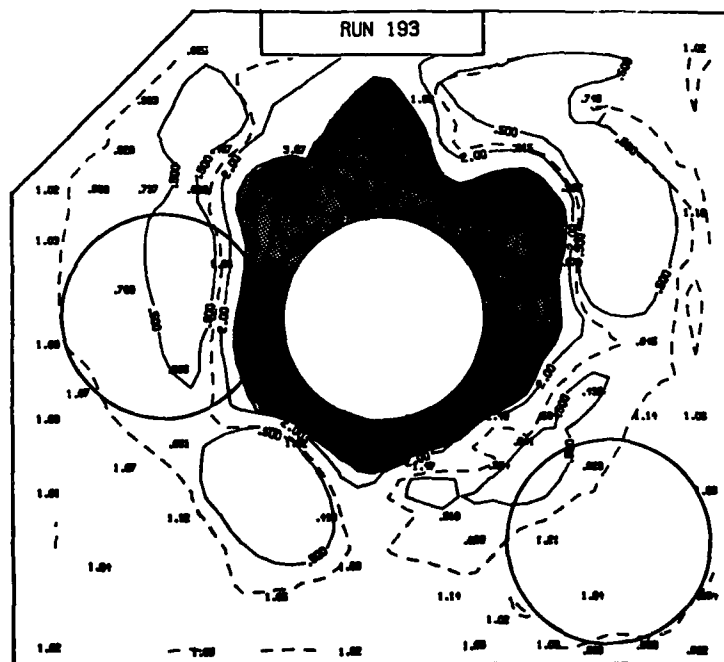
(d) $h = 15.0 r_{ne}$

Figure 29. - Concluded.

DELIBERATELY BLANK

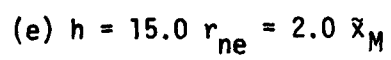


(a) $h = 2.0$ $r_{ne} = 0.27 \tilde{x}_M$



(b) $h = 4.0$ $r_{ne} = 0.53 \tilde{x}_M$

Figure 30. - Static pressure distributions (tube 2), $p_{t1} \approx 4.83 \times 10^6 \text{ N/m}^2$.



101

DELIBERATELY BLANK



(a) $h = 4.0 r_{ne}$



(b) $h = 6.0 r_{ne}$

Figure 31. - Shadowgraphs of the plume impingement (tube 2), $p_{t1} \approx 4.83 \times 10^6 \text{ N/m}^2$.

DELIBERATELY BLANK



(c) $h = 10.0 r_{ne}$



(d) $h = 15 r_{ne}$

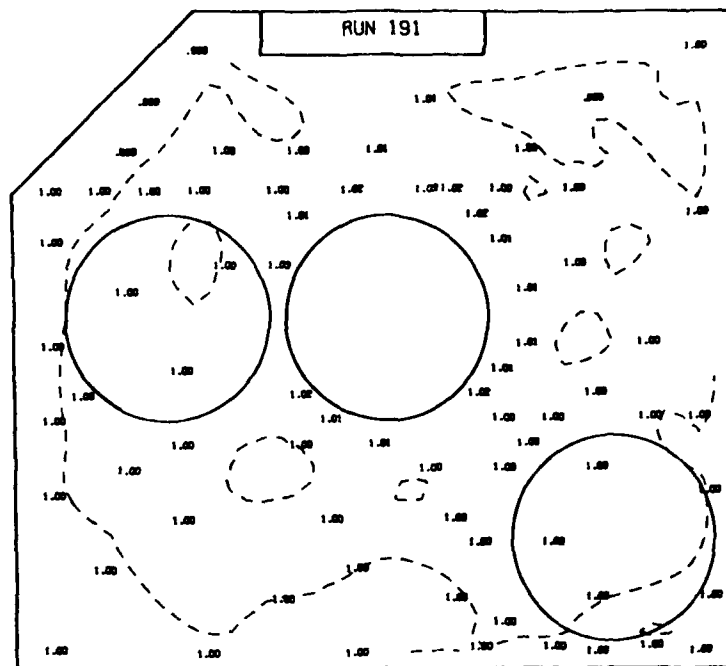
Figure 31. - Concluded.

DELIBERATELY BLANK

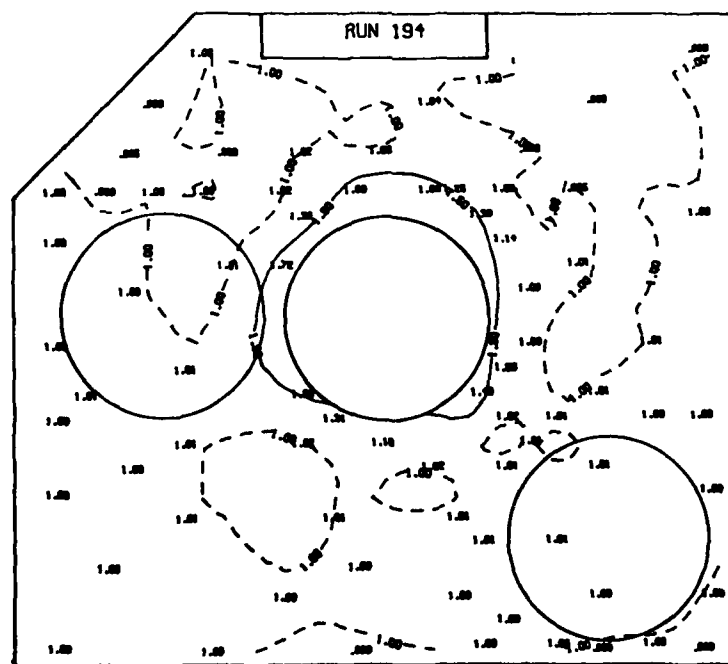
some of the exhaust flow impinges on the rim of the open tube and spreads across the face of the launcher. But, most of the exhaust gases continue down the tube. The pressure distribution is presented in Figure 30(a) for $h = 2.0 r_{ne}$. As the separation distance is increased, more of the exhaust plume interacts with the face of the launcher, and the flow becomes supercritical. The isobaric contours presented in Figures 30(b) and (c) are typical of those for supercritical flows where h is near h_1^* . However, further increases in h result in a subcritical flow field, as exhibited in Figures 30(d) and (e). The shadowgraphs presented in Figure 31 assist in defining the effect that the separation distance has on the flow field and on the pressure distributions. A special note should be made of the differences in pressure distribution when $h = 10.0 r_{ne}$ and when $h = 15.0 r_{ne}$, as shown in Figures 30(d) and (e). At the larger separation distance, $h = 15.0 r_{ne}$, a larger region of high pressure exists in the region of the open tube, than at $h = 10.0 r_{ne}$. When the nozzle-exit plane is relatively far from the face of the launcher at this stagnation pressure, viscous effects apparently have entrained the surrounding air.

At the lowest stagnation pressure tested, i.e., $p_{t1} \approx 2.76 \times 10^6 \text{ N/m}^2$, the plume is of the same size as the tube diameter. Thus, any effect of the exhaust plume on the pressure distribution is limited to the region near the edge of the open tube. The isobar maps and shadowgraphs for this stagnation pressure are presented in Figures 32 and 33.

Note that, when $h < h_1^*$, the maximum pressure on the face of the launcher assembly occurs near the edge of the open launch tube. When $h > h_1^*$, the maximum pressure occurs near the periphery of the impinging plume. At this point, it is useful to investigate the maximum pressures measured on the face of the launcher assembly. The flow-field characteristics that affect the maximum pressures are best illustrated in the data presented in Figure 34. Presented are the maximum pressures measured on the face of the launcher assembly as the model rocket was "launched" from tube 6. The data for $p_{t1} \approx 7.58 \times 10^6 \text{ N/m}^2$ are presented as a function of h/r_{ne} . When the nozzle-exit plane is relatively near the surface, i.e., $h < h_1^*$, the viscous/inviscid interaction is dominated by the normal shock wave that spans the impinging plume. This is shown in the sketch of Figure 34(b). As a result, the pressure on the face of the launcher is equal to the pressure downstream of a normal shock wave and is relatively high. As the rocket moves away from the launcher, the pressure downstream of the normal shock wave decreases. However, when $h \approx h_1^*$, the viscous/inviscid interaction changes to that described in Figure 2 and as illustrated in the sketch of Figure 34(c). Oblique shock waves appear near the periphery of the impinging plume. Since the stagnation pressure drop across an oblique shock wave is less than that

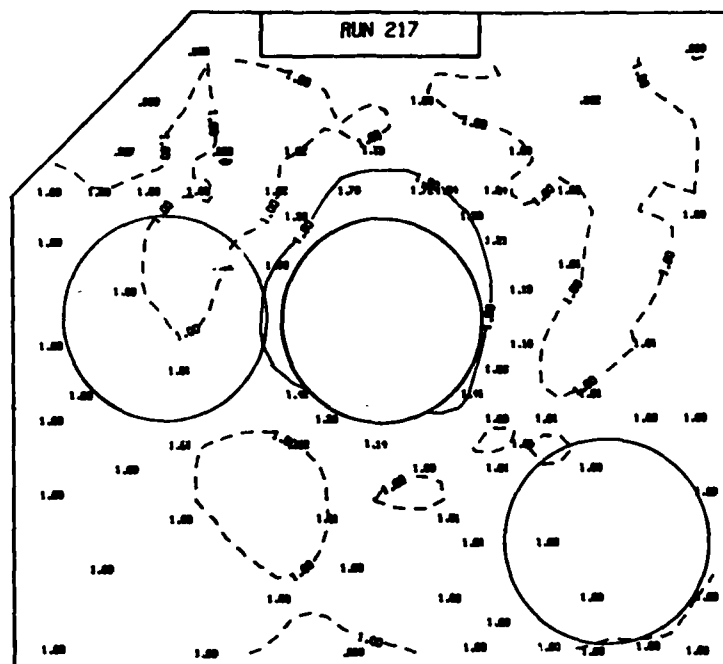


(a) $h = 2.0 r_{ne}$

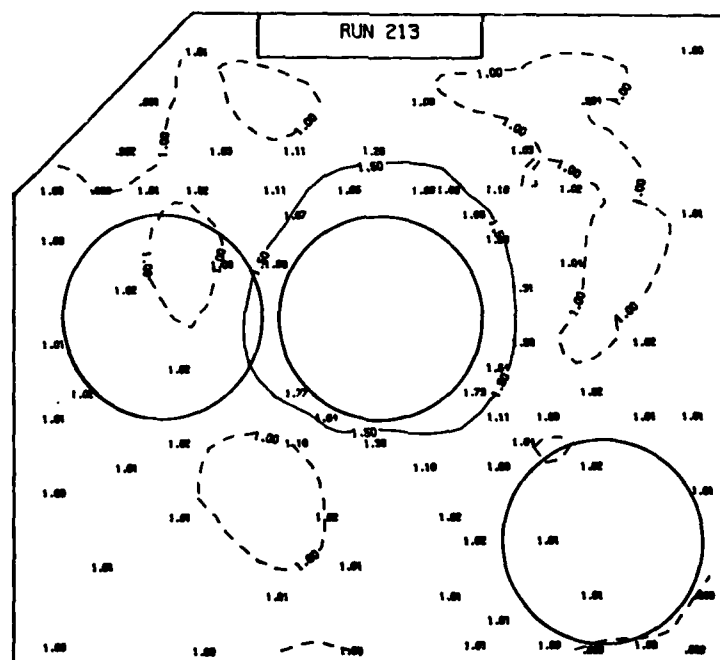


(b) $h = 4.0 r_{ne}$

Figure 32. - Static pressure distributions (tube 2), $p_{t1} \approx 2.76 \times 10^6 \text{ N/m}^2$.

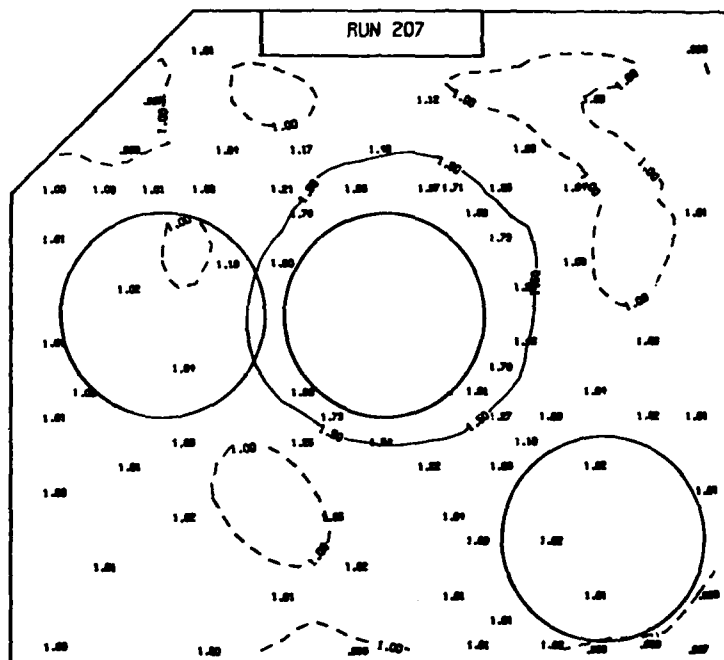


(c) $h = 6.0 r_{ne}$



(d) $h = 10.0 r_{ne}$

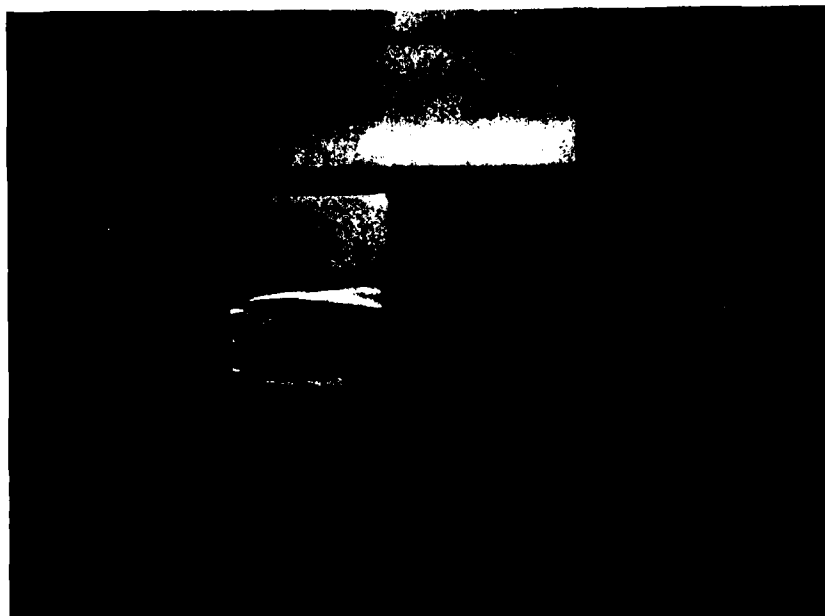
Figure 32. - Continued.



(e) $h = 15.0 r_{ne}$

Figure 32. - Concluded.

DELIBERATELY BLANK



(a) $h = 4.0 r_{ne}$



(b) $h = 6.0 r_{ne}$

Figure 33. - Shadowgraphs of the plume impingement (tube 2) $p_{t1} \approx 2.76 \times 10^6 \text{ N/m}^2$.

DELIBERATELY BLANK



(c) $h = 10.0 r_{ne}$



(d) $h = 15.0 r_{ne}$

Figure 33. - Concluded.

DELIBERATELY BLANK

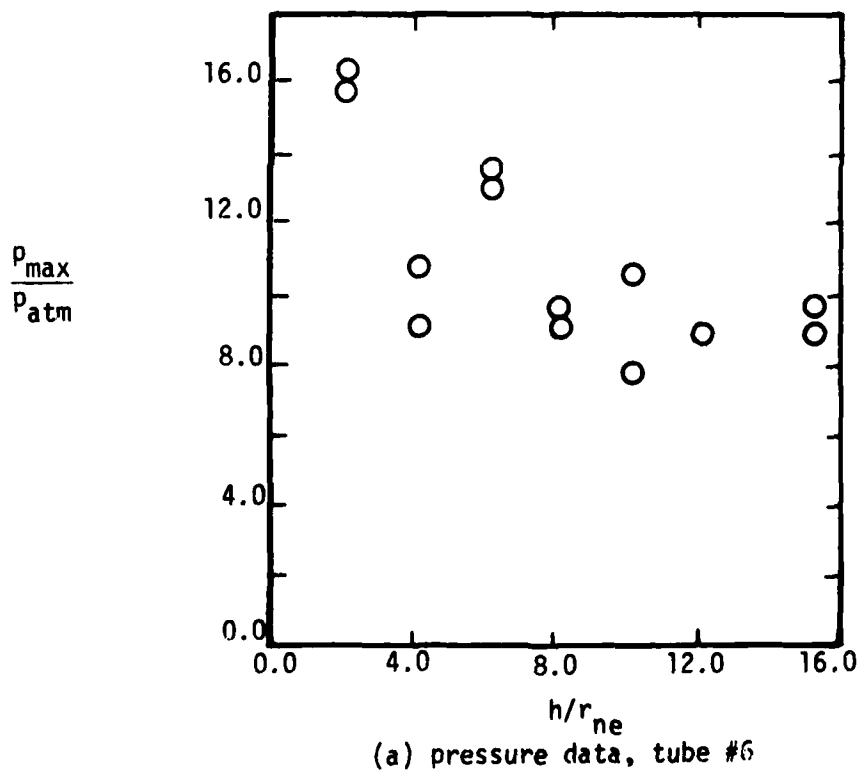
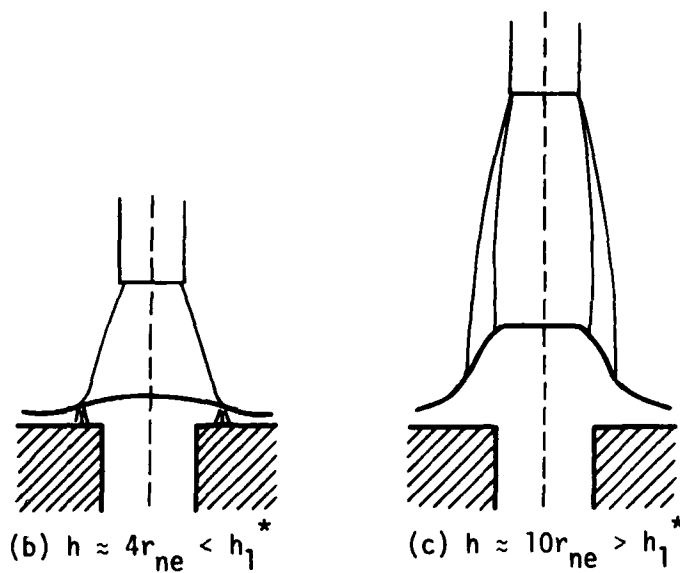


Figure 34. - Characteristics of the flow field defined by maximum static pressures on the launcher face, $p_{t1} = 7.58 \times 10^6 \text{ N/m}^2$.

across a normal shock wave, there is an increase both in the magnitude and in the radial location of the maximum pressure when this change in the shock structure occurs.

The data of Figure 34 are presented again in Figure 35(a), along with similar measurements for $p_{t1} \approx 4.83 \times 10^6 \text{ N/m}^2$ and $2.76 \times 10^6 \text{ N/m}^2$. Maximum pressure measurements are presented in Figure 35(b) for a "launch" from tube 2. When $p_{t1} \approx 4.83 \times 10^6 \text{ N/m}^2$ and h is small, the diameter of the Mach disc is smaller than the diameter of the launch tube. Thus, the pressure peak associated with the stagnation pressure downstream of a normal shock, i.e., the Mach disk, does not appear. However, the pressure peak caused by the appearance of the reflected shock waves that occur when $h > h_1^*$ are evident. Data presented in both Figures 35(a) and (b) illustrate the single peak for $p_{t1} \approx 4.83 \times 10^6 \text{ N/m}^2$. These data also exhibit a significant pressure drop at $h \approx 10.0 r_{ne}$. At a separation distance of $10.0 r_{ne}$ the stagnation pressure required for supercritical flow is approximately $4.83 \times 10^6 \text{ N/m}^2$. Thus, due to viscous dissipation, it is no longer possible to maintain supercritical flow for these conditions. Therefore, the magnitude and radial location of the maximum pressures acting on the launcher face decrease. At $p_{t1} \approx 2.76 \times 10^6 \text{ N/m}^2$ the flow field is subcritical for all nozzle-exit positions. The corresponding maximum pressures are very small.

4.3 Effect of an Open Adjacent Tube

In determining the firing sequence of a multi-tube launcher assembly, it is of interest to investigate the effect that an open tube, adjacent to the launch tube, could have on the impinging flow field. During the present experimental program, static pressures on the face of the launcher were measured for simulated launches from tube 1, from tube 2, or from tube 6 with their respective adjacent tube open. The pressure distributions for a "launch" from tube 1 with tube 2 open and closed are presented and compared in Figures 36 and 37. In general, the opening of the adjacent tube had only a slight effect on the pressure distributions measured on the face of the launcher. The small changes in the isobars may be as much due to the fairing of the measured data as to actual significant changes in the flow field, since the fairing would be affected by slight changes in the individual pressures measured and by the deletion of some pressure orifices. However, in a few cases, i.e. Figures 36(d), 36(f), and 36(h), the high pressure region shifts in the direction of the adjacent tube, where tube 2 is opened with the launch from tube 1. This increase in pressures measured below the crane suggests that the slight asymmetry introduced into the impinging flow field by the open tube is aggravated by the presence of the crane. But this effect was only observed at

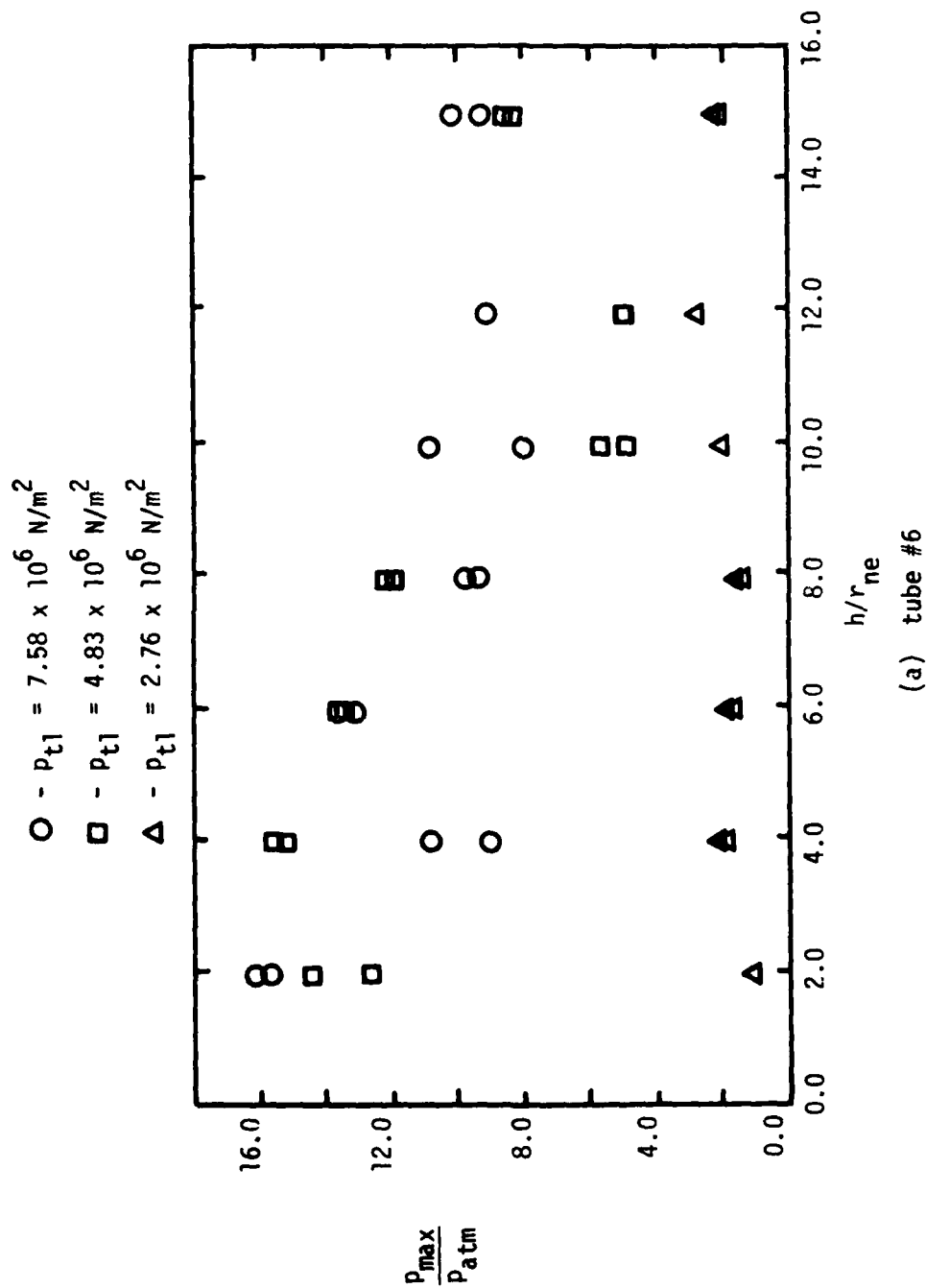


Figure 35. - Maximum static pressures on the face of the launcher assembly.

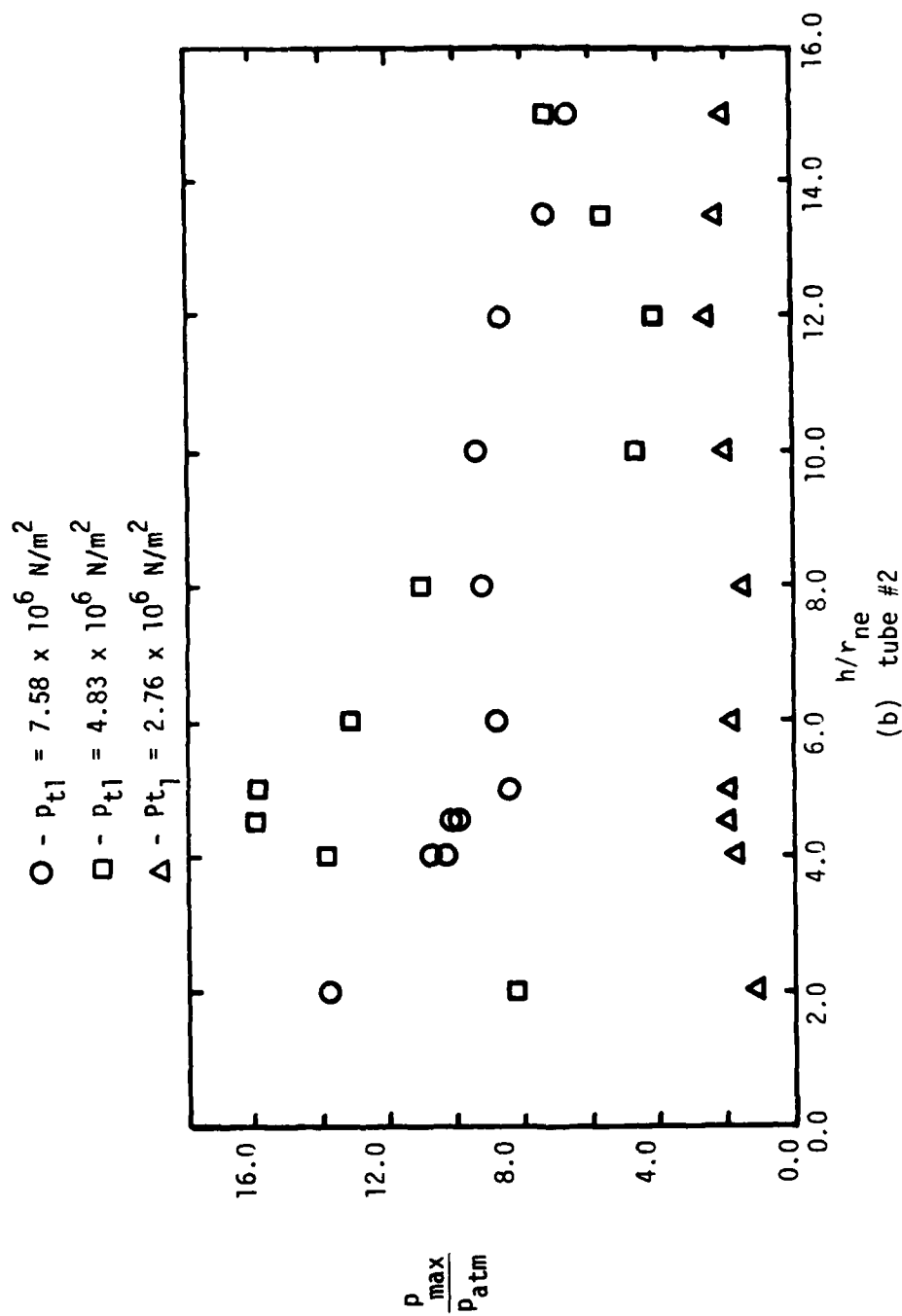
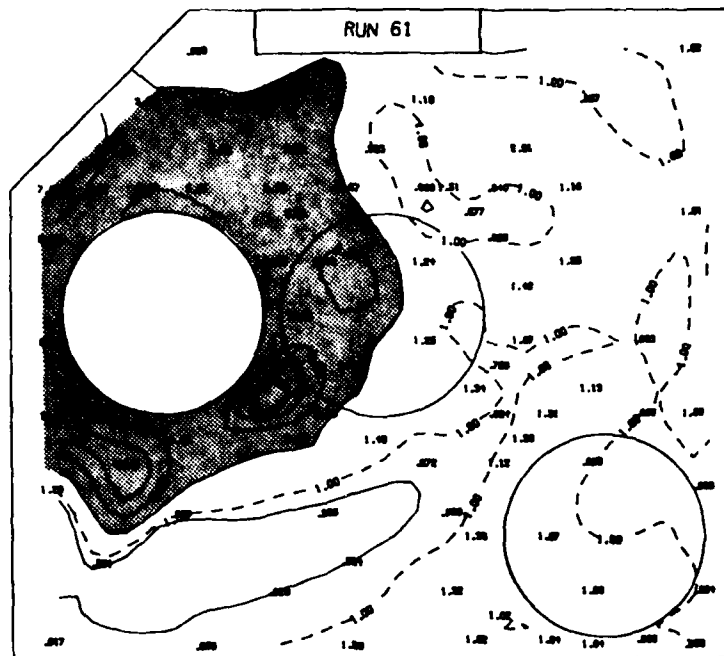
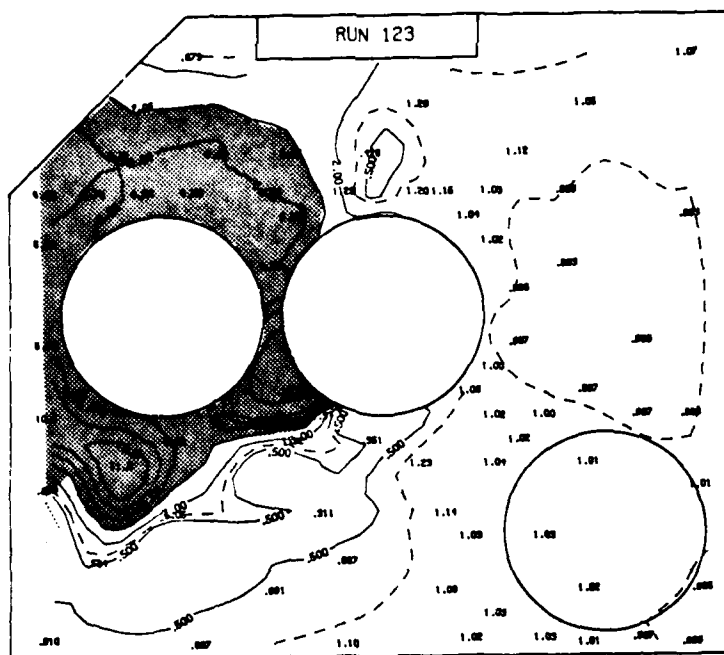


Figure 35. - Concluded.

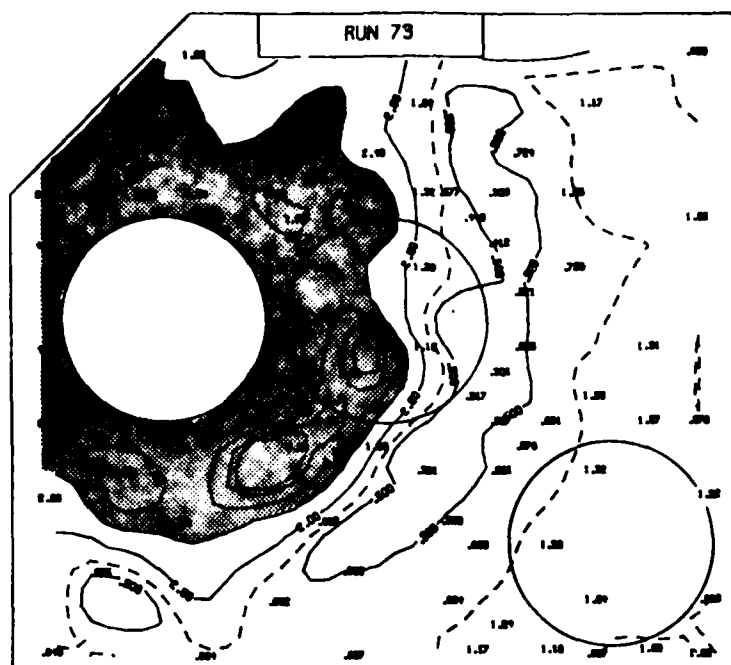


(a) $h = 4.0 r_{ne}$, adjacent tube closed

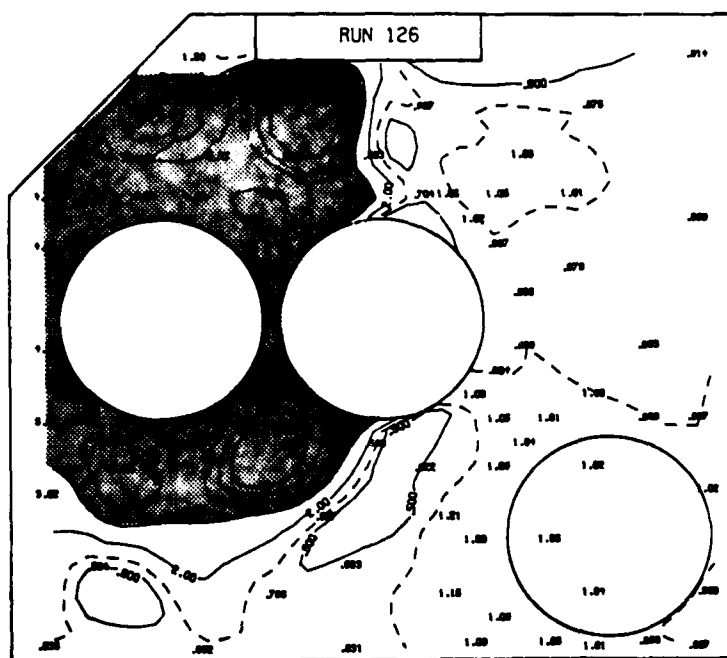


(b) $h = 4.0 r_{ne}$, adjacent tube open

Figure 36. - Static-pressure distributions with adjacent tube closed and open, $p_{t1} \approx 7.58 \times 10^6 \text{ N/m}^2$.

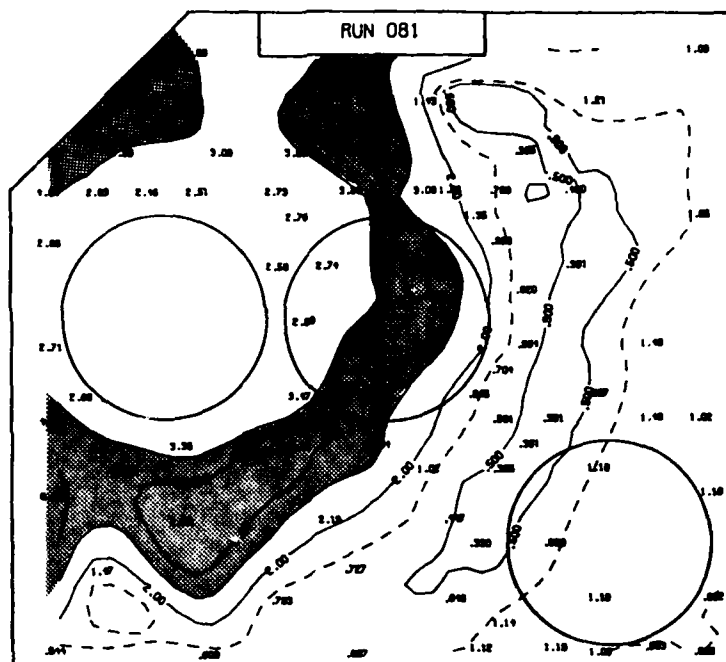


(c) $h = 6.0 r_{ne}$, adjacent tube closed

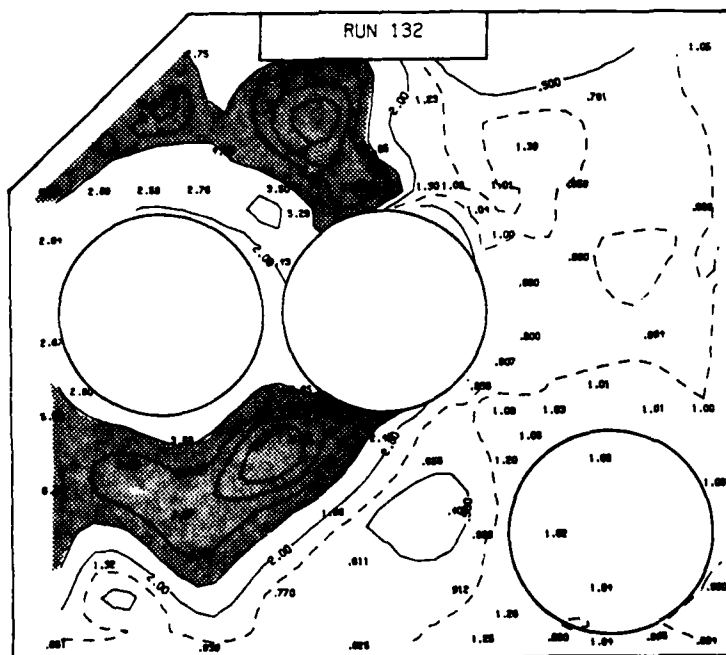


(d) $h = 6.0 r_{ne}$, adjacent tube open

Figures 36. - Continued.

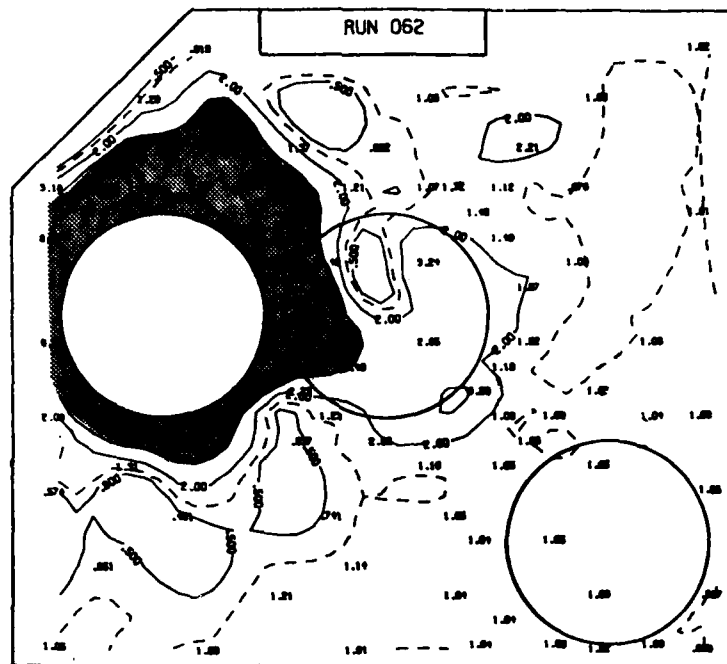


(e) $h = 10.0 r_{ne}$, adjacent tube closed

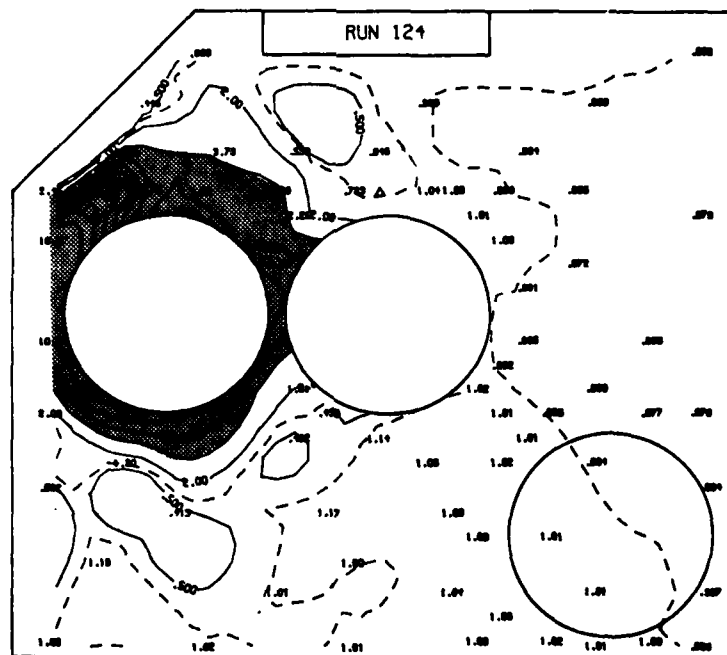


(f) $h = 10.0 \text{ } r_{ne}$, adjacent tube open

Figure 36. Continued.

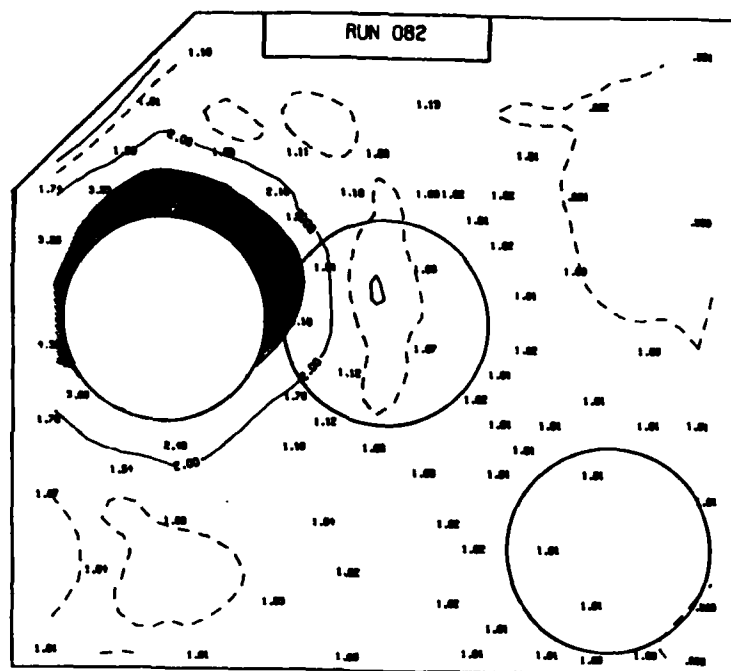


(a) $h = 4.0 r_{ne}$, adjacent tube closed

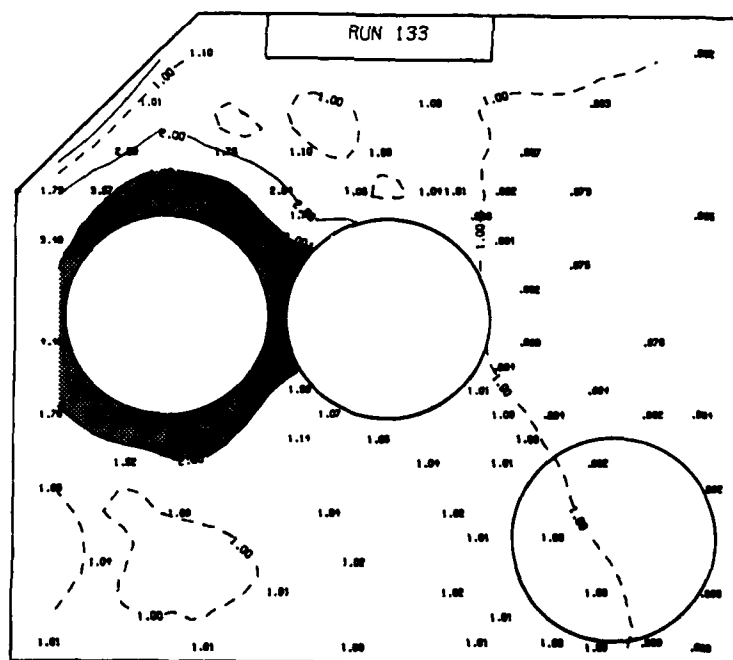


(b) $h = 4.0 r_{ne}$, adjacent tube open

Figure 37. - Static-pressure distributions with adjacent tube open and closed, $p_{t1} \approx 4.83 \times 10^6 \text{ N/m}^2$.



(e) $h = 10.0 r_{ne}$, adjacent tube closed



(f) $h = 10.0 r_{ne}$, adjacent tube open

Figure 37. - Continued.

the maximum stagnation pressure, i.e., when the flow was supercritical. The data obtained from simulated launches from tube 2 and tube 6 exhibited very little change in the isobars when the adjacent tube was opened.

4.4 Pressure Differentials Acting on the Rocket

When the exhaust gases from a rocket that is exiting a given launch tube impinge on the face of the launcher assembly, a complex viscid/inviscid interaction occurs. As a result, a portion of the impinging flow can "splash-back" onto the rocket. The asymmetric character of this "splash-back" flow can cause pressure differentials on the rocket. If large enough, the pressure differentials will affect the free-flight trajectory of the rocket.

As noted earlier, the external surface of the rocket model used in the present experimental program was instrumented with diametrically-opposed orifices, allowing for the direct measurement of static pressures on its external surface. The maximum pressure differentials, i.e., the maximum value of the difference in the pressures measured at diametrically-opposed orifices, are presented in Figure 38 for several launch conditions. Although all of the pressure differentials acting on the rocket were measured with the same precision, the values obtained at those orifices located more than $3.0 r_{ne}$ upstream of the nozzle-exit plane are questionable. When the conditions were such that the exhaust gases entrained air from the "base" region (generating flow toward the nozzle-exit plane), the air flowing over the external surface of the rocket was disturbed by the yoke assembly that was used to restrain the rocket (see Figure 5(a)). The yoke acted as a backward facing step with the entrained air flow reattaching near the pressure orifices located $5.0 r_{ne}$ to $10.0 r_{ne}$ from the nozzle-exit plane. However, the maximum pressure differentials presented in this report always occurred at the pressure orifices that were located within $2.0 r_{ne}$ of the nozzle-exit plane. Thus, these data should represent the effect that the viscid/inviscid interaction has on the maximum pressure differentials acting on the rocket.

Intuitively, one would expect the pressure differentials to be small when most of the exhaust gas is swallowed by the open tube. The effects of "splash-back" would be expected to diminish as the nozzle-exit plane moves further from the face of the launcher. Thus, the maximum pressure differential would be expected to occur when the stagnation pressure is relatively high and when the nozzle-exit plane is near (but not immediately adjacent to) the face of the launcher. The maximum pressure differentials, non-dimensionalized by

the atmospheric pressure, are presented in Figure 38 as a function of separation distance. Data are presented for simulated launches from tubes 1, 2, and 6, both with a single tube open and with two tubes open.

For a stagnation pressure of approximately $7.58 \times 10^6 \text{ N/m}^2$, i.e., Figure 38(a), the peak pressure differentials occur at a separation distance between $4.0 r_{ne}$ and $6.0 r_{ne}$. Since the flow field is supercritical for these conditions and the nozzle-exit plane is relatively close to the launcher, the data support the intuitive reasoning. When $p_{t1} \approx 4.83 \times 10^6 \text{ N/m}^2$, Figure 38(b), the peak pressure differentials occur for separation distances between $4.0 r_{ne}$ and $8.0 r_{ne}$. Again, the flow is supercritical and the nozzle-exit plane is near the launcher. The data for both stagnation pressures also exhibit the effect the launcher geometry has on "splash-back". Launch tube 2 has an overhead crane directly above it. As might be expected, the pressure differentials measured on the rocket are greatest when the rocket has been launched from tube 2. Relatively large pressure differentials were measured for all separation distances less than $8.0 r_{ne}$ for this launch configuration. For some launch conditions from tube 2 the largest static pressures acted on the top ($\phi = 0^\circ$) of the rocket. However, the angular location of the maximum static pressures measured on the rocket was not constant for all separation distances and all chamber pressures. In contrast, the maximum static pressures obtained for simulated launches from tube 1 and tube 6 consistently acted on the outboard side of the rocket, i.e., $\phi = 45^\circ$ to 135° for tube 1 and $\phi = -45^\circ$ to -135° for tube 6. The moment induced by these pressures could cause the rocket to veer away from the axial centerline of the launcher assembly.

As noted earlier, the pressure differentials acting on the rocket were measured both with the adjacent tube being covered and with the adjacent tube being open. The data of Figure 38 indicate that generally the effect of "splash-back" on the rocket is less when the adjacent tube is open.

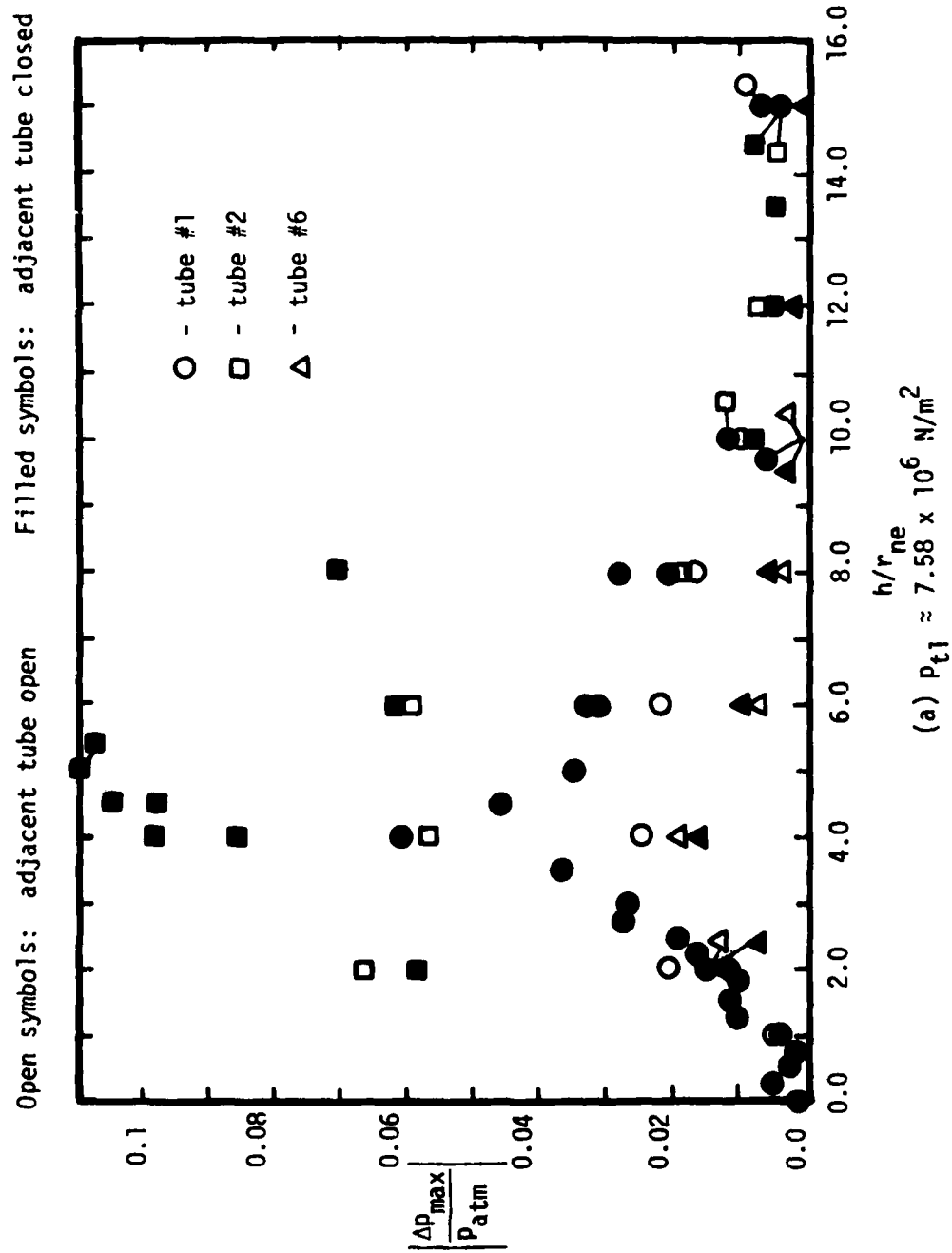


Figure 38. - Maximum pressure differentials acting on the simulated rocket.

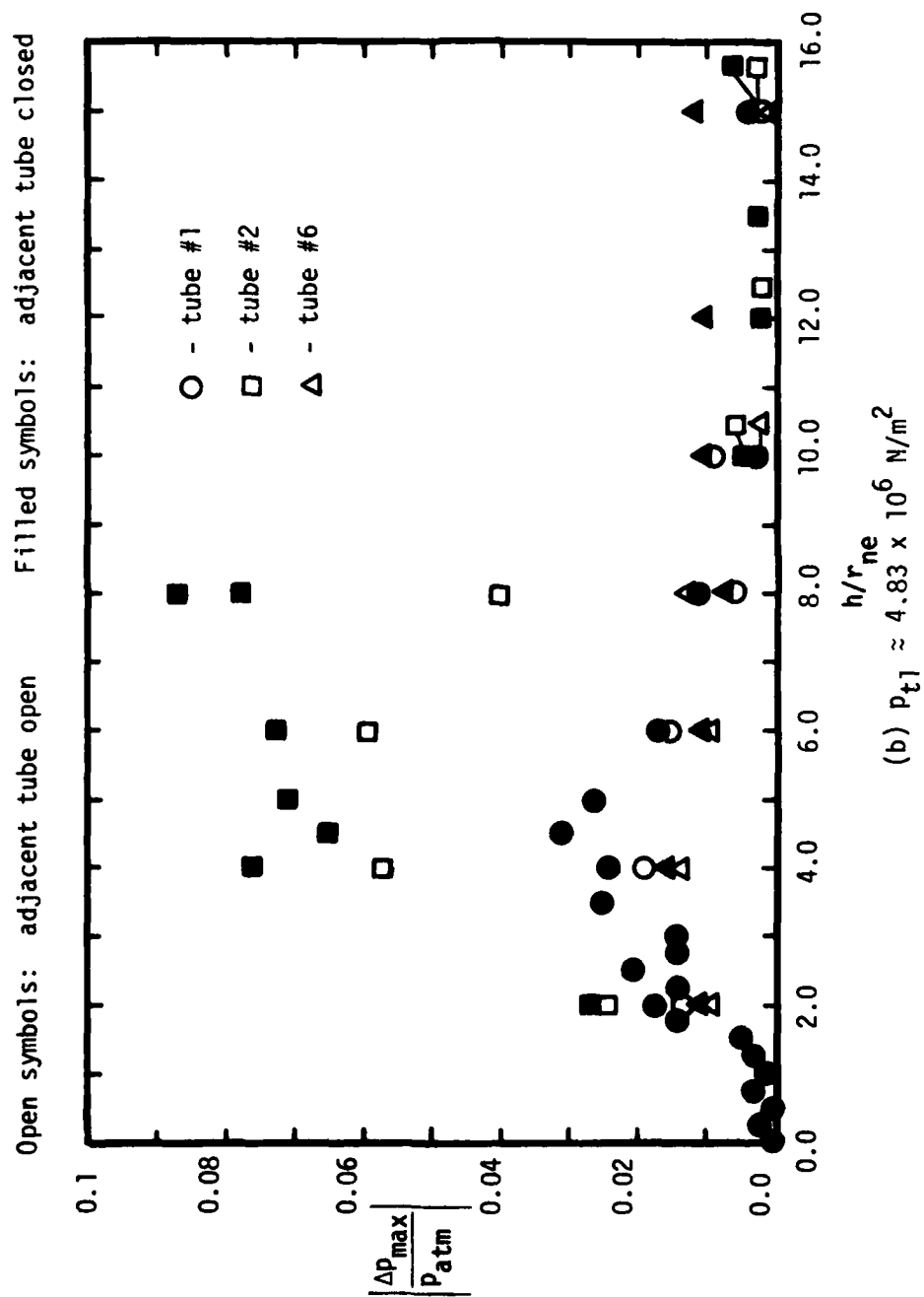


Figure 38. - Concluded.

5. CONCLUDING REMARKS

An experimental program has been conducted in which simulated rocket exhaust plumes impinged on the face of a multi-tube launcher. For the range of variables considered in the present test program, the following conclusions are made.

- 1) The most important characteristic dimension for the impingement flow-field is the ratio of the plume diameter to the diameter of the open tube. For a given nozzle/launcher configuration, this ratio is a function of the stagnation pressure and of the separation distance between the nozzle-exit plane and the launcher.
- 2) When the stagnation pressure is relatively low most of the exhaust gas is swallowed by the open tube. High surface pressures are limited to the region near the rim of the open tube.
- 3) Once a critical value of p_{t1} is exceeded, the central shock wave increases in size and in strength. For these supercritical flows, a large fraction of the exhaust gas flows across the face of the launcher, producing relatively high pressures over large areas of the surface of the launcher. When the flow is supercritical, the primary correlation parameter is the ratio, h/h_1^* .
 - (a) If $h < h_1^*$, the viscid/inviscid shock interaction structure is dominated by the central shock wave. The highest surface pressures occur near the rim of the open tube.
 - (b) When $h > h_1^*$, the central shock wave is bounded by an oblique, reflected shock wave and an annular ring of relatively high pressure occurs near the periphery of the impinging jet. The flow field is similar to that observed when a supersonic jet impinges on a solid plate.
- 4) The opening of one tube adjacent to the launch tube has only a slight effect on the pressure distribution present on the face of the launcher.
- 5) The maximum pressure differentials that act across the missile itself occur when the flow is supercritical and the nozzle-exit plane is near the face of the launcher. The largest pressure differentials were obtained, when the missile was launched from tube no. 2. Although the pressure differentials were not as great in magnitude for launches from tubes no. 1 or 6, the resulting pressure force consistently produced moments that would cause a missile launched from these tubes to veer away from the plane of the launcher.

LITERATURE CITED

1. Vick, A. R., and Andrews, E. H., Jr., "An Experimental Investigation of Highly Underexpanded Free Jets Impinging Upon a Parallel Flat Surface", TND - 2326, June 1964, NASA.
2. Ivanov, M. Y., and Nazarov, V. P., "'Lateral' Interaction of a Supersonic Underexpanded Ideal-Gas Jet With Surfaces of Different Shape", Izvestiya Akademii Nauk SSSR, Mekhanika Zhidkosti i Gaza, No. 6, November - December 1974, pp. 3 - 8.
3. Smith, S. D., Penny, M. M., Greenwood, T. F., and Roberts, B. B., "Exhaust Plume Impingement of Chemically Reacting Gas-Particle Flows", AIAA Paper No. 75-688, AIAA 10th Thermophysics Conference Denver, Colorado, May 1975.
4. Stitt, L. E., "Interaction of Highly Underexpanded Jets With Simulated Lunar Surfaces", TND - 1095, December 1961, NASA.
5. Gummer, J. H., and Hunt, B. L., "The Impingement of a Uniform Axisymmetric, Supersonic Jet on a Perpendicular Flat Plate", The Aeronautical Quarterly, Vol. 22, November 1971, pp. 403 - 420.
6. Henderson, L. F., "Experiments on the Impingement of a Supersonic Jet on a Flat Plate", Journal of Applied Mathematics and Physics, Vol. 17, 1966, pp. 553 - 569.
7. Morch, K. A., "A Theory for the Mode of Operation of the Hartmann Air Jet Generator", Journal of Fluid Mechanics, Vol. 20, 1964, pp. 141 - 159.
8. Semiletchenko, B. G., and Uskov, V. N., "Empirical Formulas for Locating Shock Waves in a Jet Impinging on a Barrier at Right Angles", Inzhenerno - Fizicheskii Zhurnal, Vol. 23, No. 3, September 1972, pp. 453 - 458.
9. Ginzburg, I. P., Semiletchenko, B. G., and Uskov, V. N., "Experimental Study of Underexpanded Jets Impinging Normally on a Plane Baffle" Fluid Mechanics - Soviet Research, Vol. 4, No. 3, May - June 1975, pp. 93 - 105.
10. Golubkov, A. G., Koz'menko, B. K., Ostapenko, V. A., and Solotchin, A. V., "On the Interaction of an Underexpanded Supersonic Jet with a Finite Flat Baffle", Fluid Mechanics - Soviet Research, Vol. 3, No. 1, January - February 1974, pp. 96 - 102.

11. Piesik, E. T., and Roberts, D. J., "A Method to Define Low-Altitude Rocket Exhaust Characteristics and Impingement Effects", Journal of Spacecraft and Rockets, Vol. 7, No. 4, April 1970, pp. 446 - 451.
12. Belov, I. A., Ginzburg, I. P., and Shub, L. I., "Supersonic Under-expanded Jet Impingement upon Flat Plate", International Journal of Heat-Mass Transfer, Vol. 16, 1973, pp. 2067 - 2076.
13. Lawson, C. L., "Software for C1 Surface Interpolation", JPL Publication 77-30, August 15, 1977.
14. Akima, H., "A Method of Bivariate Interpolation and Smooth Surface Fitting for Irregularly Distributed Data Points", ACM Transactions on Mathematical Software, Vol. 4, No. 2, June 1978, pp. 148 - 159.

NOMENCLATURE

A	cross-sectional area
d	diameter
h	distance between nozzle-exit plane and flat plate
h_1^*	distance (h) at which strong instability occurs
h_2^*	distance (h) at which weak instability occurs
M	Mach number
n	jet expansion ratio
p	pressure
r	radius
x, y, z	coordinates of right-handed coordinate system
\tilde{x}	axial coordinate with origin at nozzle-exit plane
γ	specific-heat ratio
ϕ	angular location of pressure orifices on the rocket
θ	nozzle-exit angle

Subscripts

atm	atmospheric conditions
M	relative to Mach disk in free jet
max	maximum
ne	nozzle-exit conditions
s	relative to centered shock in impinging jet
t	tube
t_1	stagnation conditions

Superscript

* sonic conditions

MED
-8